# Numerical Analysis Tools for Modelling Reinforced Concrete Shear Wall Buildings Subjected to Earthquake Loading

a thesis submitted in partial fulfilment of the requirements

for the degree of Doctor of Philosophy

by

Lei Zhang

Department of Civil and Natural Resources Engineering

University of Canterbury

Christchurch, New Zealand

first draft: 22 September, 2019

revised: 22 March, 2020

# Abstract

When it comes to resist lateral loads, shear wall is a preferred structure form. There are two main categories of finite elements to model seismic reposes of reinforced concrete shear walls, namely the microscopic and macroscopic elements. These numerical tools suffer from several vital problems, such as accuracy, efficiency, reliability and applicability, which hinder their engineering applications.

Both experimentally and numerically, it is shown that the in-plane axial-flexural-shear interaction does exist in wall panels. It is not applicable to simply neglect its effect since it could contribute up to 50 % of total deformation for short walls. However, it cannot be well predicted by current macroscopic wall elements yet. By definition, available 1D macro elements, in which heavy use of spring/truss elements is involved, cannot fully reproduce the non-linear shear response/profile along the horizontal direction due to the '*plane sections remain plane*' assumption which is unavoidable during the process of simplifying a 2D planar problem to a 1D one. Another severe issue is the capability of simulating wall-frame interaction. Although some simplification methods have been proposed for hand calculation, it is still complicated to develop finite element models to handle the interactions between wall panels and beams/slabs by using current macro elements, due to the lack of in-plane rotational degrees of freedom.

This project aims to solve above two drawbacks. The main objective is to develop an efficient quadrilateral shear wall element. The new element should be capable of reproducing coupled in-plane **axial-flexural-shear interaction** with reasonable coarse-mesh accuracy subjected to high shear stress and allowing straightforward simulations of the **wall-frame interaction** without any additional configuration.

The proposed (S)GCMQ element is developed based on a modified generalised variational theorem. The Hu-Washizu variational principle is used as a basis, the drilling degrees of free-

dom are introduced into the formulation by a proper decomposition of deformation. The generalised conforming approach is adopted to simplify the formulation. By selecting and optimizing the interpolation functions of stress, strain and displacement fields, GCMQ and SGCMQ elements are formulated. Furthermore, under the proposed variational framework, a series of elements can also be constructed by selecting different shape functions. A five-point integration scheme is also proposed to save computational effort. Since (S)GCMQ a planar element, it can automatically take all three in-plane stress components into consideration as long as the associated material model supports refined material behaviour. By this manner, the interactions among different stress components can be represented.

The validations of (S)GCMQ are performed via some selected elastic/plastic problems. Simulations of available shear wall specimens/structures are conducted with proper material models in the calibration section. (S)GCMQ is free from shear and volumetric locking and shows good bending performance. (S)GCMQ also improves the tolerance to mesh distortion. (S)GCMQ exhibits good coarse mesh accuracy so that it can be used in practical applications with a relatively low computational cost. Without loss of generality, (S)GCMQ provides an efficient alternative to numerical simulations of reinforced concrete shear walls.

# Acknowledgement

The supervisions of Dr. Chin-Long Lee, Prof. Athol J. Carr and Prof. Rajesh P. Dhakal are gratefully acknowledged.

The financial support offered by the Earthquake Commission is appreciated.

Deputy Vice-Chancellor's Office

Postgraduate Research Office

UNIVERSITY OF CANTERBURY
*Te Whare Wānanga o Waitaha*
CHRISTCHURCH NEW ZEALAND

## Co-Authorship Form

This form is to accompany the submission of any thesis that contains research reported in co-authored work that has been published, accepted for publication, or submitted for publication. A copy of this form should be included for each co-authored work that is included in the thesis. Completed forms should be included at the front (after the thesis abstract) of each copy of the thesis submitted for examination and library deposit.

Please indicate the chapter/section/pages of this thesis that are extracted from co-authored work and provide details of the publication or submission from the extract comes:
Sections 3.1, 3.2, 3.3, 3.4, 3.5, 3.6, 4.2, 4.3, 4.4, 4.5, 4.6 and 4.7 are published in the journal paper *A new drilling quadrilateral membrane element with high coarse-mesh accuracy using a modified Hu-Washizu principle* with **International Journal for Numerical Methods in Engineering** (doi: 10.1002/nme.6066).

Please detail the nature and extent (%) of contribution by the candidate:
100 %

Certification by Co-authors:
If there is more than one co-author then a single co-author can sign on behalf of all.
The undersigned certifies that:

- The above statement correctly reflects the nature and extent of the Doctoral candidate's contribution to this co-authored work.
- In cases where the candidate was the lead author of the co-authored work he or she wrote the text.

Name: Chin-Long Lee Signature: (Chin-Long Lee) Date: October 1, 2019

Deputy Vice-Chancellor's Office

Postgraduate Research Office

UNIVERSITY OF CANTERBURY
*Te Whare Wānanga o Waitaha*
CHRISTCHURCH NEW ZEALAND

## Co-Authorship Form

This form is to accompany the submission of any thesis that contains research reported in co-authored work that has been published, accepted for publication, or submitted for publication. A copy of this form should be included for each co-authored work that is included in the thesis. Completed forms should be included at the front (after the thesis abstract) of each copy of the thesis submitted for examination and library deposit.

Please indicate the chapter/section/pages of this thesis that are extracted from co-authored work and provide details of the publication or submission from the extract comes:
Sections 3.9, 5.2, 5.3, 5.4, 5.5, 6.4 and 6.5 are published in the journal paper *Numerical evaluations of a novel membrane element in simulations of reinforced concrete shear walls* with **Engineering Structures** (doi: 10.1016/j.engstruct.2019.109592).

Please detail the nature and extent (%) of contribution by the candidate:
100 %

Certification by Co-authors:
If there is more than one co-author then a single co-author can sign on behalf of all.
The undersigned certifies that:

- The above statement correctly reflects the nature and extent of the Doctoral candidate's contribution to this co-authored work.
- In cases where the candidate was the lead author of the co-authored work he or she wrote the text.

Name: Chin-Long Lee Signature: (Chin-Long Lee) Date: October 1, 2019

*To all my friends.*

*May we live in freedom.*

# Contents

# List of Figures

# List of Tables

# 1

# Introduction

## 1.1 Background

The circum-Pacific belt (**Ring of Fire**) is an active seismic zone. Many earthquakes occur in this region. Of the earthquakes, 6 out of 17 largest earthquakes since 1900* occurred during this century. New Zealand is located at one end of the circum-Pacific belt, two faults (the Alpine fault and the Wellington fault) run the length of the country, which makes it to be frequently struck by earthquakes.

The most recent hazardous earthquake in New Zealand is the Christchurch earthquake occurred at 12:51 p.m., on 22nd February, 2011. The event caused collapse of two multi-storey buildings and killed 185 people in total. Detailed investigations of failure mechanisms of collapsed buildings can be found in the reports by Royal Commission (2011b,a), Jury (2011) and Kam and Pampanin (2011). During this earthquake, a shear wall, located on the ground floor of Hotel Grand Chancellor (HGC) building, experienced high torsional actions and finally failed due to out-of-plane buckling. The failure *came close to causing a catastrophic collapse of the building* (Royal Commission, 2011b). Wall failures due to all kinds of mechanisms, such as shear failure and concrete crushing, were also observed in recent earthquakes in Chile. Specific analyses and discussions could be seen elsewhere (Carpenter et al., 2010; Wallace, 2012).

It could be noted that the tensile flexure failures are rarely observed in these earthquakes.

*Please check USGS database. https://earthquake.usgs.gov/

This is possibly due to the fact that, after extensive research, structural engineers have gained comprehensive understanding of flexural behaviour of shear walls. Consequently, the flexure capacity is well designed and the corresponding failure patterns can be successfully suppressed. In contrast, engineers have limited knowledge about the shear behaviour of wall panels due to its inherent intricacy. In practice, the shear response is assumed to be elastic and its effect is thus often neglected, particularly for slender walls. However, under some particular circumstances, such as high shear stresses and/or low aspect ratios, shear deformation may contribute a considerably significant amount (up to 50 %) to the total deformation, particularly after shear yielding. Such phenomena were observed in a number of experiments (see, e.g., Oesterle et al., 1980; Thomsen and Wallace, 2004; Tran and Wallace, 2015).

For numerical analyses, it is, in general, a difficult task to model shear walls due to the intricacies of both the corresponding geometries and material properties. Although both global and local responses could be generated by using general purpose microscopic[†] finite elements in commercial finite element analysis (FEA) packages (see, e.g., Kazaz et al., 2006; Palermo and Vecchio, 2002, 2004, 2007), it is impractical to use these elements to conduct simulations of large scale structures due to efficiency problems (Orakcal et al., 2004). To date, engineers still prefer to use macroscopic elements for shorter analysis times.

Unfortunately, most of current macroscopic shear wall elements can only be used at the global level. By definition, macroscopic elements are incapable of predicting refined in-plane coupled response. This is also pointed out by Fischinger et al. (2004). Essentially, they are 1D elements that take displacements along element axes/chords as inputs and use 1D material models to compute response. The transverse response cannot be taken into account by the material models used. Although some macroscopic elements that incorporate 2D plane stress material models have been proposed recently, they cannot be used in practical simulations due to other numerical deficiencies. For example, to produce transverse shear response, some elements attempt to construct **biaxial** strain based on **uniaxial** displacement inputs. Since the biaxial strain formulated in this way lacks a mechanics basis and may not be able to describe the true strain field, such an approach is nothing but GIGO (garbage in garbage out, computer science terminology) no matter how good the adopted material model is. Discussions regard-

[†]There are no consensual definitions of macroscopic and microscopic elements. In the following context, all 1D elements, including any spring and beam based elements, are categorized as macroscopic elements. 2D elements that are formulated according to continuum mechanics and converge to analytical solutions with mesh refinements are referred to as microscopic elements.

ing recently proposed wall elements can be seen in Chapter 2. Thus, almost all numerical simulations of low-rise walls were carried out by using microscopic elements (see, e.g., Gulec and Whittaker, 2009).

As pointed out recently by Wallace (2012), additional numerical investigations, particularly at the macroscopic level, are still needed for shear walls with low aspect ratios subjected to significant shear stresses. As can be seen later, the current macroscopic elements also suffer from several vital problems, such as incomplete coverage of failure mechanisms due to the 'plane sections remain plane' assumption, lack of capability to account for wall-frame interactions and out-of-plane response. Thus, an efficient element that can ease those problems is still in demand.

## 1.2 OBJECTIVES

The main objective of this work is to develop a new finite element that exhibits high performance for modelling tasks of panel like 2D structure members, such as shear walls. According to Wriggers (2008), to develop a new continuum element with good performance, the following objectives shall be met.

1. locking free behaviour for incompressible materials,
2. good bending performance,
3. no locking in thin elements,
4. no sensitivity against mesh distortions,
5. good coarse mesh accuracy,
6. simple implementation of nonlinear constitutive equations and,
7. efficiency (e.g., fewer integration points).

Apart from the above objectives, it is preferable for the new element to have only corner nodes to simplify the meshing process and minimise the sizes of global matrices. It is also preferable to include in-plane, drilling, rotational degrees of freedom (DoFs) into the new element. The presence of drilling DoFs can be utilised to address the compatibility issue existing in modelling wall-frame interactions. Elements with midside nodes are not suited to dynamics or large deformation problems (Belytschko et al., 2014). Furthermore, analysts are interested in not only displacement but also strain and stress results. The capability of simplifying the

recovery of better strain and stress distributions is also desirable.

## 1.3 ORGANISATION

This dissertation is organised in the following way.

Chapter 2 presents a brief review of existing wall elements. Their drawbacks are discussed, which serve as the motivations of this work.

Chapter 3 introduces the formulation of the proposed GCMQ element and its simplified version SGCMQ. Other implementation related aspects, such as integration schemes and state determination algorithm, are also introduced.

Chapter 4 reports the elastic validations of the proposed GCMQ element with some widely adopted numerical examples. Most of those examples have analytical solutions.

Chapter 5 summarises the material models used in this work.

Chapter 6 presents a series of applications, including both static and dynamic loading cases with simple and complex material models.

Chapter 7 concludes this work and discusses some common questions regarding numerical modelling of panel/wall like structures.

## 1.4 IMPLEMENTATION

The digital copy of this dissertation is available in this repository tlcfem/phd.thesis[‡].

All numerical examples, unless otherwise stated, are carried out by using suanPan[§], an open source finite element analysis framework. Model scripts of all examples can be found in the same repository tlcfem/phd.thesis[¶].

The proposed element has been implemented in RUAUMOKO (Carr, 1998). It is also available as an external dynamic library that works with OpenSees, which can be obtained from this repository gcmq-opensees-implementation.

Other files are available upon request via tlcfem@gmail.com.

[‡] https://gitlab.com/tlcfem/phd.thesis
[§] https://github.com/TLCFEM/suanPan
[¶] https://gitlab.com/tlcfem/phd.thesis

## 1.5 TOOLS USED

This dissertation is prepared with LaTeX in TeXstudio. Figures are mainly generated by using TikZ and gnuplot. Some post-processing results of numerical models are produced by ParaView. Numerical examples shown in § 2.2.2 are carried out in OpenSees. Data processing is mainly performed in MATLAB®. The author would like to thank all developers of those tools.

Although the colours, line styles, etc. of data virtualisations are carefully selected in order to avoid ambiguities that readers would encounter with monotone printing, some figures may still be difficult to read. It is thus recommended to read the digital version of this dissertation.

# 2

# Literature Review

An overall literature review of existing wall elements is introduced first. Recent state-of-the-art review can also be seen elsewhere (see, e.g., Wu et al., 2016). In what follows, discussions of the main drawbacks of those elements are presented.

## 2.1 Current Wall Elements

### 2.1.1 Beam/Truss Analogy

As a natural simplification employed by civil engineers in the computation of 2D panel-like structures, the simple and straightforward equivalent beam/truss analogy was introduced long ago, even earlier than the introduction of finite element methods (FEM). Before the invention of high performance computation tools, such a method has once been quite popular and efficient as it can significantly reduce the complexity of target problems and make them easier to solve by pure hand calculation.

In the modern era, basic components of a typical beam element with lumped plasticity are depicted in Fig. 2.1. Shear response can be recovered to a certain degree in accordance with the Timoshenko beam theory. However, due to a lack of proper shear stiffness degradation theories, it is in general difficult to produce a non-linear shear response. Analogically, such a beam element can be used for structural components dominated by flexural response such as slender

walls (walls with high aspect ratios). Thomson et al. (2009); Martinelli and Filippou (2009) and Rejec et al. (2011) adopted similar concepts in their FE analyses of cantilever walls and obtained satisfactory global responses. However, details of wall cross section, as well as other local damage, cannot be produced by those elements. Similar variants were also proposed over the years (e.g., Taylor, 1977).

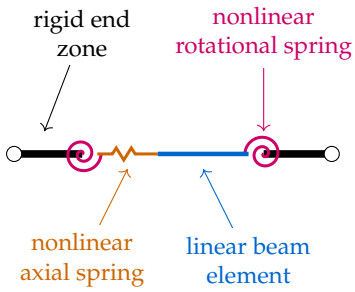


**FIGURE 2.1.** equivalent beam element

For short and squat walls, as shear response often plays a non-negligible role and may even govern the failure mode, numerical simulations should be able to produce the shear behaviour to a certain degree. Based on this fact, the equivalent truss (lattice) model (Hrennikoff, 1941) is often employed as an alternative to the beam analogy.

The model is illustrated in Fig. 2.2. Both vertical and horizontal trusses (or beams in some models) are used to simulate flexural response while shear behaviour is described by two diagonal bracing bars. The equivalent truss model is capable of producing the stress redistribution caused by diagonal shear failure. Such a truss model was adopted by Williams (2014) and Lu and Panagiotou (2014) in modelling shear walls.

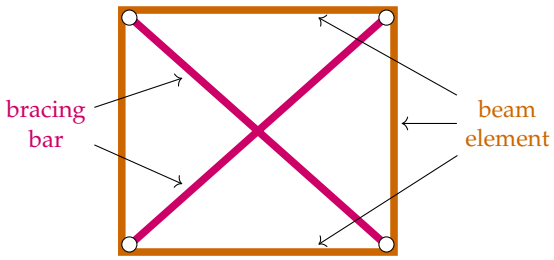


**FIGURE 2.2.** equivalent truss model (Hrennikoff, 1941)

However, when it comes to an inelastic stage, due to the lack of an explicit relationship between axial behaviour of the bracing bars and the shear response of the wall panels, it becomes difficult to determine the stiffness of the diagonal bars, as well as the corresponding hysteresis model. This is also pointed out by others (Vulcano, 1992; Jiang et al., 2005). Meanwhile, only

diagonal shear failure pattern can be described by such a model. Hence, the truss analogy has limited applications. More elegant elements should be developed.

### 2.1.2 Fibre-Based Elements

#### Three-Vertical-Line-Element Model

To reduce the complexity of numerical models, it is common to decouple flexural and shear response and simulate them independently. Based on the discoveries in a three-storey shear wall structure test carried out in 1981, Kabeyasawa et al. (1983) proposed a macro model named three-vertical-line-element model (TVLEM) to model a full-scale seven-story reinforced concrete wall structure.

The model is depicted in Fig. 2.3a. According to the 'plane sections remain plane' assumption, boundary beams are simplified to rigid ones while two non-linear axial springs are employed to simulate the tension/compression response of boundary columns, In the middle of the model, a shear spring and an axial spring, along with a rotational spring, are adopted to model the in-plane response. Alternatively, for the purpose of developing a more universal model, the response of concrete and steel can be defined individually by replacing every single spring component with a spring set consisting two springs in parallel: one for concrete and the other for steel.

Proper hysteresis models, such as the well known Takeda model* (Takeda et al., 1970), should be defined *a priori* for every spring component according to experimental data. Generally, the hysteresis model is defined based on the response of corresponding structure component. The accuracy of this TVLEM fully depends on the refinement level of the hysteresis model adopted. It is worth noting that no conventional constitutive model (material level stress-strain relationship) is defined in this model. For different reinforcement configurations, calibrations are always necessary for the hysteresis models adopted.

The major drawback of TVLEM stems from the **incompatibility** between the deformation of boundary axial springs and the one of the rotational spring. Linde and Bachmann (1994) tried to address this problem by omitting the rotational spring and further calibrating the remaining springs. Apart from this, the flexural and shear response are uncoupled, which apparently

*Detailed description of the original model and modified versions can be found in reports by Otani and Sozen (1972) and Chang and Mander (1994).

does not meet the real situation. Hence, further studies were carried out not long after the proposition of TVLEM.

### Multi-Vertical-Line-Element Model

To reduce as many empirical assumptions as possible (Azzato and Vulcano, 1996), as well as to eliminate inherent deficiencies of the aforementioned TVLEM, a modification, which was called multi-component-in-parallel model initially and then renamed to multi-vertical-line-element model (MVLEM), was proposed by Vulcano et al. (1988) and later modified by Fischinger et al. (1992).

The shear spring at height $ch$ remains unchanged while the rotational one is cancelled, as shown in Fig. 2.3b. Theoretically, the value of parameter $c$ should be determined according to curvature distribution along wall height. Several methods have been proposed to determine $c$ and suggested values are commonly between 0.33 and 0.50 (Jiang et al., 2005). A value of $c = 0.4$ was recommended and widely adopted in MVLEM by other researchers. Meanwhile, the middle axial spring is split into several axial springs which are laterally distributed. Both the number and location of non-linear axial springs can be customized to obtain a desired prediction.

Due to its simple formation and explicit physical meaning, MVLEM quickly gained popularity in the civil engineering community during the last two decades. A number of research have been carried out with regard to the performance of MVLEM subjected to various conditions, such as progressive collapse (Bao and Kunnath, 2010), slender walls under both cyclic and monotonic loading (Han et al., 2008; Chen et al., 2011; Yang et al., 2013), parametric investigation and/or calibration (Fischinger and Isaković, 2000; Orakcal and Wallace, 2006; Dashti et al., 2011).

Azzato and Vulcano (1996) conducted numerical simulations of a scaled RC shear wall structure by using three aforementioned macroscopic elements: beam element, TVLEM and MVLEM. A detailed comparison was carried out with regard to the effectiveness and reliability of the adopted elements. The result revealed that the shear response at the base of the wall was underestimated, particularly when subjected to strong ground motions. Lu and Chen (2005) employed MVLEM, along with the fibre beam element, to simulate the static response of a coupled shear wall structure. The ascending part of the obtained force-displacement curve

was quite reasonable but the model was unable to simulate the descending branch at both failure and collapse stages. Wang and Shen (2005) expanded the original MVLEM for tube structures while Kante (2005) developed a 3D version by combing two MVLEM elements along two orthogonal directions together.

It has been shown that MVLEM can produce a reasonable flexural response as long as refined hysteresis models (for both vertical and lateral springs) are applied (Fischinger et al., 2004). However, it is observed that shear response is often **underestimated**, particularly under high shear loads (Colotti, 1993). Furthermore, since shear and flexural deformations are still uncoupled, the prediction of shear-flexure interaction is **limited**, especially for walls with moderate to low aspect ratios. Another major drawback is that the fixed-end rotation, which is caused by the lumped plastic deformation, can be simulated by neither TVLEM nor MVLEM (Azzato and Vulcano, 1996), this problem is studied by Ghobarah and Youssef (1999), special springs are added to account for additional rotations.

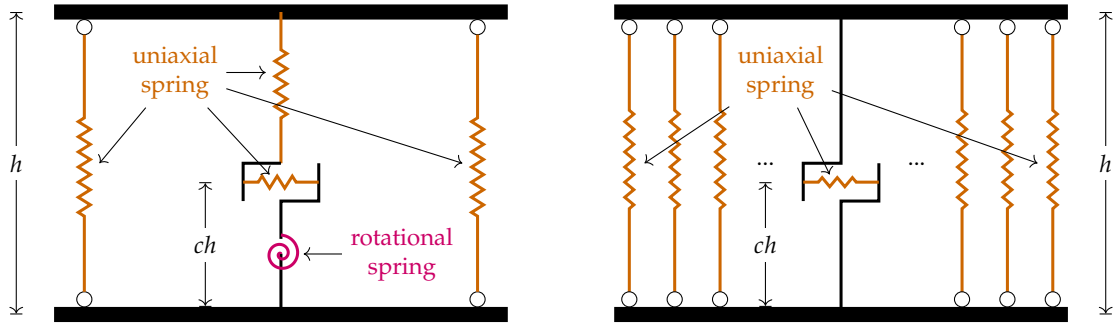


(A) TVLEM (Kabeyasawa et al., 1983) (B) MVLEM (Vulcano et al., 1988)

FIGURE 2.3. illustrations of fibre-based elements

### 2.1.3 Shear-Flexure Interaction Elements

Based on the original TVLEM, Milev (1996) employed 2D quadrilateral elements to simulate wall panels rather than three non-linear springs. Fig. 2.4 illustrates the modified model. Similar elements can also be found elsewhere (see, e.g., Chen and Kabeyasawa, 2000). In fact, such a modification can be deemed as a correction of traditional membrane elements after accounting for the stiffness difference between wall panel and boundary members.

In this sense, the shear wall element adopted by Mo et al. (2008), which is shown in Fig. 2.5, can be regarded as a further refinement. Both the boundary beams and columns are represented by non-linear beam-column elements while the wall panel is still simulated with quadrilateral

membranes. Such an element is more like a microscopic model rather than a macroscopic one.

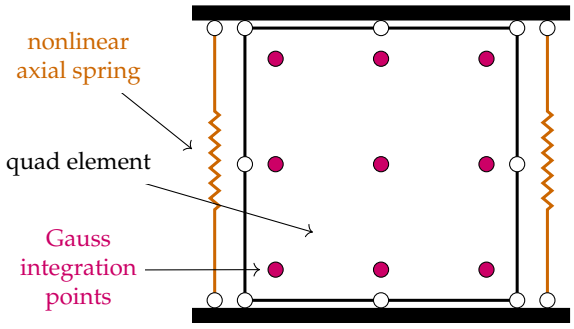


**FIGURE 2.4.** hybrid shear wall element (Milev, 1996)

To produce shear response with a better accuracy, Colotti (1993) modified MVLEM by substituting the non-linear shear spring with 2D membrane elements. By incorporating a 2D constitutive model called modified compression field theory (MCFT) (Vecchio and Collins, 1986), a reasonable prediction of shear response under monotonic loads was achieved. A similar approach was also adopted by Jiang and Lu (2002).

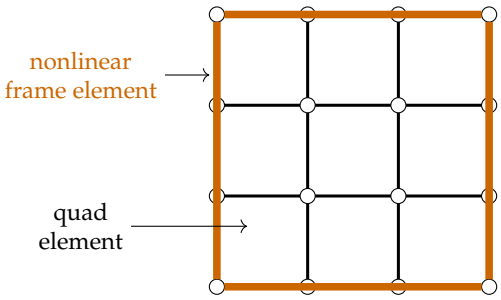


**FIGURE 2.5.** hybrid shear wall element (Mo et al., 2008)

Li and Li (2004), Orakcal and Wallace (2006) and Massone (2006) modified the original MVLEM by assigning one shear spring to each axial spring. The response of every spring set was calibrated using a 2D membrane element. The corresponding sensitivity studies were also carried out. Those models appeared to be capable of predicting the shear-flexural interaction reasonably for concrete shear walls with low aspect ratios under monotonic loads.

Recently, Kolozvari, Orakcal and Wallace (2015) abandoned the spring system concept by substituting non-linear axial springs with panel elements and proposed a new element called SFI-MVLEM, the modelling philosophy of which resembles the one of the aforementioned models proposed by Li and Li (2004) and Massone (2010). It is claimed that SFI-MVLEM exhibits a decent ability to predict load-displacement response under cyclic loads. Details can be found elsewhere (Kolozvari, 2013; Kolozvari, Tran, Orakcal and Wallace, 2015).

Apparently, the essential concept of all MVLEM modifications mentioned above can be traced back to the work by Colotti (1993), that is, replacing spring components by more refined finite elements (e.g., 2D membranes). Since microscopic elements are strictly developed with accordance to solid mechanics, convergence is often guaranteed. However, it should be noticed that in general more computation effort is required. Meanwhile, some numerical deficiencies exist in those modifications. The performance of which is unreliable. Relevant discussions would be presented later in this chapter.

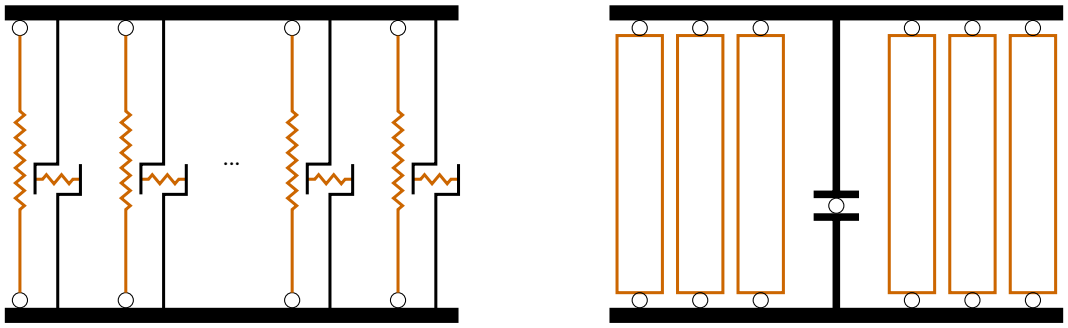

(A) modified MVLEM (Massone, 2010) (B) SFI-MVLEM (Kolozvari, 2013)

FIGURE 2.6. illustrations of modifications of MVLEM

### 2.1.4 Microscopic Elements

Numerical analyses of RC shear walls purely based on microscopic 2D or 3D finite elements were also carried out in recent years (see, e.g., Vecchio and Chan, 1990; Colotti, 1993; Ayoub and Filippou, 1998; Kazaz et al., 2006; Palermo and Vecchio, 2007; Gulec and Whittaker, 2009; Parulekar et al., 2014; Kolozvari et al., 2019). Most of these works focused on verification of the newly proposed concrete constitutive models, rather than the elements themselves. Since convergence (to analytical solution) can be guaranteed by using such a microscopic approach, the error caused by the elements could be significantly reduced, hence it is easier to isolate and evaluate the performance of different constitutive models. Among the new approaches, Barrales (2012) and Kagermanov and Ceresa (2016) adopted membrane elements with drilling DoFs in analyses of wall members. The presence of rotational degree of freedom allows interaction between the membrane and beam elements and thus provides a very promising approach to model wall-frame interactions.

Another compromise is the laminated element (Hinton and Owen, 1984), which is based on composite material mechanics theories. Reinforced concrete can be regarded as a two phase

material. As long as the reinforcement is (close to) uniformly distributed, it is easy to adopt a series of thin steel layers (plies) to represent reinforcement in an averaged sense. Furthermore, since under most circumstances reinforcement is orthogonally arranged, it can be decomposed into two independent layers (each for one direction) and then uniaxial material models can be applied. The concept behind such a method is 'divide and conquer', which is similar to the one of popular fibre frame elements. Fig. 2.7b illustrates a typical multi-layer shell element.

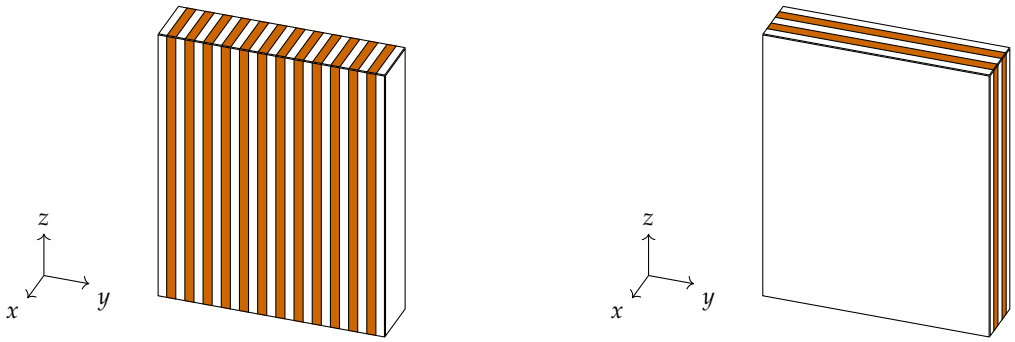


(A) laminated beam element (B) laminated shell element

**FIGURE 2.7.** illustrations of laminated elements

Polak and Vecchio (1993) employed the laminated shell element (Hinton and Owen, 1984) and MCFT for analyses of RC shell structures. Simple verifications were then carried out under different loading conditions, including membrane loads, flexure and out-of-plane shear. The results revealed that the model proposed could generate both in-plane and out-of-plane behaviour with a satisfactory level of accuracy. Similar work can be seen in the work by Miao et al. (2006); Nakamura et al. (2009); Lu et al. (2015).

In the work by Belmouden and Lestuzzi (2007), the shear wall model was discretised into several layers along wall width. Similar to fibre elements, each layer was simplified to beam element with different material models according to various configurations (reinforcement, confinement, etc.) as shown in Fig. 2.7a. The interface bond-slip sub-element was also attached to the model to account for the bond-slip effect. It is shown that the multi-layer beam element was able to reproduce the load-displacement curve with reasonable accuracy.

Valoroso et al. (2014) compared the performance of both beam and shell elements with regard to non-linear analysis of reinforced concrete shear walls. Since the classical beam kinematics assumes that 'plane sections remain plane', the wall-frame interaction, which can be well predicted by shell elements, however, cannot be represented by frame elements. Correspondingly, the curvature distributions of beams were underestimated in the beam model.

Such laminated elements are more often studied and extended when it comes to coupled-field problems. A number of different formulations were developed recently (see, e.g., Bailey, 1995; Huang et al., 1999; Sze et al., 2002; Zhang and Bradford, 2007).

### 2.1.5 Summaries of Current Elements

A summary matrix of current shear wall elements and the associated concrete material models is presented in Fig. 2.8.

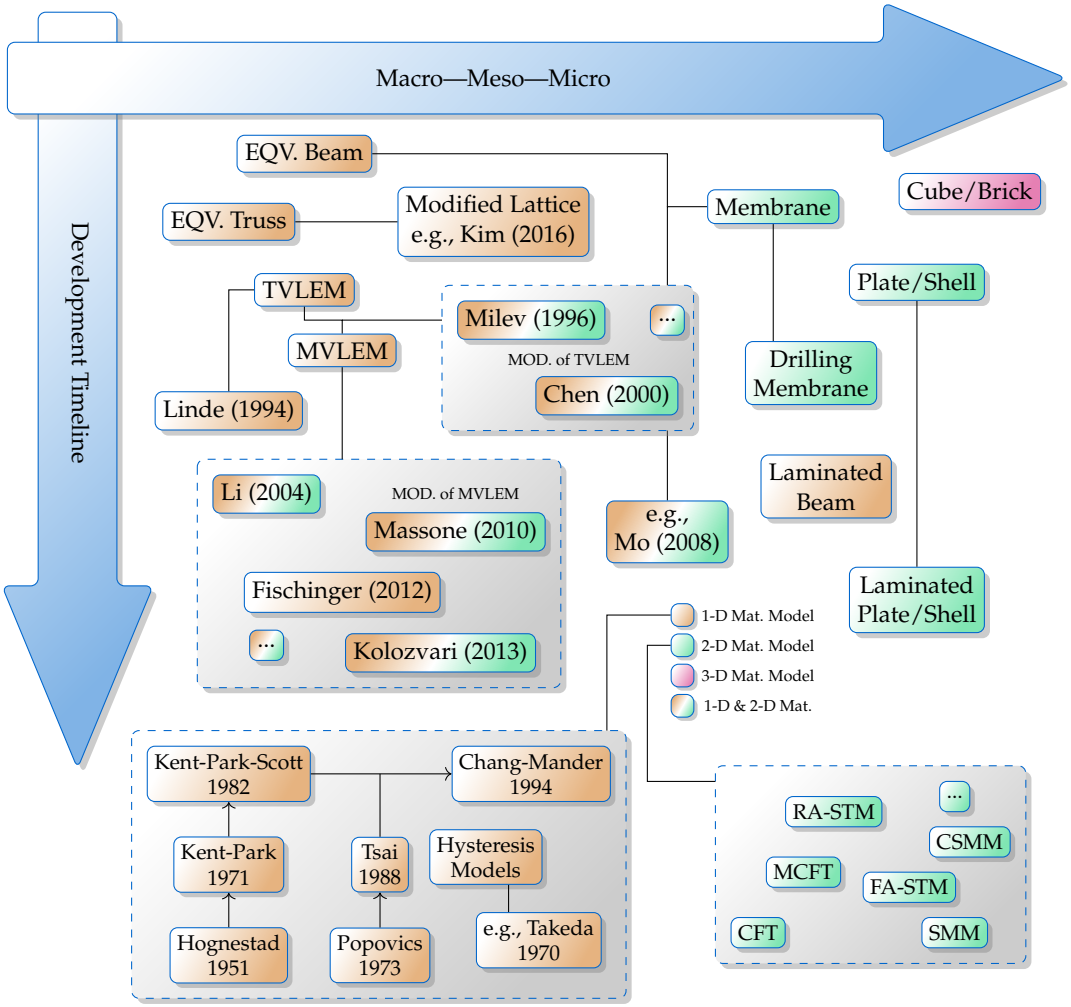


**FIGURE 2.8.** property matrix of current shear wall elements

## 2.2 SOME COMMENTS ON EXISTING ELEMENTS

Most existing macroscopic wall elements adopt formulations that consist of uniaxial material models. By the nature of those formulations, various effects, including shear-flexure in-

teraction, coupling between in-plane and out-of-plane actions, etc., cannot be easily produced. Essentially, modelling walls is a 2D problem that ought to be addressed in the 2D space with 2D tools. Some 1D formulations do bring great simplifications however they should not be expected to work well, especially when the biaxial response is significant. This section reviews some major issues in existing macroscopic wall elements, including beam/truss analogy, TVLEM/MVLEM and their variants. It could be deemed as the motivations of this project.

### 2.2.1 Beam/Truss Analogy

The classic beam analogy is a natural approach to shear wall simulation. If the target shear wall is slender enough, the corresponding transverse shear response would be negligible so that the overall behaviour is flexure dominated. In this case, a beam element is ideal due to its efficiency and simplicity. For walls in which beam theories do not apply, the beam analogy would perform poorly.

The truss analogy is another category of simple representations of 2D walls. Such an analogy is not only used in FEA but also in other engineering applications, for example the well known strut-and-tie model. As an approximation implemented in an equivalent manner, the truss analogy is able to perform properly with well tuned response of diagonal truss members. However, when it comes to the non-linear stage, it is in general difficult to define an equivalent hysteresis model for the diagonal trusses. Recent work (Lu and Panagiotou, 2014) adopts a reduction factor based on strains in both diagonal trusses. However, such a definition does not correspond to any solid mechanics theory. This means that such an equivalent approach cannot be used in blind predictions. Meanwhile, for validations of experiments, it is possible to obtain target response by simply tuning artificial/empirical parameters in either element or material model. It could be concluded that both calibration and reliability remain unpredictable with the truss analogy. Hence its applicability is limited.

### 2.2.2 MVLEM and SFI-MVLEM

MVLEM is well studied by researchers over the past decades. MVLEM is essentially a simplified version of Timoshenko beam and commonly known to be an efficient tool for slender wall modelling. However, similar to the beam/truss analogy, the application of MVLEM is limited to slender walls due to the difficulty in defining the non-linear shear response. Often,

piece-wise linear origin-oriented hysteresis models is used for shear response in practice. The calibration of those models remains an issue. Meanwhile, the concept of flexure centre, i.e., the location of the shear spring, is ambiguous and cannot be identified theoretically. The experimental observations of $c$ value scatter over a wide range from 0.2 to as high as 0.6, depending on wall geometries and loading conditions.

Practically, MVLEM is used to simulate shear walls with moderate to high aspect ratios (above 3.0) with a rigid shear response and a common $c$ value of 0.4. Noting that there is great flexibility in tuning element performance, manners of which include varying $c$ value, using empirical degradation models for the shear spring, etc., MVLEM is not reliable for blind predictions as well.

SFI-MVLEM is a modification of MVLEM. Instead of 1D springs, 2D panels/membranes, in particular four-node isoparametric quadrilaterals (Q4, or CPS4 in ABAQUS notation), are used as 'fibres' in SFI-MVLEM. It is claimed that this element can capture the shear-flexure interaction as it can produce a non-linear horizontal strain (or stress) distribution. However, this statement may not be true as the formulation lacks a theoretical basis. This type of elements suffers from the 'plane sections remain plane' assumption. Furthermore, two issues cannot be ignored in such a formulation.

### Low Accuracy

Q4 panels are generated internally in SFI-MVLEM according to the element formulation. However, the Q4 element is known to be sensitive to element geometry. The aspect ratio of each fibre can be neither too large nor too small since in which case Q4 may lock and thus very poor results would be computed. This means mesh refinement along wall height must be companioned by adding more fibres along the wall width to keep the aspect ratios of panel fibres around the same level. In extreme cases, numerical results may even **deteriorate** with improper mesh configurations. Meanwhile, due to the presence of the two end rigid bars and the artificial rotation centre, SFI-MVLEM does not converge to the true solution in most cases.

To illustrate this, a simple model is studied with different configurations shown as follows. The model illustrated in Fig. 2.9 is a cantilever beam with a prismatic rectangular cross section of unit thickness subjected to end shear. The distribution of shear stress at right end is not explicitly assigned, instead, its integration over the cross section is defined to be $P$. Assuming

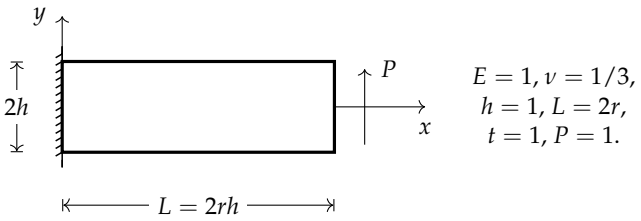


**FIGURE 2.9.** example cantilever beam model

a fully fixed boundary condition at the left end, the vertical tip deflection $v$, which can be obtained analytically via the semi-inverse method (see, e.g, Timoshenko, 1970), is

$$v = \frac{PL^3}{3EI} + \frac{Ph^2L}{2GI} = \frac{PL^3}{2Eh^3} + \frac{3PL(1+\nu)}{2Eh}. \tag{2.1}$$

Compared to the Euler-Bernoulli beam theory solution, the second term is the additional shear contribution. For parameters shown in Fig. 2.9, $v = 4r^3 + 4r$. Furthermore if the aspect ratio $r = 2$, the shear response comprises 20 % of total deflection.

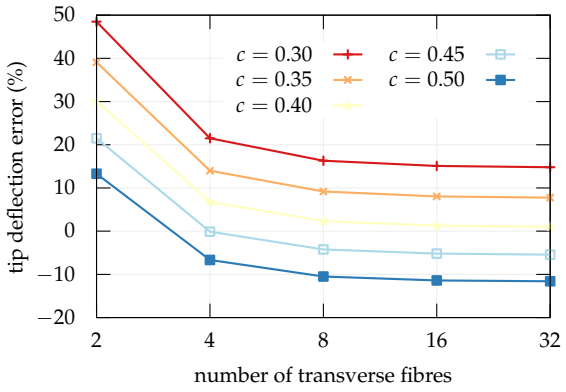


**(A)** two elements along cord

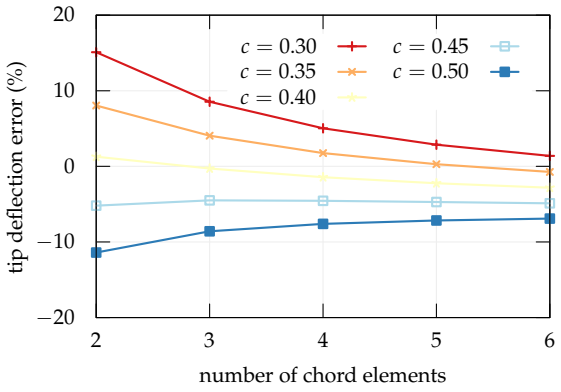


**(B)** sixteen fibres per element

**FIGURE 2.10.** sensitivity to mesh refinement in modelling a cantilever beam

As shown in Fig. 2.10, it is clear that the performance of SFI-MVLEM can be customized by simply adjusting the height of shear spring. Furthermore, mesh refinement does not guarantee convergence to analytical solution. With different configurations, the error of SFI-MVLEM is not strictly bounded as that in finite elements. Numerical investigations of the sensitivity to different aspect ratios, which are shown in Fig. 2.11, also lead to similar conclusions. There are four elements defined along the beam cord while sixteen fibres are assigned in each element. Interestingly, the rotation error does not change with different aspect ratios. The reference rotation values are not the analytical solutions as they are obtained from beam theory, which may not be suitable for short walls. Such a great uncertainty makes the calibration of SFI-

MVLEM extremely unreliable. It shall be stressed that only a simple linear elastic material model is used in this example, it would be more difficult to identify and isolate the error that stems from the element model when material nonlinearity is applied.

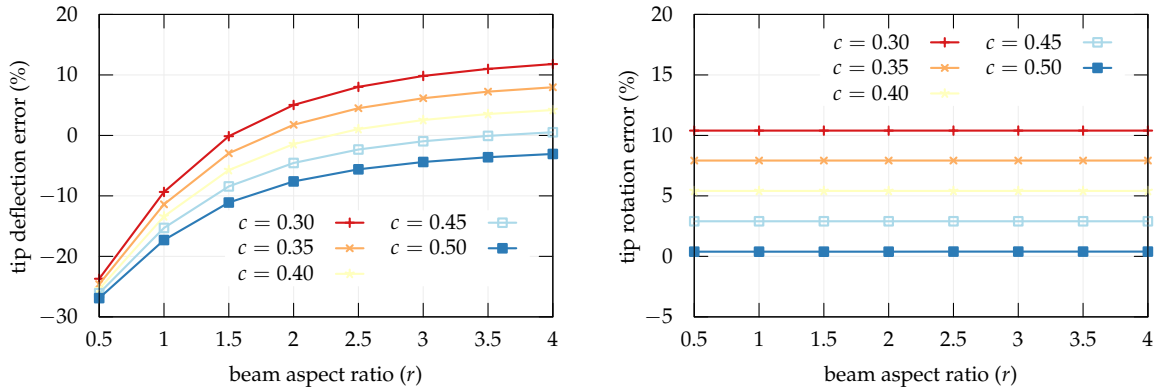


**(A)** deflection error **(B)** rotation error

**FIGURE 2.11.** sensitivity to aspect ratio with four SFI-MVLEM elements along cord

MVLEM has similar problems. Numerical results may converge to arbitrary solutions. In this sense, SFI-MVLEM does not essentially bring any improvement in accuracy. Furthermore, iterations are required in the current formulation to force either horizontal strain or stress to be zero (see Massone, 2010) so that internal history variables can be computed in state determination. Both assumptions of zero strain and zero stress are incorrect for walls.

### Hourglassing

SFI-MVLEM uses one integration point located at the centre of each fibre for numerical evaluation of fibre response. It is essentially equivalent to Q4 element with a reduced integration scheme (CPS4R in ABAQUS notation) and additional constraints. In this sense, SFI-MVLEM

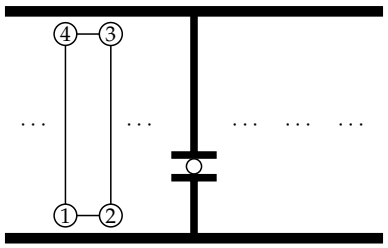


**FIGURE 2.12.** a typical fibre in SFI-MVLEM

can be deemed as a series of CPS4R element parallelly connected and sandwiched between two rigid bars. Consider a typical fibre as shown in Fig. 2.12. For a rectangular Q4 element,

three strain components (in the parent coordinate system) can be expressed in terms of nodal displacements.

$$\varepsilon_\xi = \frac{1}{4}\sum_{i=1}^{4}\xi_i u_i = \frac{1}{4}\left(-u_1 + u_2 + u_3 - u_4\right),$$
$$\varepsilon_\eta = \frac{1}{4}\sum_{i=1}^{4}\eta_i v_i = \frac{1}{4}\left(-v_1 - v_2 + v_3 + v_4\right),$$
$$\tau_{\xi\eta} = \frac{1}{4}\sum_{i=1}^{4}\left(\xi_i v_i + \eta_i u_i\right) = \frac{1}{4}\left(-v_1 + v_2 + v_3 - v_4 - u_1 - u_2 + u_3 + u_4\right).$$

Noting that in practice, fibres are often long and slim, viz., with large slenderness, it is feasible to assume

$$v_1 \approx v_2, \quad v_3 \approx v_4, \quad u_2 - u_1 \approx u_3 - u_4,$$

thus after isoparametric mapping,

$$\varepsilon_x = \frac{1}{b}\left(u_2 - u_1\right), \quad \varepsilon_y = \frac{1}{h}\left(v_3 - v_2\right), \quad \tau_{xy} = \frac{1}{h}\left(u_3 - u_2\right), \tag{2.2}$$

where $b$ and $h$ are the width and height of the target fibre respectively. Eq. (2.2) is used by SFI-MVLEM in strain computation. Apart from original $u_2$, $u_3$, $v_2$ and $v_3$, one additional variable $u_1$ is required in this process. The similar equations can also be obtained by assuming

$$v_2 - v_1 = v_4 - v_3, \quad u_3 - u_1 = u_2 - u_4.$$

This, however, corresponds to a hourglassing mode. Apparently, depending on how the final formula is interpreted, there is a potential risk of involving an hourglassing contribution into the strain computation as it is difficult to recover the 'true' deformation solely based on Eq. (2.2). Although the hourglassing effect is closely related to the loads and boundary conditions applied and may not be triggered in certain cases, the contribution of potential hourglassing modes should be fully eliminated otherwise the result could be over-flexible. This can also be seen in the previous example.

In the meantime, as the constructed 2D strain is partially artificial, it may or may not represent the true strain field, the computed response is less meaningful. Such a strategy is possibly nothing but GIGO (garbage in garbage out, computer science terminology).

#### Any Remedy?

So within the framework of current element formulation, is there any remedy to improve the performance? The answer to this question is probably negative. The potential hourglassing risk can be totally eliminated by using a full $2 \times 2$ integration scheme. However this quadruples computation effort and brings in other numerical issues. Another simple yet effective method is to include an additional displacement pattern to suppress the hourglassing effect. This can only be performed on the element level so all eight nodal forces (as of a normal Q4 element) need to be computed first. The geometry sensitivity cannot be addressed except for using other types of quadrilaterals, viz., higher order ones.

SFI-MVLEM shows a natural idea of addressing existing problems in modelling squat walls but its formulation has severe drawbacks. Given that SFI-MVLEM does not converge to analytical solutions and its error is often not bounded, analysts are **not recommended** to use this element in any modelling tasks.

### 2.2.3 Other Variants of TVLEM

Apart from the long-standing MVLEM and the recent modification SFI-MVLEM, other variants of TVLEM, as introduced in § 2.1.3, are rarely seen in practical simulations.

Replacing 1D springs with 2D plane stress elements is a conceptually reasonable approach. Since 2D plane stress elements can be used to simulate the complete behaviour of shear walls including all types of so called interactions, wrapping them into an 1D element by adding two rigid beams is unnecessary and more often less accurate, especially for squat walls. In this sense, the presence of rigid beams is only beneficial for reducing the number of nodes required to define the model. However, when it comes to modelling walls in multi-storey building, it is inevitable to define more nodes to take into consideration the effect of wall width. It can thus be concluded that to obtain more accurate simulation results, it would be better to directly use 2D plane stress elements.

### 2.2.4 Microscopic Finite Elements

Finite elements are general purpose tools for all kinds of simulations. No significant drawbacks exist except for potential low computational efficiency. Lower-order elements are in gen-

eral preferred due to both simpler mesh generation and lower computational cost. However, practically very dense mesh grids are required to obtain satisfactory results as the convergence is often slow. Higher-order elements have better accuracy, but they often require more computational effort and may not be well suited for dynamic problems. Meanwhile, the additional nodes that are located either on edges or the inside of elements are often undesirable. A more thorough discussion can be seen elsewhere (see Chapter 8, Belytschko et al., 2014).

## 2.3 THE PROPOSED APPROACH

It could be seen that, to date, most macroscopic elements involve a quite heavy use of truss/spring and beam elements, and thus do not possess a theoretical basis in terms of modelling 2D problems that the simulations of shear walls fit in. During the process of simplifying the 2D physical problems to 1D mathematical models, certain information would be discarded and cannot be recovered by simply adopting some empirical models. This fact leaves engineers with the other approach, the microscopic formulation. By construction, microscopic elements are suitable for simulating 2D solid mechanics problems. Most of the limitations of the 1D elements can be automatically eliminated, including the 'plane sections remain plane' assumption, shear-flexure interaction, etc.

As previously discussed, the main difficulty that hinders the application of microscopic elements to model shear wall structures lies in their high computation cost. One possible solution is to improve the coarse-mesh accuracy thus a reasonably accurate response could be obtained with a few elements (one or four) defined per sheet of wall. Meanwhile, adaptive analysis is automatically supported so that denser mesh grids could be assigned to critical regions of interest. This work aims to develop a new quadrilateral membrane element with high coarse-mesh accuracy that is suitable for different levels of simulations of shear walls (not limited to shear walls, but could also be any planar problems). The ultimate goal is to improve the accuracy-cost ratio and provide a reliable tool for simulations of various engineering problems.

# 3

# The GCMQ and SGCMQ Elements

This chapter describes the formulation details of the proposed GCMQ element and its simplified version SGCMQ, as well as other related aspects such as integration schemes, mass matrix formulation and discussions on computational cost.

Part of this chapter is published in the journal paper *A New Drilling Quadrilateral Membrane Element With High Coarse-Mesh Accuracy Using A Modified Hu-Washizu Principle* (Chang et al., 2019a) with **International Journal for Numerical Methods in Engineering**. Part of this chapter is also published in the journal paper *Numerical Evaluations of A Novel Membrane Element in Simulations of Reinforced Concrete Shear Walls* (Chang et al., 2019b) with **Engineering Structures**.

## 3.1 Introduction

The study of lower-order membrane elements is one of the focuses throughout the development of finite element methods (FEM). The very first elements (e.g., Turner et al., 1956; Taig and Kerr, 1964) were widely used in various applications and later adopted as elementary examples in many FEM textbooks (e.g., Zienkiewicz et al., 2013). In general, early elements are constructed based on the principle of minimum potential energy and convergence is normally guaranteed with refined mesh grids, provided the elements can pass the patch test (see Zienkiewicz and Taylor, 1997, for a more detailed discussion).

It is observed that these elements tend to be overstiff, particularly when subjected to in-

plane bending, and in general do not perform well with distorted geometry and large aspect ratios (Pian and Sumihara, 1984; Bergan and Felippa, 1985). Besides, conventional membrane elements also suffer from two other issues that limit their applications in simulating complex systems. The first problem happens when it comes to model connections between panels and beam-type elements, as traditional finite elements only have two degrees of freedom (DoFs) per node while beams possess the additional rotational DoFs. The second problem arises in the construction of some planar shell elements by combining membranes and plates together. Since the in-plane rotation DoF is absent, the corresponding main diagonal term is always zero, which leads to a singular element stiffness matrix. Although numerically it is possible to obtain usable elements by modifying the zero terms, the additional coupling effects between in-plane and out-of-plane actions cannot be properly captured. This can be a severe problem with coarse mesh configurations.

One possible solution is to introduce in-plane rotational degrees of freedom (also known as drilling DoFs) into the element formulation. Initial research on drilling membranes was carried out in 1960's (Felippa, 1966; Carr, 1967; Scordelis, 1967; Willam, 1969). The very first application in structural analysis can be traced back to the work by MacLeod (1969). Successful attempts were later made by others using higher order shape functions (Allman, 1984, 1988; Bergan and Felippa, 1985; Cook, 1986; MacNeal and Harder, 1988). The interpolation scheme used in Allman's element was also adopted by Sze et al. (1992), in which, instead of the displacement-based formulation, a two-field Hellinger-Reissner type formulation was used. It did give a more accurate result but additional treatments were required to suppress spurious energy modes. Long and Xu (1994) employed a different interpolation scheme via a generalized conforming approach. From a mathematical perspective, Hughes and Brezzi (1989) managed to derive a special variational principle, in which the drilling DoFs are bonded to the nodal rotation that is treated as an independent field. The corresponding element was evaluated by Hughes et al. (1995). The same principle was also employed by others (Ibrahimbegović et al., 1990; Ibrahimbegović and Frey, 1992; Ibrahimbegović, 1993, 1994; Chinosi et al., 1997). A similar concept was later adopted by Choi et al. (2002) in the derivation of a displacement-based element. Recent explorations can be spotted in the work by Fajman (2002); Cen et al. (2011, 2015); Madeo et al. (2012, 2014); Shang and Ouyang (2017).

Although some superior performance can be obtained (e.g., Choi et al., 2006; Choo et al.,

2006; Cen et al., 2011), most existing elements are constructed using the (modified) Hellinger-Reissner principle or the minimum complementary energy principle. Two main drawbacks cannot be ignored in those formulations: 1) there are difficulties in the use of those elements in non-linear plastic applications and 2) additional artificial parameters, the determination of which is normally empirical, may exist. Indeed, two-field formulations based on the Hellinger-Reissner variational principle are less desirable when it comes to non-linear applications since most material models are **strain controlled**. For recent approaches, such as establishing compatibility between different strains using stresses as weights (Wang et al., 2016; Shang and Ouyang, 2017), since interpolation functions involve material stiffness, whether those elements can be used in general non-linear applications remains unclear. Meanwhile, the overall performance could be further improved.

The ideal membrane element that could address those shortcomings, as well as the ones inherited from classic membranes, is expected to meet the aforementioned objectives. To this end, a four-node drilling quadrilateral membrane element called GCMQ is proposed via a mixed approach based on a modified four-field Hu-Washizu variational principle.

## 3.2 DEFORMATION DECOMPOSITION

### 3.2.1 Definition of Degrees of Freedom

For quadrilaterals, strictly speaking, there should be at least four DoFs per node (two for translations and two for independent distortions of both connected edges) to properly describe random deformation. But accounting for the compatibility with other existing elements, in this work, as a common practice, three DoFs are defined for each node: two for translation (denoted by $\boldsymbol{u}$ and $\boldsymbol{v}$) and one for rotation (denoted by $\boldsymbol{\theta}$).

Previous researches mainly provide two simple definitions of the drilling DoF $\boldsymbol{\theta}$: 1) nodal rigid body rotation (Allman, 1984) and 2) skew part of strain tensor (e.g., Carr, 1967; Hughes and Brezzi, 1989). However, those definitions have their own limitations, especially when it comes to the fully-fixed boundary condition in which case both fail to give zero values for drilling DoFs. Hence a more appropriate definition should be introduced. Meanwhile, the drilling displacement is expected to be decoupled from translation to simplify element formulation. By accounting for the above aspects, a definition similar to the one used by Sze et al.

(1992) and Long and Xu (1994) is adopted in this work. The exhaustive discussion of different definitions of $\boldsymbol{\theta}$ can be found elsewhere (Long et al., 2009).

### 3.2.2 Derivation of Independent Rotation Field

Let $\boldsymbol{F} : \boldsymbol{X} \rightarrow \boldsymbol{x}$ be a deformation, which is independent of time $t$. Accordingly, the current deformed configuration $\boldsymbol{x} \in \mathbb{R}^2$ can be interpreted as the result of applying mapping $\boldsymbol{F}$ to the undeformed configuration $\boldsymbol{X} \in \mathbb{R}^2$, that is

$$\boldsymbol{x} = \boldsymbol{F}(\boldsymbol{X}). \tag{3.1}$$

Similar to the multiplicative decomposition, it is feasible to decompose $\boldsymbol{F}$ into two phases. The first one is produced by translational DoFs, namely the translational part. The second one is generated by drilling DoFs, namely the drilling/distortion part. Let $\boldsymbol{T}$ and $\boldsymbol{D}$ denote these two parts, respectively. Then $\boldsymbol{F}$ can be expressed as

$$\boldsymbol{F} = \boldsymbol{D} \circ \boldsymbol{T}.$$

Let $\boldsymbol{x}_m$ denote the intermediate configuration obtained by solely applying mapping $\boldsymbol{T}$ to $\boldsymbol{X}$,

$$\boldsymbol{x}_m = \boldsymbol{T}(\boldsymbol{X}) = \boldsymbol{X} + \boldsymbol{u}_t(\boldsymbol{X}),$$

in which $\boldsymbol{u}_t$ is the translational deformation purely induced by the mapping $\boldsymbol{T}$. Then $\boldsymbol{x}$ can be expressed as a function of the intermediate configuration $\boldsymbol{x}_m$, through the mapping $\boldsymbol{D}$,

$$\boldsymbol{x} = \boldsymbol{D}(\boldsymbol{x}_m) = \boldsymbol{x}_m + \boldsymbol{u}_d(\boldsymbol{x}_m).$$

Hence Eq. (3.1) can be expanded as

$$\boldsymbol{x} = \boldsymbol{F}(\boldsymbol{X}) = \boldsymbol{D}(\boldsymbol{T}(\boldsymbol{X})) = \boldsymbol{X} + \boldsymbol{u}_t(\boldsymbol{X}) + \boldsymbol{u}_d(\boldsymbol{X} + \boldsymbol{u}_t(\boldsymbol{X})). \tag{3.2}$$

By using the Taylor series, one can expand the last term in Eq. (3.2) at $\boldsymbol{X}$ and obtain

$$\boldsymbol{x} = \boldsymbol{X} + \boldsymbol{u}_t(\boldsymbol{X}) + \boldsymbol{u}_d(\boldsymbol{X}) + \nabla \boldsymbol{u}_d(\boldsymbol{X}) \cdot \boldsymbol{u}_t(\boldsymbol{X}) + o(\boldsymbol{u}_t(\boldsymbol{X})),$$

where $\boldsymbol{u}_d$ is the drilling deformation and the last term is the Peano's remainder that stands for an infinitesimal term of higher order than $\boldsymbol{u}_t$. Within the framework of infinitesimal strain theory, it is reasonable to assume the deformation is sufficiently smooth that $\nabla \boldsymbol{u}_d \cdot \boldsymbol{u}_t$ is also an infinitesimal of higher order than both $\boldsymbol{u}_t$ and $\boldsymbol{u}_d$, which themselves are again higher order infinitesimals of $\boldsymbol{X}$. For simplicity, it is feasible to discard it, along with the remainder. By such, the total displacement field $\boldsymbol{u}$ can be simply written as

$$\boldsymbol{u} := \boldsymbol{x} - \boldsymbol{X} = \boldsymbol{u}_t + \boldsymbol{u}_d. \tag{3.3}$$

The graphical interpretation can be seen in Fig. 3.1. Such a decomposition cannot be applied in finite deformation problems, in which $\nabla \boldsymbol{u}_d \cdot \boldsymbol{u}_t$ could be significantly large. The decoupled displacement is important as it allows a great flexibility in the corresponding constructions of interpolations.

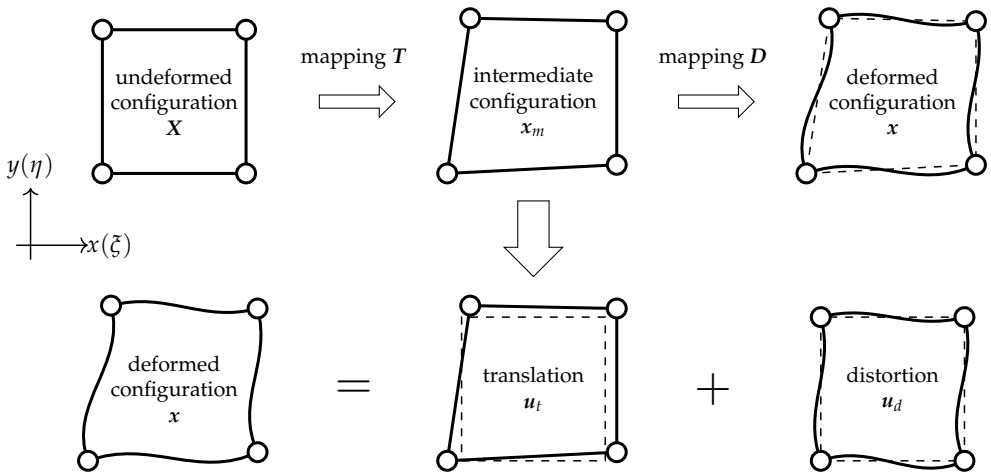


FIGURE 3.1. deformation decomposition

## 3.3 VARIATIONAL BASIS

### 3.3.1 The Hu-Washizu Principle

The general form of the Hu-Washizu variational principle (Hu, 1954) can be written as

$$\Pi_{HW}(\boldsymbol{u}, \boldsymbol{\varepsilon}, \boldsymbol{\sigma}) = \int_V \left[ W(\boldsymbol{\varepsilon}) + \boldsymbol{\sigma}^{\mathrm{T}} (\nabla \boldsymbol{u} - \boldsymbol{\varepsilon}) \right] \mathrm{d}V - \int_V \boldsymbol{b}^{\mathrm{T}} \boldsymbol{u} \, \mathrm{d}V - \int_{S_\sigma} \bar{\boldsymbol{t}}^{\mathrm{T}} \boldsymbol{u} \, \mathrm{d}S - \int_{S_u} \boldsymbol{t}^{\mathrm{T}} (\boldsymbol{u} - \bar{\boldsymbol{u}}) \, \mathrm{d}S,$$

in which $V$ denotes the volume domain, $S_\sigma$ and $S_u$ denote the corresponding boundaries, $W(\boldsymbol{\varepsilon})$ is the strain energy that is normally a non-linear function of the strain $\boldsymbol{\varepsilon}$, $\boldsymbol{\sigma}$ is the stress, $\boldsymbol{u}$ is the displacement field and $\bar{\boldsymbol{u}}$ is the prescribed boundary displacement. For brevity, it is feasible to replace the body force $\boldsymbol{b}$ term and the boundary traction $\bar{\boldsymbol{t}}$ term with the symbol

$$\Pi_{bt}(\boldsymbol{u}) = \int_V \boldsymbol{b}^{\mathrm{T}}\boldsymbol{u}\,\mathrm{d}V + \int_{S_\sigma} \bar{\boldsymbol{t}}^{\mathrm{T}}\boldsymbol{u}\,\mathrm{d}S,$$

since they are normally represented by the equivalent nodal loads that can be treated separately. Meanwhile, an additional field, called the enhanced strain $\hat{\boldsymbol{\varepsilon}}$, can be included to further tune element performance. Accounting for above aspects, the following simplified version $\Pi_S$, can be obtained.

$$\Pi_S(\boldsymbol{u}, \boldsymbol{\varepsilon}, \hat{\boldsymbol{\varepsilon}}, \boldsymbol{\sigma}) = \int_V \left[W(\boldsymbol{\varepsilon}) + \boldsymbol{\sigma}^{\mathrm{T}}(\nabla\boldsymbol{u} + \hat{\boldsymbol{\varepsilon}} - \boldsymbol{\varepsilon})\right]\mathrm{d}V - \int_{S_u} \boldsymbol{t}^{\mathrm{T}}(\boldsymbol{u} - \bar{\boldsymbol{u}})\,\mathrm{d}S - \Pi_{bt}(\boldsymbol{u}). \tag{3.4}$$

### 3.3.2 A Modified Variational Principle

It has been shown in Eq. (3.3) that the displacement field $\boldsymbol{u}$ can be decomposed into two independent portions $\boldsymbol{u}_t$ and $\boldsymbol{u}_d$ over the domain. By definition, the drilling portion $\boldsymbol{u}_d$ should be related to the in-plane rotation field $\boldsymbol{\theta}$ via a certain relationship. Similar to the approach adopted in beam elements, one may directly express $\boldsymbol{\theta}$ as a function of $\nabla\boldsymbol{u}_d$. If so, as the conformity requires $\boldsymbol{\theta}$ to be continuous on element boundaries, $\boldsymbol{u}_d$ has to be a two dimensional interpolation with $C_1$ continuity. It is commonly known to be very difficult to construct such a function. Instead of directly imposing the conforming condition, it is possible to handle those two requirements (conformity and $C_1$ continuity) separately. Noting that the $C_1$ continuity is only required on element boundaries, an auxiliary field, denoted by $\boldsymbol{u}_\theta$, that is a one-dimensional $C_1$ continuous function of $\boldsymbol{\theta}$ and resides only on boundaries, could be introduced. By such, the original $\boldsymbol{u}_d$ could simply be interpolated by any two-dimensional function and does not have to be conforming.

It could be noted that a proper interpolation for the translational displacement $\boldsymbol{u}_t$ could always be found so that

$$\boldsymbol{u}_t + \boldsymbol{u}_\theta = \bar{\boldsymbol{u}} \qquad \text{on } S_u, \tag{3.5}$$

given that $\boldsymbol{u}_\theta$ is already conforming by construction. By inserting Eq. (3.5) and Eq. (3.3) into Eq. (3.4), one obtains a new functional $\Pi_D$,

$$\Pi_D = \int_V \left[ W(\boldsymbol{\varepsilon}) + \boldsymbol{\sigma}^{\mathrm{T}} (\nabla \boldsymbol{u} + \hat{\boldsymbol{\varepsilon}} - \boldsymbol{\varepsilon}) \right] \mathrm{d}V + \int_{S_u} \boldsymbol{t}^{\mathrm{T}} (\boldsymbol{u}_\theta - \boldsymbol{u}_d) \, \mathrm{d}S - \Pi_{bt}, \tag{3.6}$$

with $\boldsymbol{u} = \boldsymbol{u}_t + \boldsymbol{u}_d$ and the conforming condition $\boldsymbol{u}_t + \boldsymbol{u}_\theta = \bar{\boldsymbol{u}}$ on $S_u$ as an essential condition. The displacement boundary $S_u$ term in the above functional, viz.,

$$\int_{S_u} \boldsymbol{t}^{\mathrm{T}} (\boldsymbol{u}_\theta - \boldsymbol{u}_d) \, \mathrm{d}S, \tag{3.7}$$

acts as a minimum conformity constraint imposed on $\boldsymbol{u}_d$ and $\boldsymbol{u}_\theta$ that guarantees convergence.

## 3.4 ELEMENT FORMULATION

### 3.4.1 A Simplification

Eq. (3.7) can be further relaxed by noting that when the element size approaches zero, the corresponding traction $\boldsymbol{t}$ approaches a constant field that can be denoted as $\boldsymbol{t}_c$. In which case, Eq. (3.7) can be rewritten as

$$\int_{S_u} \boldsymbol{t}_c^{\mathrm{T}} (\boldsymbol{u}_\theta - \boldsymbol{u}_d) \, \mathrm{d}S.$$

To avoid treating $\boldsymbol{u}_d$ separately, a slightly stronger constraint can be applied, for example,

$$\int_{S_i} \boldsymbol{I} (\boldsymbol{u}_d - \boldsymbol{u}_\theta) \, \mathrm{d}S = \int_{S_i} \boldsymbol{u}_d - \boldsymbol{u}_\theta \, \mathrm{d}S = \boldsymbol{0} \quad \text{for } i = 1, 2, 3, 4, \tag{3.8}$$

where $\boldsymbol{I}$ is the $2 \times 2$ identity matrix. In a more generic setup, it can also be expressed as

$$\int_{S_i} \boldsymbol{S} (\boldsymbol{u}_d - \boldsymbol{u}_\theta) \, \mathrm{d}S = \boldsymbol{0} \quad \text{for } i = 1, 2, 3, 4, \tag{3.9}$$

where $\boldsymbol{S}$ is a diagonal matrix with diagonal entries power functions of $S$, viz.,

$$\boldsymbol{S} = \begin{bmatrix} S^n & \\ & S^n \end{bmatrix}. \tag{3.10}$$

It should be noted that Eq. (3.8) is applied on four edges separately, hence instead of one, eight independent constraints (two for each edge) are provided. Eq. (3.8) is in fact identical to the constraint used in GQ12 element (Long and Xu, 1994). This approach is known as the generalized conforming method that can be initially observed in the work by Tang et al. (1984) and Wu et al. (1987) and later utilized, further enriched by Long and Xu (1994). Physically it means $\boldsymbol{u}_d$ and $\boldsymbol{u}_\theta$ are equivalent to each other in a weak sense on each element boundary.

Let $\boldsymbol{d}$ denote the generalised interpolation parameter used in $\boldsymbol{u}_d$ and assume $\boldsymbol{u}_\theta$ to be a function of the nodal rotation $\boldsymbol{\theta}$, it is possible to express $\boldsymbol{d}$ as a function of $\boldsymbol{\theta}$ by solving Eq. (3.8),

$$\boldsymbol{u}_d = f_1(\boldsymbol{d}) = f_1(f_2(\boldsymbol{\theta})) = f_3(\boldsymbol{\theta}),$$

although the solution is not guaranteed and depends on the discrete form of $\boldsymbol{u}_d$, this part will be discussed in the subsequent section. By such, the displacement $\boldsymbol{u}$ can be expressed solely by nodal translations and rotations. Meanwhile, Eq. (3.8) implies that Eq. (3.7) equals to zero in a generalised conforming sense. Hence, the governing variational principle Eq. (3.6) falls back to

$$\Pi_F(\boldsymbol{u}, \boldsymbol{\varepsilon}, \hat{\boldsymbol{\varepsilon}}, \boldsymbol{\sigma}) = \int_V \left[ W(\boldsymbol{\varepsilon}) + \boldsymbol{\sigma}^{\mathrm{T}} (\nabla \boldsymbol{u} + \hat{\boldsymbol{\varepsilon}} - \boldsymbol{\varepsilon}) \right] \mathrm{d}V - \Pi_{bt}(\boldsymbol{u}), \tag{3.11}$$

which is adopted in the formulation of the new element. It should be mentioned that Eq. (3.8) is not the only option. Eq. (3.7) could be replaced by various generalised conforming schemes. The interested reader is referred to the monograph (Long et al., 2009) for more details.

### 3.4.2 Solving Equations

Since the finally adopted functional is Eq. (3.11), the solving procedure of which has already been given elsewhere (Piltner and Taylor, 1995, 1999), here only a brief summary is presented. Nevertheless, it shall still be noted that in the following derivation, unlike in the original literature, the symmetry requirement is imposed on neither material stiffness nor any other matrices. The resulting state determination algorithm is universal for all kinds of material models. There is no penalty in terms of memory usage since full matrices need to be stored. Meanwhile, the state updating scheme is also corrected so that a stable algorithm is obtained.

Taking the variations of Eq. (3.4) gives,

$$\begin{cases} \int_V \delta\left(\nabla \boldsymbol{u}\right)^{\mathrm{T}} \boldsymbol{\sigma}\, \mathrm{d}V = \delta \boldsymbol{u}^{\mathrm{T}} \dfrac{\delta \Pi_{bt}}{\delta \boldsymbol{u}}, \\ \int_V \delta \boldsymbol{\sigma}^{\mathrm{T}} \left(\nabla \boldsymbol{u} + \hat{\boldsymbol{\varepsilon}} - \boldsymbol{\varepsilon}\right)\, \mathrm{d}V = 0, \\ \int_V \delta \boldsymbol{\varepsilon}^{\mathrm{T}} \left(\tilde{\boldsymbol{\sigma}}\left(\boldsymbol{\varepsilon}\right) - \boldsymbol{\sigma}\right)\, \mathrm{d}V = 0, \\ \int_V \delta \hat{\boldsymbol{\varepsilon}}^{\mathrm{T}} \boldsymbol{\sigma}\, \mathrm{d}V = 0, \end{cases} \tag{3.12}$$

where $\tilde{\boldsymbol{\sigma}}\left(\boldsymbol{\varepsilon}\right) = \partial W\left(\boldsymbol{\varepsilon}\right)/\partial \boldsymbol{\varepsilon}$ is the stress obtained from the material model. By discretising the four independent fields with

$$\boldsymbol{u} = \boldsymbol{\phi}_u \boldsymbol{q}, \qquad \boldsymbol{\sigma} = \boldsymbol{\phi}_\sigma \boldsymbol{\alpha}, \qquad \boldsymbol{\varepsilon} = \boldsymbol{\phi}_\varepsilon \boldsymbol{\beta}, \qquad \hat{\boldsymbol{\varepsilon}} = \boldsymbol{\phi}_{\hat{\varepsilon}} \boldsymbol{\zeta},$$

Eq. (3.12) can also be expressed as

$$\begin{cases} \delta \boldsymbol{q}^{\mathrm{T}} \int_V \left(\boldsymbol{L}\boldsymbol{\phi}_u\right)^{\mathrm{T}} \boldsymbol{\phi}_\sigma \boldsymbol{\alpha}\, \mathrm{d}V = \delta \boldsymbol{q}^{\mathrm{T}} \dfrac{\delta \Pi_{bt}}{\delta \boldsymbol{q}} = \delta \boldsymbol{q}^{\mathrm{T}} \boldsymbol{P}, \\ \delta \boldsymbol{\alpha}^{\mathrm{T}} \int_V \boldsymbol{\phi}_\sigma^{\mathrm{T}} \left(\boldsymbol{L}\boldsymbol{\phi}_u \boldsymbol{q} + \boldsymbol{\phi}_{\hat{\varepsilon}} \boldsymbol{\zeta} - \boldsymbol{\phi}_\varepsilon \boldsymbol{\beta}\right)\, \mathrm{d}V = 0, \\ \delta \boldsymbol{\beta}^{\mathrm{T}} \int_V \boldsymbol{\phi}_\varepsilon^{\mathrm{T}} \left(\tilde{\boldsymbol{\sigma}}\left(\boldsymbol{\varepsilon}\right) - \boldsymbol{\phi}_\sigma \boldsymbol{\alpha}\right)\, \mathrm{d}V = 0, \\ \delta \boldsymbol{\zeta}^{\mathrm{T}} \int_V \boldsymbol{\phi}_{\hat{\varepsilon}}^{\mathrm{T}} \boldsymbol{\phi}_\sigma \boldsymbol{\alpha}\, \mathrm{d}V = 0. \end{cases} \tag{3.13}$$

The corresponding linearised equations between two iterations denoted with pseudo-time $t_n$ and $t_{n+1}$ could be obtained as

$$\begin{cases} \int_V \left(\boldsymbol{L}\boldsymbol{\phi}_u\right)^{\mathrm{T}} \boldsymbol{\phi}_\sigma \Delta\boldsymbol{\alpha}\, \mathrm{d}V = \boldsymbol{P}_{n+1} - \boldsymbol{P}_n, \\ \int_V \boldsymbol{\phi}_\sigma^{\mathrm{T}} \left(\boldsymbol{L}\boldsymbol{\phi}_u \Delta\boldsymbol{q} + \boldsymbol{\phi}_{\hat{\varepsilon}} \Delta\boldsymbol{\zeta} - \boldsymbol{\phi}_\varepsilon \Delta\boldsymbol{\beta}\right)\, \mathrm{d}V = \boldsymbol{0}, \\ \int_V \boldsymbol{\phi}_\varepsilon^{\mathrm{T}} \left(\tilde{\boldsymbol{E}}\boldsymbol{\phi}_\varepsilon \Delta\boldsymbol{\beta} - \boldsymbol{\phi}_\sigma \Delta\boldsymbol{\alpha}\right)\, \mathrm{d}V = -\boldsymbol{Q}_n, \\ \int_V \boldsymbol{\phi}_{\hat{\varepsilon}}^{\mathrm{T}} \boldsymbol{\phi}_\sigma \Delta\boldsymbol{\alpha}\, \mathrm{d}V = -\boldsymbol{F}_n, \end{cases} \tag{3.14}$$

in which $\boldsymbol{P}_{n+1}$ stands for the external load that could include the contributions of nodal forces, body forces and/or surface tractions. The increment of the material stress $\Delta\tilde{\boldsymbol{\sigma}}$ is linearised with

the tangent stiffness $\tilde{\boldsymbol{E}}$ that could also be obtained from the material model,

$$\Delta\tilde{\boldsymbol{\sigma}} \approx \tilde{\boldsymbol{E}}\Delta\boldsymbol{\varepsilon} = \tilde{\boldsymbol{E}}\boldsymbol{\phi}_{\varepsilon}\Delta\boldsymbol{\beta}. \tag{3.15}$$

The gradient operator $\boldsymbol{L}$ could be expressed as

$$\boldsymbol{L} = \begin{bmatrix} \partial/\partial x & \cdot & \partial/\partial y \\ \cdot & \partial/\partial y & \partial/\partial x \end{bmatrix}^{\mathrm{T}},$$

where $x$ and $y$ are global coordinates. The resistance $\boldsymbol{P}_n$, the residuals $\boldsymbol{Q}_n$ and $\boldsymbol{F}_n$ are

$$\boldsymbol{P}_n = \int_V (\boldsymbol{L}\boldsymbol{\phi}_u)^{\mathrm{T}} \boldsymbol{\phi}_{\sigma}\boldsymbol{\alpha}_n \,\mathrm{d}V, \tag{3.16}$$

$$\boldsymbol{Q}_n = \int_V \boldsymbol{\phi}_{\varepsilon}^{\mathrm{T}}\tilde{\boldsymbol{\sigma}}_n - \boldsymbol{\phi}_{\varepsilon}^{\mathrm{T}}\boldsymbol{\phi}_{\sigma}\boldsymbol{\alpha}_n \,\mathrm{d}V, \tag{3.17}$$

$$\boldsymbol{F}_n = \int_V \boldsymbol{\phi}_{\hat{\varepsilon}}^{\mathrm{T}}\boldsymbol{\phi}_{\sigma}\boldsymbol{\alpha}_n \,\mathrm{d}V. \tag{3.18}$$

The non-zero term $\boldsymbol{F}_n$ origins from a relaxed version of the fourth equation in Eq. (3.12), which represents a full orthogonality condition that should be enforced on the enhanced strain $\hat{\boldsymbol{\varepsilon}}$. However, with such a condition, it is difficult to recover the magnitude of $\hat{\boldsymbol{\varepsilon}}$. Hence, instead of the original condition, a partially orthogonal one can be adopted (Simo and Rifai, 1990; Piltner and Taylor, 1995), that is

$$\int_V \delta\hat{\boldsymbol{\varepsilon}}^{\mathrm{T}}\hat{\boldsymbol{\sigma}} \,\mathrm{d}V = \boldsymbol{0},$$

in which $\hat{\boldsymbol{\sigma}}$ is a reference stress field consists of at least three constant modes. If the adopted stress interpolation employs higher order polynomials, the original expression does not necessarily equal to zero for all non-converged iterations. The selection of the enhanced strain will be further discussed later.

By further denoting

$$\boldsymbol{H} = \int_V \boldsymbol{\phi}_{\sigma}^{\mathrm{T}}\boldsymbol{\phi}_{\varepsilon}\mathrm{d}V, \quad \tilde{\boldsymbol{H}} = \int_V \boldsymbol{\phi}_{\varepsilon}^{\mathrm{T}}\tilde{\boldsymbol{E}}\boldsymbol{\phi}_{\varepsilon}\mathrm{d}V, \quad \boldsymbol{M} = \int_V \boldsymbol{\phi}_{\sigma}^{\mathrm{T}}\boldsymbol{\phi}_{\hat{\varepsilon}}\mathrm{d}V, \quad \boldsymbol{N} = \int_V \boldsymbol{\phi}_{\sigma}^{\mathrm{T}}\boldsymbol{L}\boldsymbol{\phi}_u\mathrm{d}V, \tag{3.19}$$

the system of linear equations can be obtained as

$$\begin{bmatrix} \cdot & \boldsymbol{N}^{\mathrm{T}} & \cdot & \cdot \\ \boldsymbol{N} & \cdot & -\boldsymbol{H} & \boldsymbol{M} \\ \cdot & -\boldsymbol{H}^{\mathrm{T}} & \tilde{\boldsymbol{H}} & \cdot \\ \cdot & \boldsymbol{M}^{\mathrm{T}} & \cdot & \cdot \end{bmatrix} \begin{bmatrix} \Delta\boldsymbol{q} \\ \Delta\boldsymbol{\alpha} \\ \Delta\boldsymbol{\beta} \\ \Delta\boldsymbol{\zeta} \end{bmatrix} = \begin{bmatrix} \boldsymbol{P}_{n+1} - \boldsymbol{P}_n \\ \boldsymbol{0} \\ -\boldsymbol{Q}_n \\ -\boldsymbol{F}_n \end{bmatrix}. \tag{3.20}$$

### 3.4.3 Solution Procedure

The traditional local iterative scheme can be adopted for solving Eq. (3.20). From the third equation in Eq. (3.20), $\Delta\boldsymbol{\beta}$ can be expressed as

$$\Delta\boldsymbol{\beta} = \tilde{\boldsymbol{H}}^{-1}\left(\boldsymbol{H}^{\mathrm{T}}\Delta\boldsymbol{\alpha} - \boldsymbol{Q}_n\right),$$

assuming $\tilde{\boldsymbol{H}}$ is invertible, inserting it into the second equation, one obtains

$$\Delta\boldsymbol{\alpha} = \left(\boldsymbol{H}\tilde{\boldsymbol{H}}^{-1}\boldsymbol{H}^{\mathrm{T}}\right)^{-1}\left(\boldsymbol{N}\Delta\boldsymbol{q} + \boldsymbol{M}\Delta\boldsymbol{\zeta} + \boldsymbol{H}\tilde{\boldsymbol{H}}^{-1}\boldsymbol{Q}_n\right).$$

However, if $\boldsymbol{H}$ is square and invertible, the stress interpolation parameter $\boldsymbol{\alpha}$ could be directly updated according to the third equation in Eq. (3.13), that is

$$\boldsymbol{\alpha} = \boldsymbol{H}^{-\mathrm{T}}\int_V \boldsymbol{\phi}_\varepsilon^{\mathrm{T}}\tilde{\sigma}\,\mathrm{d}V. \tag{3.21}$$

It could be seen that $\boldsymbol{\alpha}$ only depends on the material stress $\tilde{\sigma}$ and can be computed immediately after updating the material state. Since the equilibrium is enforced, the corresponding residual simply equals to zero,

$$\boldsymbol{Q}_n = \boldsymbol{0}.$$

Meanwhile, $\Delta\boldsymbol{\beta}$ can be directly obtained from the second equation as

$$\Delta\boldsymbol{\beta} = \tilde{\boldsymbol{N}}\Delta\boldsymbol{q} + \tilde{\boldsymbol{M}}\Delta\boldsymbol{\zeta}, \tag{3.22}$$

in which $\tilde{\boldsymbol{N}} = \boldsymbol{H}^{-1}\boldsymbol{N}$ and $\tilde{\boldsymbol{M}} = \boldsymbol{H}^{-1}\boldsymbol{M}$.

The remaining equations can be rearranged as

$$\begin{bmatrix} \boldsymbol{U} & \boldsymbol{W} \\ \boldsymbol{W}^{\mathrm{T}} & \boldsymbol{V} \end{bmatrix} \begin{bmatrix} \Delta \boldsymbol{q} \\ \Delta \boldsymbol{\zeta} \end{bmatrix} = \begin{bmatrix} \boldsymbol{P}_{n+1} - \boldsymbol{P}_n \\ -\boldsymbol{F}_n \end{bmatrix},$$

in which

$$\boldsymbol{U} = \tilde{\boldsymbol{N}}^{\mathrm{T}} \tilde{\boldsymbol{H}} \tilde{\boldsymbol{N}}, \quad \boldsymbol{V} = \tilde{\boldsymbol{M}}^{\mathrm{T}} \tilde{\boldsymbol{H}} \tilde{\boldsymbol{M}}, \quad \boldsymbol{W} = \tilde{\boldsymbol{N}}^{\mathrm{T}} \tilde{\boldsymbol{H}} \tilde{\boldsymbol{M}}. \tag{3.23}$$

By repeating the condensation procedure, one could obtain

$$\Delta \boldsymbol{\zeta} = \boldsymbol{V}^{-1} \left( -\boldsymbol{F}_n - \boldsymbol{W}^{\mathrm{T}} \Delta \boldsymbol{q} \right), \tag{3.24}$$

which leads to the final expression of the equivalent stiffness $\boldsymbol{K}$

$$\boldsymbol{K} = \boldsymbol{U} - \boldsymbol{W} \boldsymbol{V}^{-1} \boldsymbol{W}^{\mathrm{T}}, \tag{3.25}$$

while the equivalent resistance $\boldsymbol{R}$ is

$$\boldsymbol{R} = \boldsymbol{P}_n - \boldsymbol{W} \boldsymbol{V}^{-1} \boldsymbol{F}_n. \tag{3.26}$$

It should be noted that the above procedure can largely reduce computation cost but is only valid for an invertible $\boldsymbol{H}$. It is, in general, easy to construct a valid $\boldsymbol{H}$. Otherwise a standard condensation should be conducted on Eq. (3.20). Another major difference between those two procedures is that the standard condensation requires $\tilde{\boldsymbol{H}}$ to be invertible while the presented one requires $\boldsymbol{V}$ to be invertible. Noting that $\boldsymbol{V}$ is a smaller matrix, it is less likely for $\boldsymbol{V}$ to be singular compared to $\boldsymbol{H} \tilde{\boldsymbol{H}}^{-1} \boldsymbol{H}^{\mathrm{T}}$. Stability could be potentially improved with the new procedure.

### 3.4.4 Implementation Algorithm

For state determination at the element level, here a non-iterative scheme is presented in Algorithm 1 where $w^i$ denotes the overall numerical integration weight that could include original integration weight, element thickness and determinant of the Jacobian matrix at the corresponding integration point.

It should be noted that $\boldsymbol{H}$, $\boldsymbol{M}$, $\boldsymbol{N}$, $\tilde{\boldsymbol{M}}$ and $\tilde{\boldsymbol{N}}$ are all constant matrices. Once the corresponding shape functions are chosen, they could be readily computed, stored and later used in analyses. Meanwhile, $\boldsymbol{U}$, $\boldsymbol{V}$ and $\boldsymbol{W}$ solely depend on the material tangent $\tilde{\boldsymbol{E}}$ that should be computed according to given strain $\boldsymbol{\varepsilon}$ and/or other variables. Accordingly, they could be initialized, stored and updated as element level history variables during iterations.

**Algorithm 1:** state determination at element level

**Input:** $\Delta\boldsymbol{q}$, $\boldsymbol{q}_n$, $\boldsymbol{\alpha}_n$, $\boldsymbol{\beta}_n$, $\boldsymbol{\zeta}_n$, $\boldsymbol{V}_n$, $\boldsymbol{W}_n$
**Output:** $\boldsymbol{K}$, $\boldsymbol{R}$, $\boldsymbol{q}_{n+1}$, $\boldsymbol{\alpha}_{n+1}$, $\boldsymbol{\beta}_{n+1}$, $\boldsymbol{\zeta}_{n+1}$, $\boldsymbol{V}_{n+1}$, $\boldsymbol{W}_{n+1}$
**initialize** constant matrices if necessary;
**compute** $\Delta\boldsymbol{\zeta} = -\boldsymbol{V}_n^{-1}\boldsymbol{M}^{\mathrm{T}}\boldsymbol{\alpha}_n - \boldsymbol{V}_n^{-1}\boldsymbol{W}_n^{\mathrm{T}}\Delta\boldsymbol{q}$; // Eq. (3.24)
**compute** $\Delta\boldsymbol{\beta} = \tilde{\boldsymbol{N}}\Delta\boldsymbol{q} + \tilde{\boldsymbol{M}}\Delta\boldsymbol{\zeta}$; // Eq. (3.22)
**update** $\boldsymbol{q}_{n+1} = \boldsymbol{q}_n + \Delta\boldsymbol{q}$;
**update** $\boldsymbol{\zeta}_{n+1} = \boldsymbol{\zeta}_n + \Delta\boldsymbol{\zeta}$;
**update** $\boldsymbol{\beta}_{n+1} = \boldsymbol{\beta}_n + \Delta\boldsymbol{\beta}$;
**forall** integration points **do**
  **compute** $\boldsymbol{\varepsilon}^i_{n+1} = \boldsymbol{\phi}^i_\varepsilon\boldsymbol{\beta}_{n+1}$;
  **compute** $\tilde{\boldsymbol{E}}^i_{n+1}$, $\tilde{\boldsymbol{\sigma}}^i_{n+1}$ from material models;
  **assemble** $\tilde{\boldsymbol{H}}_{n+1} = \sum w^i\boldsymbol{\phi}^{i,\mathrm{T}}_\varepsilon\tilde{\boldsymbol{E}}^i_{n+1}\boldsymbol{\phi}^i_\varepsilon$;
  **assemble** $\tilde{\boldsymbol{S}}_{n+1} = \sum w^i\boldsymbol{\phi}^{i,\mathrm{T}}_\varepsilon\tilde{\boldsymbol{\sigma}}^i_{n+1}$;
**end**
**compute** $\boldsymbol{\alpha}_{n+1} = \boldsymbol{H}^{-\mathrm{T}}\tilde{\boldsymbol{S}}_{n+1}$; // Eq. (3.21)
**update** $\boldsymbol{U}_{n+1}$, $\boldsymbol{V}_{n+1}$, $\boldsymbol{W}_{n+1}$ using $\tilde{\boldsymbol{H}}_{n+1}$; // Eq. (3.23)
**compute** $\boldsymbol{K} = \boldsymbol{U}_{n+1} - \boldsymbol{W}_{n+1}\boldsymbol{V}^{-1}_{n+1}\boldsymbol{W}^{\mathrm{T}}_{n+1}$; // Eq. (3.25)
**compute** $\boldsymbol{R} = \boldsymbol{N}\boldsymbol{\alpha}_{n+1} - \boldsymbol{W}_{n+1}\boldsymbol{V}^{-1}_{n+1}\boldsymbol{M}^{\mathrm{T}}\boldsymbol{\alpha}_{n+1}$; // Eq. (3.26)
**return**;

## 3.5 CONSTRUCTION OF INTERPOLATIONS

### 3.5.1 Displacement

As a conventional approach, the translational part of displacement field $\boldsymbol{u}_t$ is interpolated by nodal translations via an isoparametric mapping, that is,

$$\boldsymbol{\phi}_t = \begin{bmatrix} N_1 & 0 & N_2 & 0 & N_3 & 0 & N_4 & 0 \\ 0 & N_1 & 0 & N_2 & 0 & N_3 & 0 & N_4 \end{bmatrix}$$

with

$$N_i = \frac{1}{4}\left(1+\xi\xi_i\right)\left(1+\eta\eta_i\right),$$

in which $\xi_i$ and $\eta_i$ are parent coordinates of corresponding nodes. Then $\boldsymbol{u}_t$ is expressed as

$$\boldsymbol{u}_t = \begin{bmatrix} u_t & v_t \end{bmatrix}^{\mathrm{T}} = \boldsymbol{\phi}_t \boldsymbol{q}_t, \tag{3.27}$$

in which $\boldsymbol{q}_t = \begin{bmatrix} u_1 & v_1 & u_2 & v_2 & u_3 & v_3 & u_4 & v_4 \end{bmatrix}^{\mathrm{T}}$ consists of translational nodal displacements.

For the drilling part $\boldsymbol{u}_d$, the corresponding shape functions can be in fact arbitrarily chosen as no $C_1$ continuity is imposed.

$$\boldsymbol{u}_d = \begin{bmatrix} u_d & v_d \end{bmatrix}^{\mathrm{T}} = \boldsymbol{\phi}_d \boldsymbol{d}. \tag{3.28}$$

Since the bilinear terms have already been included in the translational part, higher order terms could be picked in $\boldsymbol{u}_d$. One possible choice is a serendipity-like basis. Mimicking a similar form used for $\boldsymbol{\phi}_t$, $\boldsymbol{\phi}_d$ can be written as

$$\boldsymbol{\phi}_d = \begin{bmatrix} \bar{N}_1 & 0 & \bar{N}_2 & 0 & \bar{N}_3 & 0 & \bar{N}_4 & 0 \\ 0 & \bar{N}_1 & 0 & \bar{N}_2 & 0 & \bar{N}_3 & 0 & \bar{N}_4 \end{bmatrix} \tag{3.29}$$

with

$$\bar{N}_1 = 1-\xi^2, \quad \bar{N}_2 = \eta-\xi^2\eta, \quad \bar{N}_3 = 1-\eta^2, \quad \bar{N}_4 = \xi-\xi\eta^2. \tag{3.30}$$

Accordingly, $\boldsymbol{d}$ consists of eight generalized interpolation parameters that do not need to possess any physical meaning, although with Eq. (3.30), they correspond to the displacement values of centres of four edges.

$$\boldsymbol{d} = \begin{bmatrix} d_1 & d_2 & d_3 & d_4 & d_5 & d_6 & d_7 & d_8 \end{bmatrix}^{\mathrm{T}}.$$

For the boundary version $\boldsymbol{u}_\theta$, to satisfy the imposed $C_1$ continuity requirement, it is feasible to choose the Hermite interpolation or other parametric curves (e.g., splines) as the shape

functions. Here in this work a Hermite-type curve constructed by two nodal rotations $\theta_i$ are adopted. For each edge $l_j$,

$$\boldsymbol{u}_\theta = \left[w_j\right] = \sum_{i=1}^{2} \tilde{N}_i \theta_i,$$

in which $w_j$ is the displacement perpendicular to the edge since this is a beam-type interpolation, and

$$\tilde{N}_1 = \frac{l_j}{8}\left(s^3 - s^2 - s + 1\right), \quad \tilde{N}_2 = \frac{l_j}{8}\left(s^3 + s^2 - s - 1\right),$$

where the edge label $l_j$ is also used to denote the length of that edge and $-1 \leqslant s \leqslant 1$ is the parent coordinate. There are several methods to transform the displacement $w_j$ from the local system to the global one as depicted in Fig. 3.2. Here a simple decomposition is used.

$$\boldsymbol{u}_\theta = \begin{bmatrix} u_\theta \\ v_\theta \end{bmatrix} = w_j \begin{bmatrix} \cos\left(\psi_j + \dfrac{\pi}{2}\right) \\ \sin\left(\psi_j + \dfrac{\pi}{2}\right) \end{bmatrix} = w_j \begin{bmatrix} -\sin\psi_j \\ \cos\psi_j \end{bmatrix}. \tag{3.31}$$

where $\psi_j$ is the inclination of the edge. Other curves may be used as substitutes. Additional internal parameters can also be introduced to further control the deformation.

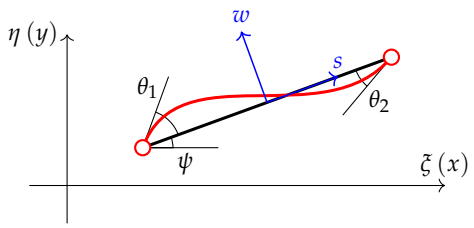


**FIGURE 3.2.** illustration of coordinate systems

Now Eq. (3.8) can be established explicitly. It provides eight independent constraints, which can be expanded as

$$\int_{S_1} \boldsymbol{u}_d \,\mathrm{d}S = \int_{S_1} \boldsymbol{u}_\theta \,\mathrm{d}S, \qquad \int_{S_2} \boldsymbol{u}_d \,\mathrm{d}S = \int_{S_2} \boldsymbol{u}_\theta \,\mathrm{d}S,$$
$$\int_{S_3} \boldsymbol{u}_d \,\mathrm{d}S = \int_{S_3} \boldsymbol{u}_\theta \,\mathrm{d}S, \qquad \int_{S_4} \boldsymbol{u}_d \,\mathrm{d}S = \int_{S_4} \boldsymbol{u}_\theta \,\mathrm{d}S.$$

The integrations can be performed analytically for both $\boldsymbol{u}_\theta$ and $\boldsymbol{u}_d$. By collecting all equations

and rearranging them into a matrix form, one obtains

$$\boldsymbol{G}\boldsymbol{d} = \boldsymbol{Q}\boldsymbol{\theta}, \tag{3.32}$$

with $\boldsymbol{\theta} = \begin{bmatrix} \theta_1 & \theta_2 & \theta_3 & \theta_4 \end{bmatrix}^{\mathrm{T}}$, $\boldsymbol{G}$ and $\boldsymbol{Q}$ are explicitly shown as in Eq. (3.33).

$$\underset{8\times 4}{\boldsymbol{Q}} = \int_{-1}^{1} \operatorname{diag} \begin{pmatrix} -\sin\psi_1 \\ \cos\psi_1 \\ -\sin\psi_2 \\ \cos\psi_2 \\ -\sin\psi_3 \\ \cos\psi_3 \\ -\sin\psi_4 \\ \cos\psi_4 \end{pmatrix} \cdot \begin{bmatrix} \tilde{N}_1 & \tilde{N}_2 & \cdot & \cdot \\ \tilde{N}_1 & \tilde{N}_2 & \cdot & \cdot \\ \cdot & \tilde{N}_1 & \tilde{N}_2 & \cdot \\ \cdot & \tilde{N}_1 & \tilde{N}_2 & \cdot \\ \cdot & \cdot & \tilde{N}_1 & \tilde{N}_2 \\ \cdot & \cdot & \tilde{N}_1 & \tilde{N}_2 \\ \tilde{N}_2 & \cdot & \cdot & \tilde{N}_1 \\ \tilde{N}_2 & \cdot & \cdot & \tilde{N}_1 \end{bmatrix} \mathrm{d}s, \quad \underset{8\times 8}{\boldsymbol{G}} = \begin{bmatrix} \int_{-1}^{1} \boldsymbol{\phi}_d\big|_{\eta=-1}\,\mathrm{d}\xi \\ \int_{-1}^{1} \boldsymbol{\phi}_d\big|_{\xi=1}\,\mathrm{d}\eta \\ \int_{-1}^{1} \boldsymbol{\phi}_d\big|_{\eta=1}\,\mathrm{d}\xi \\ \int_{-1}^{1} \boldsymbol{\phi}_d\big|_{\xi=-1}\,\mathrm{d}\eta \end{bmatrix}. \tag{3.33}$$

Assume $\boldsymbol{G}$ is invertible, then

$$\boldsymbol{d} = \boldsymbol{G}^{-1}\boldsymbol{Q}\boldsymbol{\theta}, \tag{3.34}$$

inserting Eq. (3.34) into Eq. (3.28), $\boldsymbol{u}_d$ can eventually be expressed by $\boldsymbol{\theta}$, which consists of four nodal rotations.

$$\boldsymbol{u}_d = \boldsymbol{\phi}_d\boldsymbol{d} = \boldsymbol{\phi}_d\boldsymbol{G}^{-1}\boldsymbol{Q}\boldsymbol{\theta}. \tag{3.35}$$

Then Eq. (3.3) can be reinterpreted by $\boldsymbol{q}_t$ and $\boldsymbol{\theta}$,

$$\boldsymbol{u} = \boldsymbol{u}_t + \boldsymbol{u}_d = \boldsymbol{\phi}_t\boldsymbol{q}_t + \boldsymbol{\phi}_d\boldsymbol{G}^{-1}\boldsymbol{Q}\boldsymbol{\theta}. \tag{3.36}$$

Accordingly,

$$\boldsymbol{\phi}_u = \begin{bmatrix} \boldsymbol{\phi}_t & \boldsymbol{\phi}_d\boldsymbol{G}^{-1}\boldsymbol{Q} \end{bmatrix}, \qquad \boldsymbol{q} = \begin{bmatrix} \boldsymbol{q}_t & \boldsymbol{\theta} \end{bmatrix}^{\mathrm{T}}.$$

The order of $\boldsymbol{q}$ could be rearranged to fit the corresponding DoF encoding rule. As there is no additional constraint imposed, $\boldsymbol{G}$ could be singular, hence a careful construction of $\boldsymbol{\phi}_d$ is

required to avoid singularity.

### 3.5.2 Stress

The stress modes can be derived from the Airy stress function, which is a common practice that has been used in prior research (see, e.g., Fu et al., 2010; Cen et al., 2011; Nodargi and Bisegna, 2017).

$$\boldsymbol{\sigma} = \begin{bmatrix} \sigma_x & \sigma_y & \tau_{xy} \end{bmatrix}^{\mathrm{T}} = \boldsymbol{\phi}_\sigma \boldsymbol{\alpha}, \tag{3.37}$$

with $\boldsymbol{\alpha} = \begin{bmatrix} \alpha_1 & \alpha_2 & \alpha_3 & \cdots & \alpha_{11} \end{bmatrix}^{\mathrm{T}}$ and $\boldsymbol{\phi}_\sigma$ can be explicitly shown as in Eq. (3.38),

$$\boldsymbol{\phi}_\sigma = \left[\begin{array}{ccc|cc|cc|cc|cc} 1 & 0 & 0 & 0 & y & 0 & x & 0 & 2xy & -x^2 & 2y^2 - x^2 \\ 0 & 1 & 0 & x & 0 & y & 0 & 2xy & 0 & 2x^2 - y^2 & -y^2 \\ 0 & 0 & 1 & 0 & 0 & -x & -y & -x^2 & -y^2 & 2xy & 2xy \end{array}\right]. \tag{3.38}$$

The chosen $\boldsymbol{\phi}_\sigma$ is complete up to order two. Compared to the one adopted by Fu et al. (2010), which can be referred to for a detailed derivation, the last two columns are however different — a symmetric pair is chosen here. Once the Jacobian matrix is known, $\boldsymbol{\sigma}$ can be conveniently expressed in terms of parent coordinates $\xi$ and $\eta$.

Some of the stress patterns that Eq. (3.38) can represent are illustrated in Fig. 3.3. The corresponding Airy stress terms are also shown in the same figure. For conventional FEM analyses, external loads are typically applied as (or converted to) concentrated nodal forces. This leads to a low-order distribution of stress field within the element domain. However, a constant or (incomplete) bilinear interpolation, as commonly adopted in existing elements, is not sufficient to properly describe stress distributions in certain loading cases. With a quadratic distribu-

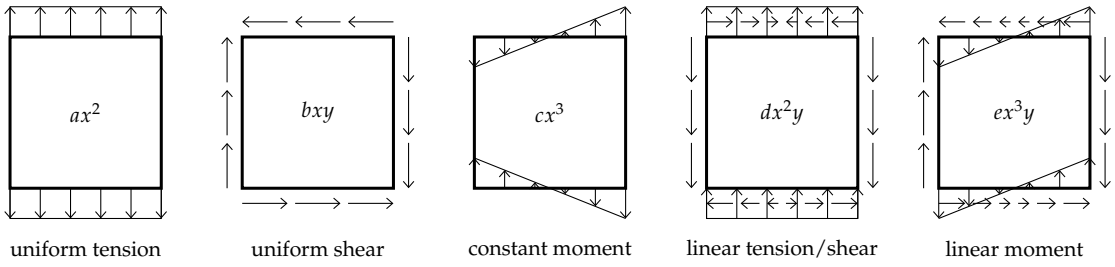


**FIGURE 3.3.** corresponding stress patterns of selected terms

tion, as can be seen in the figure, most stress patterns in loaded panel-like structures (without boundary tractions) can be covered.

### 3.5.3 Strain

The strain field is interpolated in a similar way,

$$\boldsymbol{\varepsilon} = \begin{bmatrix} \varepsilon_x & \varepsilon_y & \gamma_{xy} \end{bmatrix}^{\mathrm{T}} = \boldsymbol{\phi}_\varepsilon \boldsymbol{\beta} = \boldsymbol{C}\boldsymbol{\phi}_\sigma \boldsymbol{\beta}, \tag{3.39}$$

with $\boldsymbol{\beta} = \begin{bmatrix} \beta_1 & \beta_2 & \beta_3 & \cdots & \beta_{11} \end{bmatrix}^{\mathrm{T}}$. Mathematically, $\boldsymbol{C}$ is a constant matrix. In this sense, any constant matrices can be adopted, despite not all of them have physical meanings and perform well. For isotropic materials, $\boldsymbol{C}$ is chosen to be dependent on Poisson's ratio $\nu$,

$$\boldsymbol{C} = \begin{bmatrix} 1 & -\nu & 0 \\ -\nu & 1 & 0 \\ 0 & 0 & 2+2\nu \end{bmatrix}. \tag{3.40}$$

In such a manner, the Poisson effect can be correctly described. For the plane strain case, $\nu$ shall be replaced by $\nu/(1-\nu)$. In anisotropic cases, for example orthotropic models, $\boldsymbol{C}$ could be modified accordingly by introducing additional material constants.

The purpose of $\boldsymbol{C}$ is to bond interpolation parameters $\boldsymbol{\beta}$ to physical deformation. For example, the first three parameters ($\beta_1$, $\beta_2$ and $\beta_3$) now represent uniform tension along two global axes and the uniform shear deformation of the element. Practically the variability of Poisson's ratio is often ignored, hence a constant around 0.3 can be used for both elastic and elasto-plastic applications, if the element formulation has no access to material constants.

An identity matrix could be chosen as $\boldsymbol{C}$ for simplicity. In that case, only one of $\boldsymbol{\phi}_\varepsilon = \boldsymbol{\phi}_\sigma$ needs to be stored, although the resulting element is **no more insensitive** to volumetric locking. This can be predicted theoretically. Without $\boldsymbol{C}$, the interpolated strain field cannot describe an **isochoric** deformation for arbitrary interpolation parameters $\boldsymbol{\beta}$. For example, consider an incompressible plain strain case with $\nu = 0.5$, the left top $2 \times 2$ block of $\boldsymbol{C}$ becomes

$$\boldsymbol{C}_{2\times 2} = \begin{bmatrix} 1 & -1 \\ -1 & 1 \end{bmatrix}.$$

Let

$$\boldsymbol{\varepsilon}^* = \begin{bmatrix} \varepsilon_x^* & \varepsilon_y^* & \gamma_{xy}^* \end{bmatrix}^{\mathrm{T}} = \boldsymbol{\phi}_\sigma \boldsymbol{\beta} \tag{3.41}$$

be the strain before applying $\boldsymbol{C}$, so that $\boldsymbol{\varepsilon} = \boldsymbol{C}\boldsymbol{\varepsilon}^*$ contains the following normal strain components

$$\varepsilon_x = \varepsilon_x^* - \varepsilon_y^*, \qquad \varepsilon_y = \varepsilon_y^* - \varepsilon_x^*.$$

Obviously, the corresponding volumetric strain is zero for any $\boldsymbol{\beta}$. The presence of $\boldsymbol{C}$ allows the interpolated strain field to describe equivoluminal deformation. This explanation is consistent with the statement given by Belytschko et al. (2014, see pg. 500), who wrote: *to avoid locking, the strain field must be isochoric throughout the element for any velocity field which preserves the volume of the element*.

Alternatively, the strain and stress fields can also be interpolated in the parent coordinate system and then transformed back to the global frame in the corresponding integrals. Since the complete polynomials are chosen as the shape functions, $\boldsymbol{\phi}_\sigma$ and $\boldsymbol{\phi}_\varepsilon$ should be complete in both coordinate systems.

### 3.5.4 Enhanced Strain

Instead of the aforementioned full orthogonality condition, to pass the patch test, the enhanced strain $\hat{\boldsymbol{\varepsilon}}$ only needs to satisfy the following condition (Simo and Rifai, 1990; Taylor et al., 1976),

$$\int_V \langle \boldsymbol{\sigma}^*, \hat{\boldsymbol{\varepsilon}} \rangle \, \mathrm{d}V = \int_V \hat{\boldsymbol{\varepsilon}}^{\mathrm{T}} \boldsymbol{\sigma}^* \, \mathrm{d}V = \int_V \boldsymbol{\sigma}^{*,\mathrm{T}} \hat{\boldsymbol{\varepsilon}} \, \mathrm{d}V = 0,$$

where $\boldsymbol{\sigma}^*$ denotes a **constant** stress field that is frame invariant. Noting that $\boldsymbol{\zeta}$ should be arbitrary and $\hat{\boldsymbol{\varepsilon}}$ needs to be transformed into the global reference frame when evaluating the integral, it is equivalent to express the above condition as

$$\int_V \boldsymbol{\phi}_{\hat{\varepsilon}}^g \, \mathrm{d}V = \mathbf{0}, \tag{3.42}$$

where $\boldsymbol{\phi}^g_{\hat{\varepsilon}}$ denotes the corresponding global interpolation function so that $\hat{\boldsymbol{\varepsilon}}^g = \boldsymbol{\phi}^g_{\hat{\varepsilon}}\boldsymbol{\zeta}$. Noting that by default $\boldsymbol{\phi}_{\hat{\varepsilon}}$ denotes the interpolation in the parent coordinate system. The required $\boldsymbol{\phi}^g_{\hat{\varepsilon}}$ can be obtained by the following transformation

$$\boldsymbol{\phi}^g_{\hat{\varepsilon}} = \boldsymbol{F}_0\boldsymbol{\phi}_{\hat{\varepsilon}}, \tag{3.43}$$

where $\boldsymbol{F}_0$ is the transformation matrix that depends on the corresponding Jacobian $\boldsymbol{J}_0$ evaluated at $\xi = \eta = 0$.

Let $\boldsymbol{J}_0$ be denoted as

$$\boldsymbol{J}_0 = \begin{bmatrix} \dfrac{\partial x}{\partial \xi} & \dfrac{\partial y}{\partial \xi} \\ \dfrac{\partial x}{\partial \eta} & \dfrac{\partial y}{\partial \eta} \end{bmatrix} = \begin{bmatrix} J_{11} & J_{12} \\ J_{21} & J_{22} \end{bmatrix},$$

then $\boldsymbol{F}_0$ can be expressed as

$$\boldsymbol{F}_0 = \begin{bmatrix} J_{11}^2 & J_{21}^2 & 2J_{11}J_{21} \\ J_{12}^2 & J_{22}^2 & 2J_{12}J_{22} \\ J_{11}J_{12} & J_{21}J_{22} & J_{11}J_{22} + J_{12}J_{21} \end{bmatrix}. \tag{3.44}$$

Since $\boldsymbol{F}_0$ is constant, Eq. (3.42) becomes

$$\int_V \boldsymbol{\phi}_{\hat{\varepsilon}}\, \mathrm{d}V = \boldsymbol{0}. \tag{3.45}$$

For the final stiffness matrix to be non-singular, the following condition should be met,

$$n_\sigma \geqslant n_u + n_{\hat{\varepsilon}} - n_r, \tag{3.46}$$

in which $n_\sigma$, $n_u$, $n_{\hat{\varepsilon}}$ are the numbers of modes of corresponding fields and $n_r$ is the number of rigid body modes. In this work, $n_\sigma = 11$, $n_u = 8 + 4 = 12$ and $n_r = 4$ (instead of 3 due to that the rotation field is assumed to be an independent field), this leads to $n_{\hat{\varepsilon}} \leqslant 3$.

The complete cubic polynomials $\boldsymbol{\phi}$ include ten terms

$$\boldsymbol{\phi} = \begin{bmatrix} 1 & \xi & \eta & \xi\eta & \xi^2 & \eta^2 & \xi^3 & \xi^2\eta & \xi\eta^2 & \eta^3 \end{bmatrix}. \tag{3.47}$$

The integral of which gives

$$\int_S \boldsymbol{\phi}\, \mathrm{d}S = \int_{-1}^{1}\int_{-1}^{1} \boldsymbol{\phi}\, \mathrm{d}\xi\mathrm{d}\eta = \begin{bmatrix} 4 & 0 & 0 & 0 & \frac{4}{3} & \frac{4}{3} & 0 & 0 & 0 & 0 \end{bmatrix}. \tag{3.48}$$

This indicates that terms $\xi$, $\eta$, $\xi\eta$, $\xi^3$, $\eta^3$, $\xi^2\eta$ and $\xi\eta^2$ can be freely combined as (part of) the enhanced strain modes. For the remaining terms, following combinations are admissible: $3\xi^2 - 1$, $3\eta^2 - 1$ and $\xi^2 - \eta^2$. By replacing the original terms with the admissible ones, one can obtain

$$\boldsymbol{\phi} = \begin{bmatrix} \xi & \eta & \xi\eta & 3\xi^2 - 1 & 3\eta^2 - 1 & \xi^2 - \eta^2 & \xi^3 & \xi^2\eta & \xi\eta^2 & \eta^3 \end{bmatrix}. \tag{3.49}$$

For the purpose of satisfying Eq. (3.45) **only**, the linear combinations of any terms in Eq. (3.49) can be used as the enhanced strain mode. This allows various modes to be created and used, although **not all possible combinations work and the performance may vary**.

After extensive numerical experiments, the following modes are chosen. It shall be noted that $\boldsymbol{\phi}_{\hat{\varepsilon}}$ could have at most three columns. Here only one example is shown for brevity.

$$\boldsymbol{\phi}_{\hat{\varepsilon}} = \begin{bmatrix} 3\xi^2 - 1 \\ 3\eta^2 - 1 \\ 0 \end{bmatrix}. \tag{3.50}$$

## 3.6 INTEGRATION SCHEME

To integrate a cubic function, theoretically a two-point Gaussian quadrature is sufficient. However, for the proposed GCMQ element, a $2 \times 2$ scheme can only provide six constraints while the total number of DoFs is twelve with four rigid body modes*. To avoid additional treatments (e.g., isolation and suppression of zero energy modes), the number of integration points shall increase. The simplest solution is to use the $3 \times 3$ Gaussian or Lobatto quadratures.

In fact, to provide two more constraints, only one additional integration point is required. Hence it would be appealing if a five-point scheme (instead of a nine-point scheme) can be applied as in that case, the computation cost could be roughly halved.

Irons (1971) proposed a class of quadrature rules for 3D applications, the six-point version

*The additional one rigid body mode is caused by the independent rotation field.

has a cubic accuracy and can be expressed as

$$\int F(\xi,\eta,\psi)\,\mathrm{d}V = \sum_{i=1}^{6} w_i F_i = wF(\pm 1,0,0) + wF(0,\pm 1,0) + wF(0,0,\pm 1)\,, \tag{3.51}$$

with $w = 4/3$. It is possible to project the cube onto $\xi\eta$ plane by compressing the third axis $\psi$. Then Eq. (3.51) becomes

$$\int F(\xi,\eta)\,\mathrm{d}A = \sum_{i=1}^{5} w_i F_i = wF(\pm 1,0) + wF(0,\pm 1) + 2wF(0,0) \tag{3.52}$$

with a halved weight $w = 2/3$. Since Eq. (3.51) has a cubic accuracy (Irons, 1971), Eq. (3.52) should also possess an equivalent truncation error of $\mathcal{O}(h^4)$.

Three versions that use different integration schemes are provided with GCMQ, which are GCMQI(rons), GCMQL(obatto) and GCMQG(auss). As can be seen in the next chapter, no significant difference is observed among three schemes with dense mesh configurations. But different results could be given with very coarse mesh grids.

## 3.7 MASS MATRIX

Either consistent or lumped mass matrices can be used in analyses. The standard concentration methods can be applied. According to the finite element formulation, the mass matrix can be computed based on the integration of displacement shape functions. Such a formulation is known as the consistent (to displacement) mass matrix. In GCMQ, using the previous notations, it can be expressed as

$$\boldsymbol{M} = \int_V \boldsymbol{\phi}_u^{\mathrm{T}} \rho \boldsymbol{\phi}_u \mathrm{d}V. \tag{3.53}$$

Noting that the symbols used here have different meanings, here $\boldsymbol{M}$ is the element mass matrix. It shall be stressed that all three integration schemes only **under-integrate** the mass matrix, which has terms up to sixth order, as $\boldsymbol{N} = \boldsymbol{\phi}_u$ contains cubic order terms. This may not be a major problem as in most cases the lumped mass is used.

It is known that omitting rotational inertia has little impact on the accuracy of computed lower mode frequencies for normal finite element meshes. By setting the four drilling diagonal terms to zeros, Eq. (3.53) becomes the consistent mass matrix of the bilinear quadrilateral ele-

ment (Q4) with additional zero fill-ins. It shall be noted that such a reduced mass matrix and its lumped companion are only positive semi-definite.

Apart from the above two consistent formulations, the corresponding lumped versions can also be adopted to save storage. There are a few different lumping approaches. The diagonal scaling approach is one of them and it uses the following expression.

$$\bar{\boldsymbol{M}}_{ij} = \begin{cases} \alpha \boldsymbol{M}_{ij}, & i = j, \\ 0, & i \neq j, \end{cases} \tag{3.54}$$

where $\bar{\boldsymbol{M}}$ is the lumped version of the consistent mass matrix $\boldsymbol{M}$ and $\alpha$ is the scaling factor and shall be properly determined so that the total mass along each direction equals the mass of the element. An illustration of entry patterns of different mass formulations can be seen in Fig. 3.4. It would be preferable to have a positive definite (non-singular) mass matrix so that

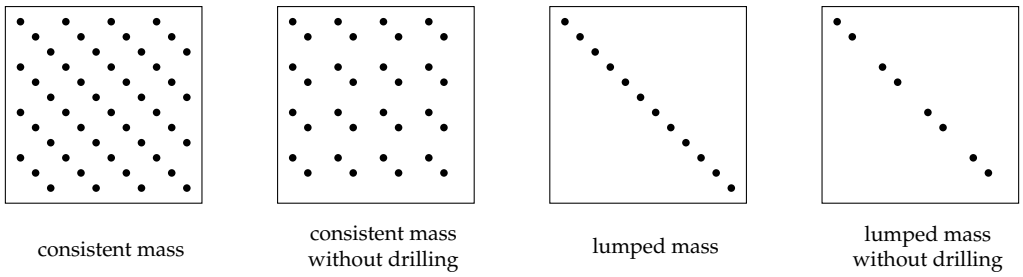


FIGURE 3.4. entry patterns of different mass matrices

the frequencies of the corresponding model are well bounded. A singular mass matrix may not be an issue for dynamic applications in structural engineering which are mostly subjected to low frequency excitations, however, it would make a significant impact on wave propagation applications where high frequency response matters. This may also affect the stability of some time integration methods such as the central difference method, in which the global mass matrix shall be full ranked in the absence of damping matrix. Standard dynamics textbooks (e.g., Chopra, 2011) are referred to here for more details.

## 3.8 COST ESTIMATION

To estimate the computational cost, here the number of multiplications is counted for each operation. There are various algorithms in existing literature to compute the product of matrices. For two $n \times n$ matrices, the lower bound of arithmetic operations is commonly known

to be $O(n^3)$. The currently known best upper bound is $O(n^{2.3728639})$. For a rough estimation, here the lower bound is used so that for the product of two matrices of sizes $i \times j$ and $j \times k$ respectively, the number of scalar multiplications required is simply $i \times j \times k$.

For both five-point and nine-point integration schemes, the required numbers of arithmetic multiplications for various numbers of enhanced strain modes are shown in Table 3.1. The efficiency of a single GCMQ element is comparable to that of Q8 (second order serendipity quadrilateral element, CPS8 in ABAQUS notation), in particular, GCMQ is slower than Q8R with reduced integration but faster than Q8 with full $3 \times 3$ integration scheme. Given that GCMQ has a smaller number of DoFs, the corresponding global matrix has a smaller size which leads to a faster solving process. It could be concluded that GCMQ is more efficient than Q8 in terms of overall performance.

**TABLE 3.1.** multiplication operation counter

| operation | 1 enhanced mode | 2 enhanced modes | 3 enhanced modes |
|---|---|---|---|
| $\Delta\boldsymbol{\zeta} = -[\boldsymbol{VIF}]_n - [\boldsymbol{VIWT}]_n \Delta\boldsymbol{q}$ | $1 \times 12 \times 1$ | $2 \times 12 \times 1$ | $3 \times 12 \times 1$ |
| $\Delta\boldsymbol{\beta} = \tilde{\boldsymbol{N}}\Delta\boldsymbol{q} + \tilde{\boldsymbol{M}}\Delta\boldsymbol{\zeta}$ | $11 \times 12 \times 1 + 11 \times 1 \times 1$ | $11 \times 12 \times 1 + 11 \times 2 \times 1$ | $11 \times 12 \times 1 + 11 \times 3 \times 1$ |
| $\boldsymbol{\varepsilon}^i_{n+1} = \boldsymbol{\phi}^i_\varepsilon \boldsymbol{\beta}_{n+1}$ | $3 \times 11 \times 1$ | | |
| $\tilde{\boldsymbol{H}}_{n+1} = \sum w^i \boldsymbol{\phi}^{i,\mathrm{T}}_\varepsilon \tilde{\boldsymbol{E}}^i_{n+1} \boldsymbol{\phi}^i_\varepsilon$ | $11 \times 3 \times 11 + 3 \times 3 \times 11$ | | |
| $\tilde{\boldsymbol{S}}_{n+1} = \sum w^i \boldsymbol{\phi}^{i,\mathrm{T}}_\varepsilon \tilde{\boldsymbol{\sigma}}^i_{n+1}$ | $11 \times 3 \times 1$ | | |
| $\boldsymbol{\alpha}_{n+1} = \boldsymbol{H}^{-\mathrm{T}} \tilde{\boldsymbol{S}}_{n+1}$ | $11 \times 11 \times 1$ | | |
| $\boldsymbol{V}_{n+1} = \tilde{\boldsymbol{M}}^{\mathrm{T}} \tilde{\boldsymbol{H}} \tilde{\boldsymbol{M}}$ | $1 \times 11 \times 11 + 11 \times 11 \times 1$ | $2 \times 11 \times 11 + 11 \times 11 \times 2$ | $3 \times 11 \times 11 + 11 \times 11 \times 3$ |
| $\boldsymbol{T}_{n+1} = \tilde{\boldsymbol{N}}^{\mathrm{T}} \tilde{\boldsymbol{H}}$ | $12 \times 11 \times 11$ | | |
| $\boldsymbol{W}_{n+1} = \boldsymbol{T}_{n+1} \tilde{\boldsymbol{M}}$ | $12 \times 11 \times 1$ | $12 \times 11 \times 2$ | $12 \times 11 \times 3$ |
| $[\boldsymbol{VIWT}]_{n+1} = \boldsymbol{V}^{-1}_{n+1} \boldsymbol{W}^{\mathrm{T}}_{n+1}$ | $1 \times 1 \times 12$ | $2 \times 2 \times 12$ | $3 \times 3 \times 12$ |
| $[\boldsymbol{VIF}]_{n+1} = \boldsymbol{V}^{-1}_{n+1} \boldsymbol{M}^{\mathrm{T}} \boldsymbol{\alpha}_{n+1}$ | $1 \times 1 \times 1 + 1 \times 11 \times 1$ | $2 \times 2 \times 1 + 2 \times 11 \times 1$ | $3 \times 3 \times 1 + 3 \times 11 \times 1$ |
| $\boldsymbol{K} = \boldsymbol{T}_{n+1} (\tilde{\boldsymbol{N}} - \tilde{\boldsymbol{M}} [\boldsymbol{VIWT}]_{n+1})$ | $12 \times 11 \times 12 + 11 \times 1 \times 12$ | $12 \times 11 \times 12 + 11 \times 2 \times 12$ | $12 \times 11 \times 12 + 11 \times 3 \times 12$ |
| $\boldsymbol{R} = \boldsymbol{N}\boldsymbol{\alpha}_{n+1} - \boldsymbol{W}_{n+1} [\boldsymbol{VIF}]_{n+1}$ | $12 \times 11 \times 1 + 12 \times 1 \times 1$ | $12 \times 11 \times 1 + 12 \times 2 \times 1$ | $12 \times 11 \times 1 + 12 \times 3 \times 1$ |
| five-point summation | 6626 | 7217 | 7824 |
| nine-point summation | 8738 | 9329 | 9946 |

## 3.9 SECTION RESULTANT FORCES

Engineers are more interested in section resultant forces as from which useful information can be extracted to guide structure design. By definition, section resultant forces, including moment $M$, axial force $F$ and shear force $V$, can be obtained by integrating the stress field $\sigma$ over the target section, which degenerates to a line in a 2D scenario. Since the proposed GCMQ element explicitly interpolates the stress field, the corresponding integration is possible.

For any section within the element domain, three resultant forces could be expressed as

$$F = \int \sigma_w \, \mathrm{d}A, \qquad V = \int \tau_s \, \mathrm{d}A, \qquad M = \int s \cdot \sigma_w \, \mathrm{d}A, \tag{3.55}$$

in which $s$ and $w$ are local coordinates of the target section/line, $\sigma_w$ and $\tau_s$ are two stresses acting along corresponding directions. The $w$ axis points to the outer normal direction while the $s$ axis coincides with the section inclination. Since a uniform thickness $t$ is assumed, $\mathrm{d}A$ simply equals to $t \cdot \mathrm{d}s$.

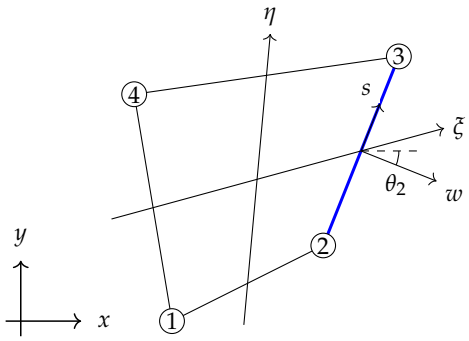


**FIGURE 3.5.** definitions of reference frames

Here only the edge 2 that connects node 2 and 3 is discussed for illustration. Fig. 3.5 shows the definitions of three different reference frames: the global coordinate system $x$-$y$, the parent coordinate system $\xi$-$\eta$ and the local coordinate system $s$-$w$ for edge 2. In this case, $s$ and $\eta$ are of the same direction so that

$$\mathrm{d}s = \frac{e_2}{2}\mathrm{d}\eta,$$

where $e_2$ is the length of edge 2. The stress $\boldsymbol{\sigma}$ can be transformed from $x$-$y$ system to $w$-$s$ system as follows,

$$\bar{\boldsymbol{\sigma}}_2(\eta) = \begin{bmatrix} \sigma_w \\ \tau_s \end{bmatrix} = \boldsymbol{L}_2 \boldsymbol{\sigma}_2 = \boldsymbol{L}_2 \boldsymbol{\phi}_\sigma(\xi, \eta)\Big|_{\xi=1} \boldsymbol{\alpha}, \tag{3.56}$$

with

$$\boldsymbol{L}_2 = \begin{bmatrix} l_2^2 & m_2^2 & 2l_2m_2 \\ -l_2m_2 & l_2m_2 & l_2^2 - m_2^2 \end{bmatrix}, \tag{3.57}$$

where $l_2 = \cos\theta_2$ and $m_2 = \sin\theta_2$ are directional cosines with $\theta_2$ denotes the anticlockwise angle measured from $x$-axis to $w$-axis. The subscript $n = 1, 2, 3, 4$ denotes four edge labels. The transformation matrix $\boldsymbol{L}_n$ can be easily derived from the free body diagram of a wedge subjected to given stress status $\boldsymbol{\sigma}$. It shall be stressed that the original $\boldsymbol{\phi}_\sigma$ is a function of global coordinates $x$ and $y$, while in Eq. (3.56) it is expressed as a function of the parent coordinates $\xi$ and $\eta$. The transformation between parent and global coordinates is given by the Jacobian matrix that is available via isoparametric mapping.

Then three section resultant forces can be simply integrated as

$$
\begin{aligned}
F_2 &= \int \sigma_w \, \mathrm{d}A = \frac{e_2 t}{2} \int_{-1}^{1} \sigma_w \, \mathrm{d}\eta, \\
V_2 &= \int \tau_s \, \mathrm{d}A = \frac{e_2 t}{2} \int_{-1}^{1} \tau_s \, \mathrm{d}\eta, \\
M_2 &= \int s \cdot \sigma_w \, \mathrm{d}A = \frac{e_2^2 t}{4} \int_{-1}^{1} \eta \cdot \sigma_w \, \mathrm{d}\eta.
\end{aligned}
$$

Since $\boldsymbol{L}_n$ is a constant matrix for each boundary, they can further be expressed as

$$
\begin{bmatrix} F_2 \\ V_2 \end{bmatrix} = \frac{e_2 t}{2} \boldsymbol{L}_2 \boldsymbol{C}_2 \boldsymbol{\alpha}, \qquad M_2 = \frac{e_2^2 t}{4} \boldsymbol{L}_2^{(1)} \boldsymbol{D}_2 \boldsymbol{\alpha}. \tag{3.58}
$$

where

$$
\boldsymbol{C}_2 = \int_{-1}^{1} \boldsymbol{\phi}_\sigma \left(\xi, \eta\right) \Big|_{\xi=1} \mathrm{d}\eta, \qquad \boldsymbol{D}_2 = \int_{-1}^{1} \eta \cdot \boldsymbol{\phi}_\sigma \left(\xi, \eta\right) \Big|_{\xi=1} \mathrm{d}\eta. \tag{3.59}
$$

The symbol $\boldsymbol{L}_2^{(1)}$ denotes the first row of $\boldsymbol{L}_2$. The matrices $\boldsymbol{C}_2$ and $\boldsymbol{D}_2$, that contain up to cubic terms, can be precisely evaluated by a two-point Gaussian scheme. For other edges, the transformation can be derived in a similar fashion. A closed form of above resultant forces is available only if the shape of element is a parallelogram or rectangle.

It shall be emphasised that since the resultant moment is computed per edge, it is less meaningful when several elements are defined side by side, in which case, further post-processing is required in order to obtain a section resultant moment. It is useful when there is only one element defined along the width of the wall. The resultant axial and shear forces are sectional equivalences of the corresponding stress components. Since the interpolated stress field satisfies equilibrium, the resultant forces obtained in this way also satisfy force equilibrium.

## 3.10 A SIMPLIFICATION OF GCMQ

For seismic engineering related applications with complex materials, such as reinforced concrete, the additional improvement of performance (around a few percent) brought by the enhanced strain field $\hat{\boldsymbol{\varepsilon}}$ is disproportional to its cost. Meanwhile, the overall numerical performance also largely depends on the material models used. A cost efficient element is thus of more interest. To this end, the original functional Eq. (3.11) can be further simplified by omitting the enhanced strain field, which results in the following governing functional.

$$\Pi_F(\boldsymbol{u}, \boldsymbol{\varepsilon}, \boldsymbol{\sigma}) = \int_V \left[ W(\boldsymbol{\varepsilon}) + \boldsymbol{\sigma}^{\mathrm{T}} (\nabla \boldsymbol{u} - \boldsymbol{\varepsilon}) \right] \mathrm{d}V - \Pi_{bt}(\boldsymbol{u}). \tag{3.60}$$

Eq. (3.60) is identical to the Hu-Washizu variational principle, although $\boldsymbol{u}$ now consists of the contributions of both translational and drilling degrees of freedom.

Based on the above simplification, a new element, denoted as SGCMQ (Simplified GCMQ), can be derived. The derivation resembles the original one for GCMQ. Here a brief summary is presented solely for completeness. By taking variations of Eq. (3.60) and linearising the result using the following discretisations,

$$\boldsymbol{u} = \boldsymbol{\phi}_u \boldsymbol{q}, \quad \boldsymbol{\sigma} = \boldsymbol{\phi}_\sigma \boldsymbol{\alpha}, \quad \boldsymbol{\varepsilon} = \boldsymbol{\phi}_\varepsilon \boldsymbol{\beta},$$

where $\boldsymbol{q}$, $\boldsymbol{\alpha}$ and $\boldsymbol{\beta}$ are interpolation parameters for displacement, stress and strain, respectively. Meanwhile, $\boldsymbol{\phi}_u$, $\boldsymbol{\phi}_\sigma$ and $\boldsymbol{\phi}_\varepsilon$ are the corresponding interpolation functions that are chosen to be identical to that of GCMQ.

The system of linear equations can be expressed as

$$\begin{bmatrix} \cdot & \boldsymbol{N}^{\mathrm{T}} & \cdot \\ \boldsymbol{N} & \cdot & -\boldsymbol{H} \\ \cdot & -\boldsymbol{H}^{\mathrm{T}} & \tilde{\boldsymbol{H}} \end{bmatrix} \begin{bmatrix} \Delta \boldsymbol{q} \\ \Delta \boldsymbol{\alpha} \\ \Delta \boldsymbol{\beta} \end{bmatrix} = \begin{bmatrix} \boldsymbol{P}_{n+1} - \boldsymbol{P}_n \\ \boldsymbol{0} \\ \boldsymbol{0} \end{bmatrix}, \tag{3.61}$$

with

$$\boldsymbol{H} = \int_V \boldsymbol{\phi}_\sigma^{\mathrm{T}} \boldsymbol{\phi}_\varepsilon \mathrm{d}V, \quad \tilde{\boldsymbol{H}} = \int_V \boldsymbol{\phi}_\varepsilon^{\mathrm{T}} \tilde{\boldsymbol{E}} \boldsymbol{\phi}_\varepsilon \mathrm{d}V, \quad \boldsymbol{N} = \int_V \boldsymbol{\phi}_\sigma^{\mathrm{T}} \boldsymbol{L} \boldsymbol{\phi}_u \mathrm{d}V, \tag{3.62}$$

in which $\tilde{\boldsymbol{E}}$ is the material tangent stiffness and $\boldsymbol{L}$ is the gradient operator.

With an invertible $\boldsymbol{H}$, the equivalent stiffness $\boldsymbol{K}$ can be simply expressed as

$$\boldsymbol{K} = \boldsymbol{N}^{\mathrm{T}}\boldsymbol{H}^{-\mathrm{T}}\tilde{\boldsymbol{H}}\boldsymbol{H}^{-\mathbf{1}}\boldsymbol{N}.$$

By further denoting $\bar{\boldsymbol{N}} = \boldsymbol{\phi}_{\varepsilon}\boldsymbol{H}^{-1}\boldsymbol{N}$, one can obtain

$$\boldsymbol{K} = \int_{V} \bar{\boldsymbol{N}}^{\mathrm{T}}\tilde{\boldsymbol{E}}\bar{\boldsymbol{N}}\mathrm{d}V. \tag{3.63}$$

Eq. (3.63) has a form similar to that of traditional displacement based elements. As a result, no element level matrix operations are required. The numerical cost of such a simplified element is only about 2 to 3 times of that of Q4. Meanwhile, with a form of Eq. (3.63), it is possible to formulate planar shell elements by combining other high performing plate elements into the formulation in a relatively independent manner.

# 4

# Analytical Validations of GCMQ

The analytical validations and performance benchmarks of GCMQ are the main focuses of this chapter. Isotropic linear elastic materials are used in all examples presented in this chapter. Certain assumptions are made to properly simulate the correct boundary conditions. For most examples, analytical solutions obtained in accordance with the theory of elasticity are also given. For the problems with no analytical solutions, mesh refinements are performed to obtain converged values which are used as reference solutions.

Part of this chapter is published in the journal paper *A New Drilling Quadrilateral Membrane Element With High Coarse-Mesh Accuracy Using A Modified Hu-Washizu Principle* (Chang et al., 2019a) with **International Journal for Numerical Methods in Engineering**.

## 4.1 Eigenanalysis

Before presenting benchmarks, the eigenanalysis is performed to reveal zero energy modes and deformation patterns, which are shown in Fig. 4.1. A unit square GCMQI element is used to formulate the stiffness matrix. The other integration schemes may give slightly different values.

The first four modes are zero energy modes with trivial eigenvalues, which correspond to two translations, one rigid rotation and one additional pure distortion mode due to the presence of drilling degrees of freedom. Modes 5, 6 and 7 are combined modes that are mainly

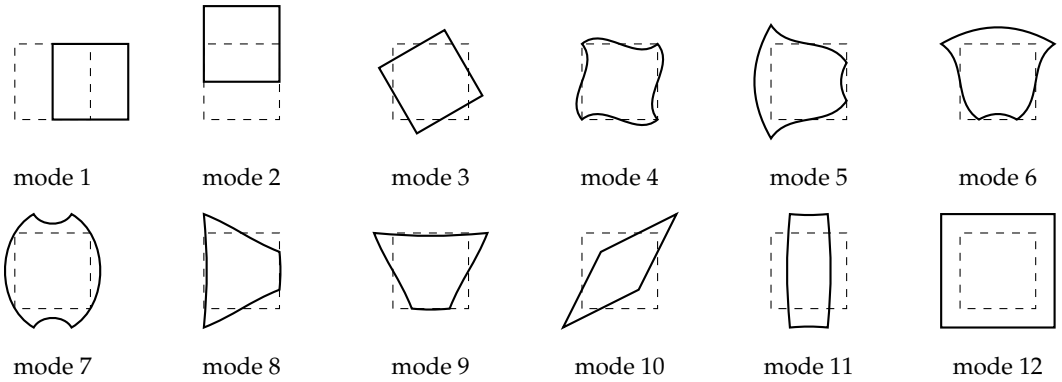


**FIGURE 4.1.** eigenmodes of the proposed GCMQ element

governed by distortion (rotation). Modes 8, 9 and 11 are the counterparts that are dominated by translation. The remaining two are one pure shear (mode 10) and one dilatation (mode 12). The coupling between translation and drilling DoFs can be isolated by applying recombinations of eigenvectors. It shall be stressed that the recombined modes 5, 6, 7, 8, 9 and 11 shown in Fig. 4.2 are not eigenvectors.

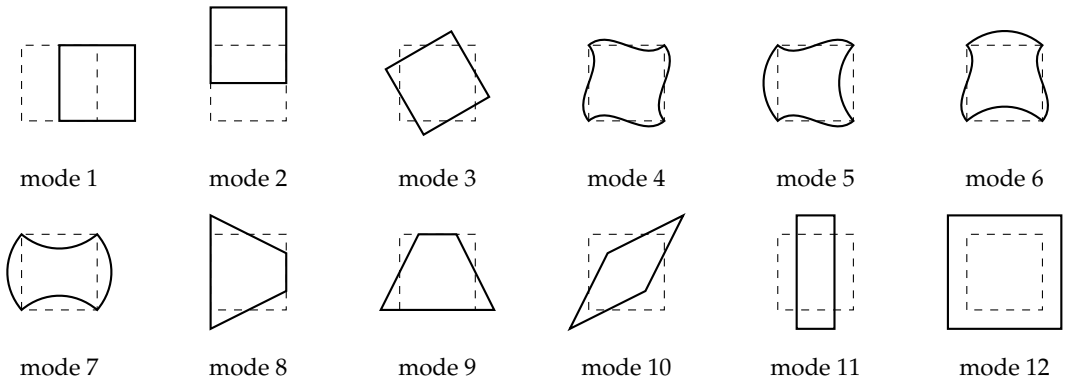


**FIGURE 4.2.** recombined basic deformation modes

## 4.2 THE PATCH TEST

### Patch Test I

As a convention adopted widely in finite element development, the patch test (Irons, 1966) is first presented as an elementary example. The model defines four elements in a rectangular panel as shown in Fig. 4.3.

Given that the drilling part $\boldsymbol{u}_d$ is interpolated with a higher order function, to generate a constant strain field, the corresponding DoF has to be trivial, that is $\boldsymbol{\theta} = \mathbf{0}$. Once $\boldsymbol{u}_d$ is suppressed,

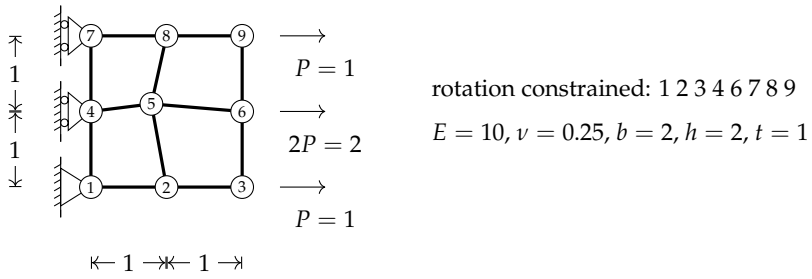


**FIGURE 4.3.** constant strain patch test a

the only displacement component left is $\boldsymbol{u}_t$ which is identical to the conforming displacement field in Q4. For convex mesh grids, linear displacement field and constant strain/stress field can be successfully recovered by all three versions of GCMQ. The Irons and Lobatto schemes do have numerical stability issues with concave geometries as some integration points are located on element boundaries, while the Gauss scheme has no such problems.

### Patch Test II

FE model shown in Fig. 4.4 gives identical result $u_4 = u_{14} = 0.6$ to the analytical one. Meanwhile, altering the position of any edge and/or internal node does not affect the result. Other forms of constant strain patch test (see, e.g., MacNeal and Harder, 1985) also give exact analytical solutions. Hence it can be concluded that GCMQ can pass the patch test.

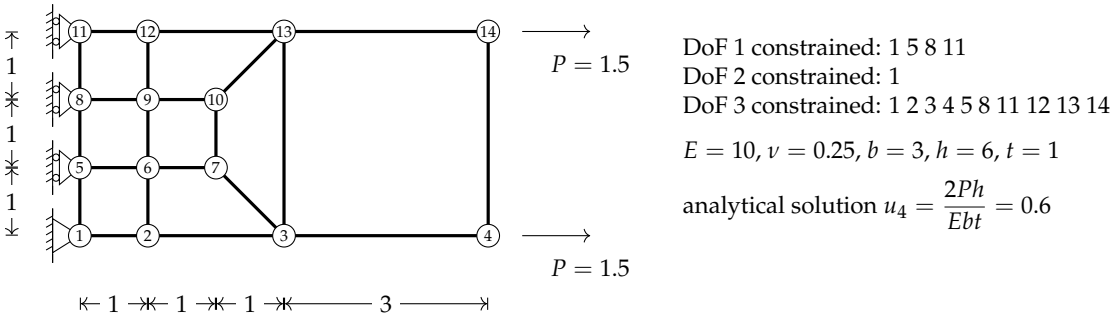


**FIGURE 4.4.** constant strain patch test b

## 4.3 CONVERGENCE

### 4.3.1 Curved Beam

Convergence can be illustrated by mesh refinements with examples that can be solved analytically. Fig. 4.5 shows a curved beam subjected to end force. The deflection of the free end is

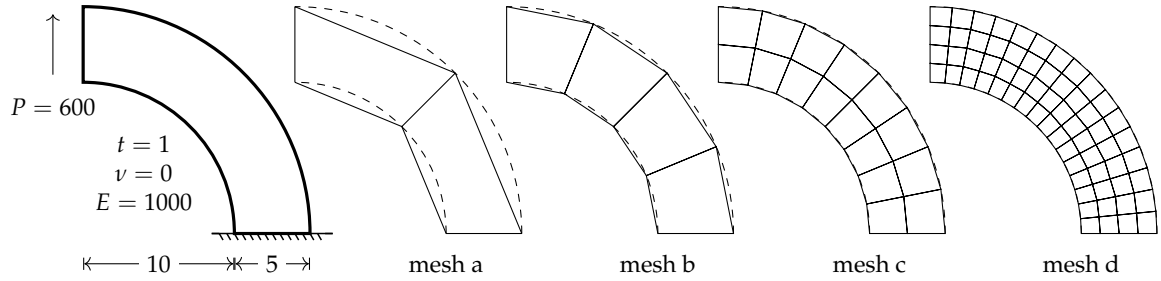


**FIGURE 4.5.** curved beam subjected to tip load

given analytically by

$$v = \frac{P\pi}{E} \cdot \frac{a^2 + b^2}{(a^2 - b^2) + (a^2 + b^2)\ln\frac{b}{a}}. \tag{4.1}$$

The derivation can be seen elsewhere (Timoshenko, 1970). For the geometry and material properties shown in Fig. 4.5, where $a = 10$ and $b = 15$,

$$v = \frac{600}{1000} \cdot \frac{10^2 + 15^2}{(10^2 - 15^2) + (10^2 + 15^2)\ln 1.5} \cdot \pi \approx 90.41. \tag{4.2}$$

It shall be noted that the above analytical solution is obtained by applying traction boundary condition $\int \tau \, \mathrm{d}A = P$ on the free end, the actual distribution of $\tau$ is unknown. In the following numerical examples, a uniformly distributed shear force is assumed.

**TABLE 4.1.** averaged tip deflection and error of a curved beam

| | mesh a | | mesh b | | mesh c | | mesh d | |
|---|---|---|---|---|---|---|---|---|
| element | $v$ | % | $v$ | % | $v$ | % | $v$ | % |
| Q4 | 22.36 | 75.27 | 57.90 | 35.96 | 79.29 | 12.30 | 87.26 | 3.49 |
| PS | 51.16 | 43.42 | 84.52 | 6.52 | 88.41 | 2.20 | 89.79 | 0.68 |
| QE2 | 51.32 | 43.23 | 84.53 | 6.50 | 88.41 | 2.20 | 89.79 | 0.68 |
| GQ12 | 83.70 | 7.42 | 89.07 | 1.48 | 89.81 | 0.66 | 90.20 | 0.23 |
| US-ATFQ4 | - | - | 86.30 | 4.54 | - | - | - | - |
| AGQ-I | - | - | 91.88 | -1.63 | - | - | - | - |
| AGQ-II | - | - | 86.93 | 3.85 | - | - | - | - |
| GCMQI | 85.31 | 5.64 | 87.17 | 3.58 | 89.88 | 0.58 | 90.26 | 0.16 |
| GCMQL | 85.52 | 5.40 | 88.74 | 1.84 | 89.94 | 0.51 | 90.26 | 0.16 |
| GCMQG | 86.72 | 4.08 | 89.83 | 0.64 | 90.05 | 0.39 | 90.27 | 0.15 |
| SGCMQI | 85.30 | 5.65 | 87.16 | 3.59 | 89.88 | 0.59 | 90.26 | 0.17 |
| SGCMQL | 83.68 | 7.44 | 86.85 | 3.94 | 89.85 | 0.62 | 90.26 | 0.17 |
| SGCMQG | 84.46 | 6.58 | 88.23 | 2.41 | 89.97 | 0.49 | 90.27 | 0.15 |
| ref. | 90.41 | | | | | | | |

Numerical results and comparisons with other elements are presented in Table 4.1. For the not-even-close-to-geometry mesh grid with only two elements defined, the error is around 5 % which is acceptable. This indicates GCMQ has a relatively good performance under coarse

mesh configurations.

### 4.3.2 Cook's Skew Beam

The skew beam (Cook, 1987) shown in Fig. 4.6 is a popular example used to evaluate the overall performance of new elements.

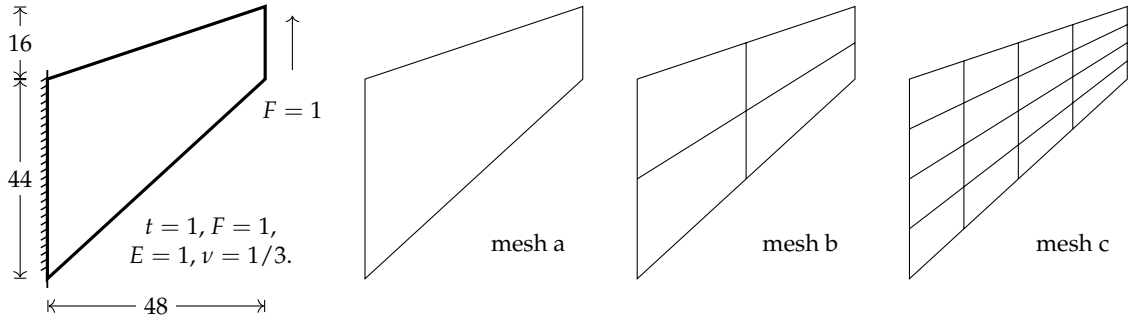


**FIGURE 4.6.** Cook's skew beam

**TABLE 4.2.** averaged tip deflection and error of Cook's skew beam

| | mesh a | | mesh b | | mesh c | |
|---|---|---|---|---|---|---|
| | $v$ | error % | $v$ | error % | $v$ | error % |
| Q4 | 5.97 | 75.1 | 11.85 | 50.5 | 18.30 | 23.6 |
| Q8 | 17.14 | 28.5 | 22.72 | 5.2 | 23.71 | 1.0 |
| PS | 16.73 | 30.2 | 21.13 | 11.8 | 23.02 | 3.9 |
| GQ12 | 16.25 | 32.2 | 20.89 | 12.8 | 23.06 | 3.8 |
| GQ12M | 20.31 | 15.2 | 21.69 | 9.5 | 23.30 | 2.8 |
| QE2 | 19.13 | 20.2 | 21.35 | 10.9 | 23.04 | 3.8 |
| D-Type | 14.07 | 41.3 | 20.68 | 13.7 | 22.98 | 4.1 |
| HSFQ4 | 21.01 | 12.1 | 22.55 | 5.9 | 23.44 | 2.2 |
| Pimpinelli (2004) | 15.95 | 33.4 | 21.02 | 12.3 | 23.01 | 4.0 |
| Choi et al. (2006) | - | - | 22.55 | 5.9 | 23.44 | 2.2 |
| Madeo et al. (2012) | - | - | 22.14 | 7.6 | 23.42 | 2.3 |
| Boutagouga (2016) | - | - | 22.09 | 7.8 | 23.30 | 2.8 |
| Zouari et al. (2016) | - | - | 21.37 | 10.8 | 23.06 | 3.8 |
| US-ATFQ4 | - | - | 22.76 | 5.0 | 23.43 | 2.2 |
| GCMQI | 19.94 | 16.8 | 22.03 | 8.0 | 23.41 | 2.3 |
| GCMQL | 19.21 | 19.8 | 22.03 | 8.0 | 23.43 | 2.2 |
| GCMQG | 19.19 | 19.9 | 22.41 | 6.5 | 23.52 | 1.8 |
| SGCMQI | 19.71 | 17.7 | 21.93 | 8.5 | 23.39 | 2.4 |
| SGCMQL | 17.89 | 25.3 | 21.89 | 8.7 | 23.41 | 2.3 |
| SGCMQG | 18.00 | 24.9 | 22.30 | 6.9 | 23.51 | 1.9 |
| ref. | 23.96 | | | | | |

Numerical results are shown in Table 4.2. Similar to the previous curved beam, GCMQ shows a good coarse mesh accuracy. For a $4 \times 4$ mesh grid, GCMQ can produce the best result when compared to all existing four-node membranes. Since the distribution of the end force is not given, a uniformly distributed pattern is assumed. Better results can be obtained by averaging tip deflections for dense mesh grids.

## 4.4 IRREGULAR AND BAD GEOMETRY

### 4.4.1 MacNeal's Thin Beam

The MacNeal's thin beam (MacNeal and Harder, 1985) shown in Fig. 4.7 is a classic example, the dimension of which is $0.2 \times 6.0$. Three different mesh grids are employed. The aspect ratio of each element is around 5. Poor results may be generated by certain elements that are sensitive to geometry. Both end shear and moment loads are applied. Numerical results

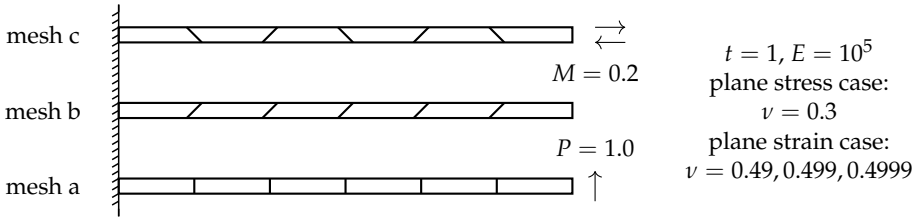


FIGURE 4.7. MacNeal's thin beam

are shown in Table 4.3. It should be noted that to reveal more significant figures, the original material properties are slightly changed here. It should also be noted that the moment load is applied as both force pair (force on the first DoF) and 'moment' (force on the third DoF). Clearly, all three versions of GCMQ do not show any sensitivity to large aspect ratios. Although accuracy varies slightly with different mesh grids, the largest error is less than 4 % (GCMQL with parallelogram mesh). Such an attribute allows more flexible mesh generation, as well as better overall performance and efficiency due to potentially fewer elements required.

TABLE 4.3. tip deflection of plane stress MacNeal's thin beam

| | shear force | | | moment as force pair | | | moment as moment | | |
|---|---|---|---|---|---|---|---|---|---|
| | mesh a | mesh b | mesh c | mesh a | mesh b | mesh c | mesh a | mesh b | mesh c |
| GCMQI | 1.0733 | 1.0488 | 1.0654 | 0.0540 | 0.0538 | 0.0537 | 0.0534 | 0.0543 | 0.0519 |
| GCMQL | 1.0733 | 1.0464 | 1.0665 | 0.0540 | 0.0537 | 0.0539 | 0.0534 | 0.0543 | 0.0521 |
| GCMQG | 1.0733 | 1.0467 | 1.0638 | 0.0540 | 0.0536 | 0.0538 | 0.0534 | 0.0538 | 0.0524 |
| ref. | 1.0812 | | | 0.0540 | | | 0.0540 | | |

### 4.4.2 Mesh Distortion

Mesh distortion is undesirable in general but cannot be avoided, especially for complex geometries. A simple cantilever beam with two elements defined is used to benchmark the sensitivity to mesh distortion. The model is shown in Fig. 4.8.

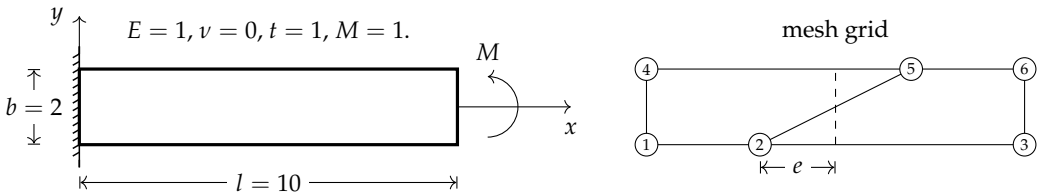


**FIGURE 4.8.** cantilever beam with mesh distortion

To exactly model the fixed boundary condition, a trivial Poisson's ratio is used. For pure bending, the analytical solution of tip deflection (Timoshenko, 1970) can be obtained as

$$v = \frac{Ml^2}{2EI} = \frac{1 \times 10^2 \times 6}{1 \times 1 \times 2^3} = 75, \tag{4.3}$$

which is identical to the solution given by the Euler beam theory. Similar to previous examples, the moment $M$ can be applied as either force pair or conjugate 'moment'. The parameter $e$ controls the degree of distortion and ranges from $-5$ to 5. Varying it gives the following results as shown in Fig. 4.9. The reciprocal condition number of the Jacobian matrix at element

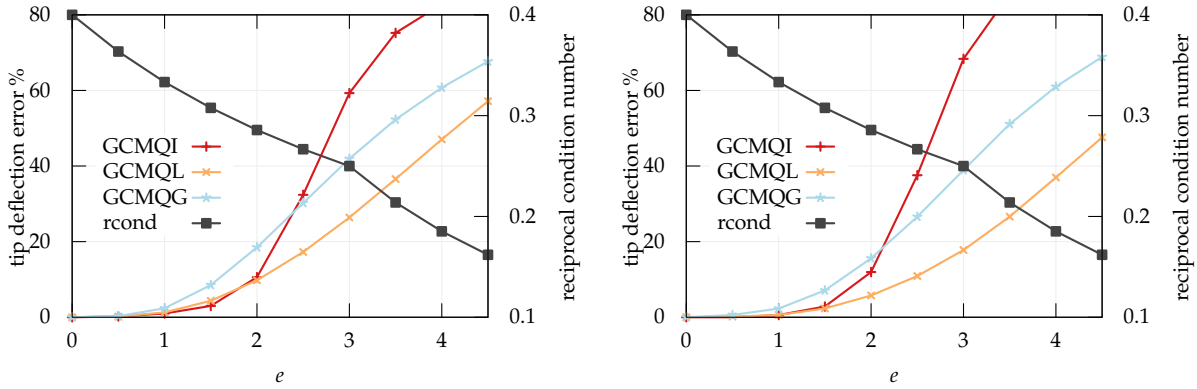


**(A)** load applied as force pair **(B)** load applied as moment

**FIGURE 4.9.** averaged tip deflection error in the mesh distortion test

centre is also plotted, which appears to be not informative about the degree of mesh distortion. Noting that the exact analytical solution is given with the absence of Poisson's effect, GCMQ can precisely describe the bending response of Euler-Bernoulli beams. Clearly, GCMQ is not fully insensitive to mesh distortion. However, compared to other elements (cf. Cen et al., 2015), the overall accuracy of GCMQ is good, especially with the Lobatto integration scheme. For all three versions, when $|e| \leqslant 1$, viz., the smallest internal angle is greater than 45°, slight accuracy degradation is observed which indicates GCMQ is almost insensitive to mesh distortion with similar mesh configurations. Such a threshold can be relaxed to even $|e| \leqslant 2$, which corre-

sponds to a rarely seen element geometry in practical simulations. Practically, as long as the mesh grid is not extremely distorted, sensitivity to mesh distortion is in general not a problem.

Isoparametric mapping is known to be one of the reasons that cause sensitivity to mesh distortion (Lee and Bathe, 1993). The latest approach to address this problem is the area coordinate method (Long et al., 2010). However, the resulting elements cannot pass the $C^0$ patch test. Some asymmetric elements (e.g., Cen et al., 2015) can also address this problem, but their asymmetric feature may be undesired in some cases.

## 4.5 STRESS FIELD

### 4.5.1 Felippa's Beam

Felippa's beam (Felippa, 1966) is a cantilever beam subjected to parabolic end shear. The configuration of which is shown in Fig. 4.10.

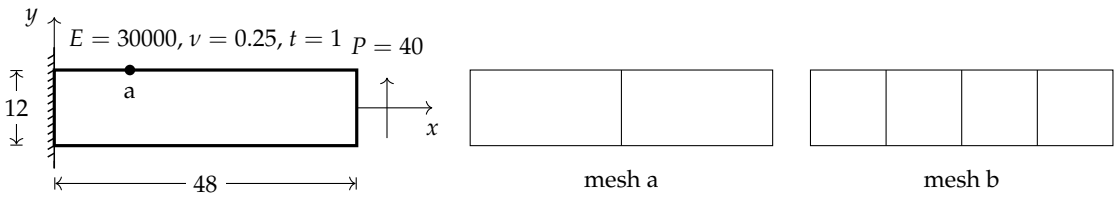


FIGURE 4.10. cantilever beam with regular mesh

Numerical results are shown in Table 4.4. For mesh a, the stress result is identical to the analytical one. For mesh b, as the stress field is discontinuous between elements, two different values are given by two adjacent elements at the same point. However, the averaged value 60, as given in the table, equals the analytical solution.

TABLE 4.4. displacement and stress results of Felippa's beam

| | mesh a | | mesh b | |
|---|---|---|---|---|
| | $v_{tip}$ | $\sigma_{x,a}$ | $v_{tip}$ | $\sigma_{x,a}$ |
| GCMQI(L) | 0.3333 | 60 | 0.3493 | 60 |
| GCMQG | 0.3333 | - | 0.3493 | - |
| ref. | 0.3558 | 60 | | |

Since GCMQG does not use corner nodes as integration points, stress results are not shown here. But it is always possible to use interpolation parameter $\boldsymbol{\alpha}$ to recover the corresponding stress distribution.

### 4.5.2 Plate With Circular Hole

For a sufficiently large plate with a circular hole subjected to uniform tension as shown in Fig. 4.11, the stress distribution around the hole can be obtained by the Kirsch's solution (see Timoshenko, 1970, pg. 80).

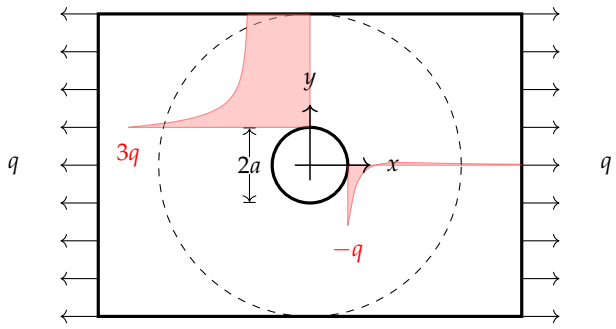


**FIGURE 4.11.** plate with circular hole

The normal stress $\sigma_y$ along $x$-axis is

$$\sigma_y = q\left(\frac{1}{2}\frac{a^2}{\rho^2} - \frac{3}{2}\frac{a^4}{\rho^4}\right), \tag{4.4}$$

while the normal stress $\sigma_x$ along $y$-axis is

$$\sigma_x = q\left(1 + \frac{1}{2}\frac{a^2}{\rho^2} + \frac{3}{2}\frac{a^4}{\rho^4}\right), \tag{4.5}$$

where $\rho$ is the polar coordinate.

A quarter of the plate is analysed using the following mesh grids and a plane stress isotropic elastic material model with Young's modulus of $E = 1000$ and Poisson's ratio of $\nu = 0.2$. To

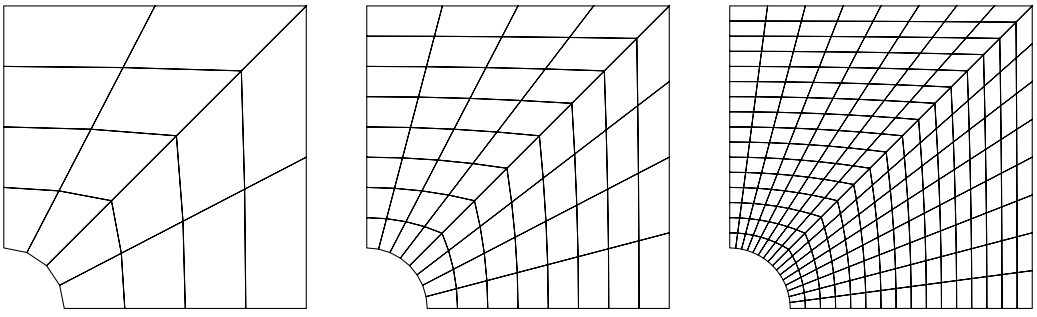


**FIGURE 4.12.** mesh grids for plate with circular hole

avoid any potential ambiguity in stress averaging process, here only GCMQI and GCMQL are

presented as GCMQG requires extrapolation. All stress values are directly obtained without any post-processing. Finite element results are shown in Fig. 4.13. Due to finite element dis-

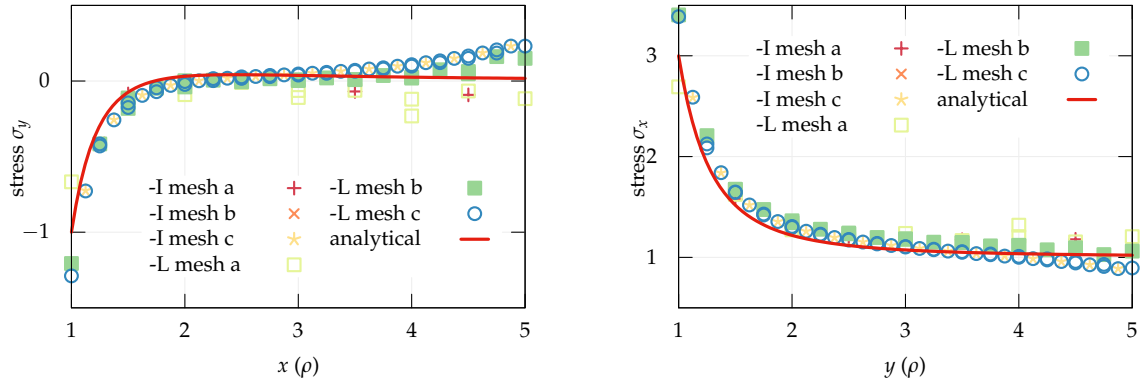


**(A)** vertical stress $\sigma_y$ distribution at $y = 0$ **(B)** horizontal stress $\sigma_x$ distribution at $x = 0$

**FIGURE 4.13.** stress prediction for plate with circular hole

cretization, the exact Kirsch's solution **cannot** be obtained. However, numerical solution stays close to analytical one and with mesh b, a relatively accurate result is obtained. Mesh a is simply too coarse to map Eq. (4.4) and Eq. (4.5), although the error is still bounded within a reasonable range. The work by Madeo et al. (2014) is referred to here for more comparisons between numerical and analytical solutions.

Furthermore, as the mesh grid becomes denser, GCMQI tends to produce the same stress field as of GCMQL. This means, if a dense mesh grid is used, analysts could consider to use GCMQI instead of GCMQL for better efficiency, if stability is not an issue. Compared to traditional displacement based elements, as there is no additional treatment required for recovering the strain and stress fields, GCMQ omits uncertainties that exist in most strain/stress averaging methods, which often lead to less accurate results by their nature, and further simplifies numerical analysis work flow. For a moderately smooth stress distribution, it can be seen that the interpolated field is reasonable and relatively accurate even with a coarse mesh grid. However, for an extremely discontinuous stress field, which is quite common in elasto-plastic cases, a point-wise accurate stress field is in general not achievable without mesh refinements.

## 4.6 VOLUMETRIC LOCKING

Volumetric locking arises in (near) incompressible problems. Completely incompressible materials, viz., $\nu = 0.5$, are not considered here as the corresponding elasticity matrix is un-

bounded for common isotropic materials. For those materials, special constitutive models can be developed, for example the Mooney-Rivlin model for rubber-like materials. Here only near incompressible isotropic materials are considered. Plane stress problems are not valid for showcasing the sensitivity to volumetric locking. In the following examples, the plane strain condition is applied by default.

### 4.6.1 Thick-Walled Cylinder

A thick-walled cylinder was first proposed by MacNeal and Harder (1985) for testing the sensitivity to volumetric locking of new elements.

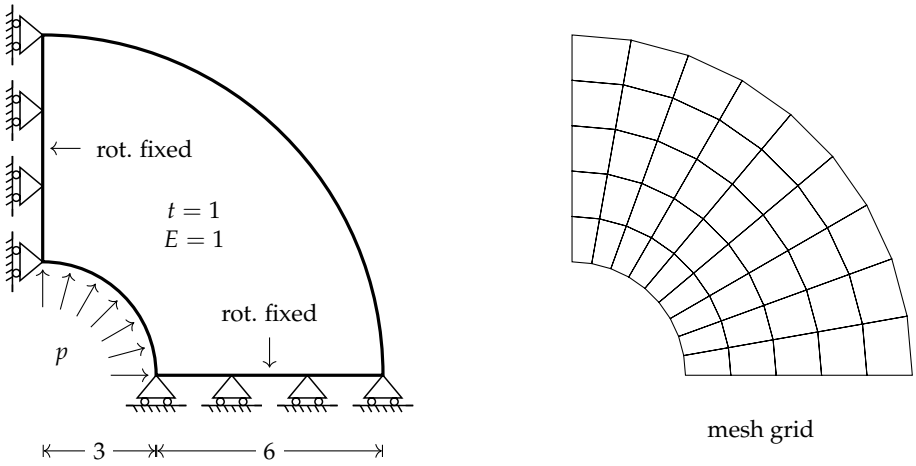


**FIGURE 4.14.** thick-walled cylinder subjected to unit pressure

The model and the corresponding mesh grid used are shown in Fig. 4.14. The analytical solution of radial displacement is given by

$$u = \frac{(1+\nu)\, pR_1^2}{E\left(R_2^2 - R_1^2\right)} \left( \frac{R_2^2}{r} + (1-2\nu)\, r \right), \tag{4.6}$$

where $p$ is the pressure, $R_1$ is the inner radius and $R_2$ is the outer radius. For $r = R_1$,

$$u = \frac{3}{4}(1+\nu)(5-\nu), \tag{4.7}$$

Numerical results with different Poisson's ratios are shown in Table 4.5. No volumetric locking is observed as the error stays around the same level (3 %) for all valid Poisson's ratios. The numerical failure is caused by the ill-conditioned stiffness matrix, rather than the element formulation. In fact, GCMQ accepts completely incompressible material, viz., $\nu = 0.5$, in which

the corresponding $\boldsymbol{C}$ matrix is well-conditioned.

**TABLE 4.5.** inner radial displacement of thick-walled cylinder

| $\nu$ | 0.49 | 0.499 | 0.4999 | 0.49999 | 0.499999 | 0.4999999 | 0.49999999 |
|---|---|---|---|---|---|---|---|
| GCMQI | 4.8888 | 4.8988 | 4.8997 | 4.8997 | 4.8998 | 4.8998 | 4.8998 |
| GCMQL | 4.8850 | 4.8942 | 4.8950 | 4.8951 | 4.8951 | 4.8951 | 4.8951 |
| GCMQG | 4.8852 | 4.8941 | 4.8949 | 4.8950 | 4.8950 | 4.8950 | 4.8950 |
| SGCMQI | 4.8884 | 4.8981 | 4.8990 | 4.8991 | 4.8991 | 4.8991 | 4.8991 |
| SGCMQL | 4.8848 | 4.8940 | 4.8948 | 4.8949 | 4.8949 | 4.8949 | 4.8949 |
| SGCMQG | 4.8840 | 4.8927 | 4.8935 | 4.8935 | 4.8936 | 4.8936 | 4.8936 |
| analytical | 5.0399 | 5.0602 | 5.0623 | 5.0625 | 5.0625 | 5.0625 | 5.0625 |

### 4.6.2 MacNeal's Thin Beam

The same beam shown in § 4.4.1 is reused here with the plane strain isotropic elastic material as the second example to investigate the sensitivity to volumetric locking. Three different values of Poisson's ratio are used, the corresponding numerical results are listed in Table 4.6.

**TABLE 4.6.** tip deflection of MacNeal's thin beam

| | shear force | | | moment as force pair | | | moment as moment | | |
|---|---|---|---|---|---|---|---|---|---|
| | mesh a | mesh b | mesh c | mesh a | mesh b | mesh c | mesh a | mesh b | mesh c |
| | | | | $\nu = 0.49$ | | | | | |
| GCMQI | 0.8159 | 0.7947 | 0.8078 | 0.0410 | 0.0408 | 0.0408 | 0.0395 | 0.0401 | 0.0386 |
| GCMQL | 0.8159 | 0.7956 | 0.8103 | 0.0410 | 0.0409 | 0.0409 | 0.0395 | 0.0403 | 0.0384 |
| GCMQG | 0.8159 | 0.7966 | 0.8102 | 0.0410 | 0.0409 | 0.0409 | 0.0395 | 0.0400 | 0.0382 |
| ref. | 0.8217 | | | 0.0410 | | | 0.0410 | | |
| | | | | $\nu = 0.499$ | | | | | |
| GCMQI | 0.8063 | 0.7849 | 0.7978 | 0.0406 | 0.0403 | 0.0403 | 0.0389 | 0.0396 | 0.0381 |
| GCMQL | 0.8063 | 0.7861 | 0.8007 | 0.0406 | 0.0404 | 0.0404 | 0.0389 | 0.0397 | 0.0379 |
| GCMQG | 0.8063 | 0.7872 | 0.8007 | 0.0406 | 0.0404 | 0.0404 | 0.0389 | 0.0395 | 0.0377 |
| ref. | 0.8121 | | | 0.0406 | | | 0.0406 | | |
| | | | | $\nu = 0.4999$ | | | | | |
| GCMQI | 0.8054 | 0.7839 | 0.7968 | 0.0405 | 0.0402 | 0.0402 | 0.0389 | 0.0395 | 0.0381 |
| GCMQL | 0.8054 | 0.7852 | 0.7998 | 0.0405 | 0.0404 | 0.0404 | 0.0389 | 0.0397 | 0.0378 |
| GCMQG | 0.8054 | 0.7862 | 0.7997 | 0.0405 | 0.0403 | 0.0404 | 0.0389 | 0.0395 | 0.0376 |
| ref. | 0.8111 | | | 0.0405 | | | 0.0405 | | |

No volumetric locking is observed with varying loading cases and Poisson's ratios. As discussed in § 3.5.3, GCMQ is expected to be free from volumetric locking. The error of each configuration stays at about the same level for all three different Poisson's ratios and is smaller than that of US-ATFQ4 (Cen et al., 2015).

As aforementioned, the conjugate force of rotation (the third DoF) can be deemed as 'nodal moment'. However, external moments applied in this way tend to produce less accurate results, in particular, the error is about 5 % greater than that of the other cases.

## 4.7 SHEAR LOCKING

Shear locking could be a problem for lower order elements. However, as long as not all of drilling DoFs are fixed (see for example the previous eigenanalysis), it is less concerning in GCMQ by its construction. The MacNeal's thin beam in § 4.4.1 can be used here. With the end shear force applied, the greatest error is about 4 %, indicating that the proposed GCMQ element is free from shear locking.

Noting that the element formulation does not involve strain rate, it is expected that GCMQ is free from shear locking under transient loading.

## 4.8 CONVERGENCE RATE

To close this chapter, the convergence rate of the proposed GCMQ and SGCMQ elements is investigated. An example of L-shaped specimen with displacement load applied on the top

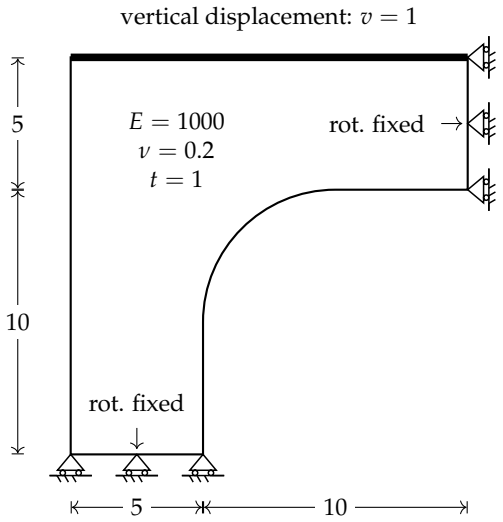


FIGURE 4.15. L-shaped specimen with displacement load

boundary, which is shown in Fig. 4.15, is chosen to eliminate the biases introduced by different force patterns applied on nodes.

The convergence performance of vertical resistance is shown in Fig. 4.16. The drilling degrees of freedom of both ends are constrained to precisely describe the corresponding boundary conditions. Different mesh refinements show no noticeable difference among different versions of GCMQ and SGCMQ, hence only one line is shown for brevity. The reference value is ob-

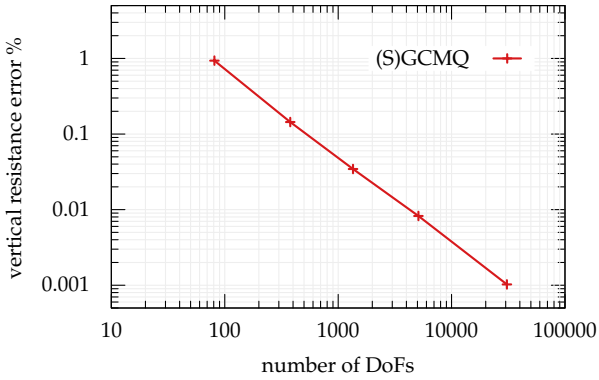


**FIGURE 4.16.** vertical resistance error v.s. number of DoFs

tained by using a mesh grid of GCMQI elements with 121 503 degrees of freedom. The slope is found to be 1.15. The theoretical convergence rate is not achievable as stated by Zienkiewicz et al. (2013), the convergence rate of (S)GCMQ is better than Q4 but slower than Q8, approximately equals to other similar elements. This is possibly due to the generalised conforming nature of its mixed formulation. Further work may be required to reveal more technical details.

# 5

# Material Models

This chapter presents all existing material models used in this work and serves as a reference. Simple models such as the von Mises model are first introduced. They are used to investigate the performance baseline of (S)GCMQ regarding elasto-plastic applications. Since reinforced concrete shear wall specimens are also involved in this work, models of reinforcement, plain concrete and reinforced concrete are discussed, respectively. Noting that a number of material models are discussed, each model is independent to the others so that the same symbol may have different meanings in different models.

## 5.1 The von Mises Model

The von Mises model is probably the simplest plastic model and can be used to model metals. The yield surface of which can be characterised by the following function,

$$F = |\boldsymbol{s} - \boldsymbol{\beta}| - \sqrt{\frac{2}{3}}\sigma_y, \tag{5.1}$$

in which $\boldsymbol{s}$ is the deviatoric stress, $\boldsymbol{\beta}(\varepsilon_p)$ is called the back stress that can be defined as a function of plastic strain $\varepsilon_p$ and/or other internal history variables, as is the yield stress $\sigma_y(\varepsilon_p)$. An associative plastic flow is normally assumed for metal so that

$$\dot{\boldsymbol{\varepsilon}}_p = \gamma \frac{\partial F}{\partial \boldsymbol{\sigma}}, \tag{5.2}$$

in which $\gamma$ is the plastic consistency parameter. For hardening, a multilinear hardening relationship and an exponential form with a saturation limit are often used for isotropic hardening $\sigma_y(\varepsilon_p)$. For kinematic hardening $\boldsymbol{\beta}(\varepsilon_p)$, either linear or non-linear forms can be defined. Details can be seen elsewhere (see, e.g., Simo and Hughes, 1998; Chaboche, 2008).

## 5.2 REINFORCEMENT

With a discrete simulation approach, reinforcing bars are often idealized as uniaxial elements such as trusses which adopt uniaxial material models.

The uniaxial implementation of the aforementioned von Mises model can be used to model reinforcing bars. The Bauschinger effect can be modelled by incorporating a non-linear kinematic hardening rule, for example the Armstrong-Frederick rule (Frederick and Armstrong, 2007). Other popular uniaxial models include the models based on the Ramberg-Osgood relationship (Ramberg and Osgood, 1943), the Menegotto-Pinto model (Menegotto and Pinto, 1973) and the Dodd-Restrepo model (Dodd and Restrepo-Posada, 1995).

The strain-stress relationship of the Menegotto-Pinto model can be expressed as

$$\sigma_n = b\varepsilon_n + \frac{\varepsilon_n - b\varepsilon_n}{\sqrt[R]{1+\varepsilon_n^R}}, \tag{5.3}$$

with the normalized stress $\sigma_n$ and strain $\varepsilon_n$ and parameter $R$ that controls curvature defined as

$$\sigma_n = \frac{\sigma - \sigma_r}{\sigma_0 - \sigma_r}, \quad \varepsilon_n = \frac{\varepsilon - \varepsilon_r}{\varepsilon_0 - \varepsilon_r}, \quad R = R_0 - \frac{a_1\xi}{a_2 + \xi}, \quad \xi^n = \frac{\left|\varepsilon_r^n - \varepsilon_0^{n-1}\right|}{\varepsilon_{y,0}}, \qquad (n > 1). \tag{5.4}$$

The other parameters are: $b$ controls hardening, $\sigma_y = \sigma_0^0$ and $\varepsilon_y = \varepsilon_0^0$ are initial yielding stress and strain so that $E = \sigma_y/\varepsilon_y$ defines Young's modulus, and three dimensionless parameters with recommended values $R_0 = 20$, $a_1 = 18.5$ and $a_2 = 0.15$. $\xi$ controls the Bauschinger effect. It can be set to zero so that $R = R_0$ remains unchanged for the whole loading history. As the result, the corresponding response resembles the one of a bilinear hardening material. Additional parameters may be introduced to account for isotropic hardening (see Filippou et al., 1983). An illustrative model is shown in Fig. 5.1. Noting that most steel models exhibit the ratcheting mechanism which would result in the increment of the maximum strain without increasing the maximum stress under cyclic loading.

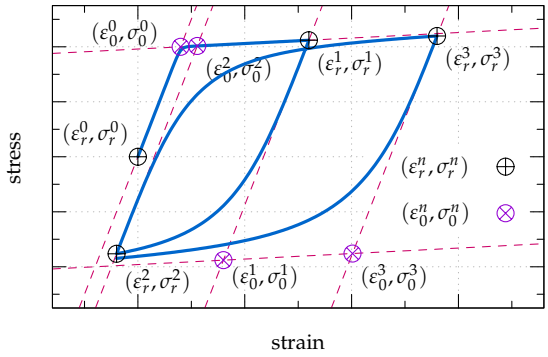


**FIGURE 5.1.** illustration of a typical Menegotto-Pinto model

If reinforcement is implemented in a smeared approach, it is in general difficult to model bar buckling failure precisely. A popular solution is to directly modify the corresponding intact material model by, for example, adding a degradation factor. Dhakal and Maekawa (2002) proposed a general modification that can be used with any existing models. It shall be stressed that bar buckling may play a vital role in modelling failure of slender walls. The degradation part of hysteresis loops may be largely affected and controlled by bar buckling.

## 5.3 CONCRETE

The plastic-damage model proposed by Lee and Fenves (1998) is used to model concrete in-plane behaviour with the assist of a plane stress wrapper. A similar model known as the concrete damage plasticity (CDP) model, which supports user-defined backbones and degradations, is available in ABAQUS.

The uniaxial backbone curve is defined as a function of the accumulated plastic strain $\varepsilon_p$ by the following expression for both tension and compression,

$$\sigma_{\aleph} = f_{\aleph}\left((1+a_{\aleph})\exp\left(-b_{\aleph}\varepsilon_p\right) - a_{\aleph}\exp\left(-2b_{\aleph}\varepsilon_p\right)\right), \tag{5.5}$$

where the subscript $\aleph$ can be either $t$ or $c$ to represent tensile and compressive properties, $f_{\aleph}$ is the initial yield strength, $a_{\aleph}$ and $b_{\aleph}$ are two parameters that control the shape of the curve. An illustration of backbones can be seen in Fig. 5.2. Regularisations can be implemented by relating $a_{\aleph}$ and $b_{\aleph}$ with objective quantities. In specific, the model defines

$$g_{\aleph} = \int_0^{\infty} \sigma_{\aleph}\, \mathrm{d}\varepsilon_p = \frac{f_{\aleph}}{b_{\aleph}}\left(1+\frac{a_{\aleph}}{2}\right) \tag{5.6}$$

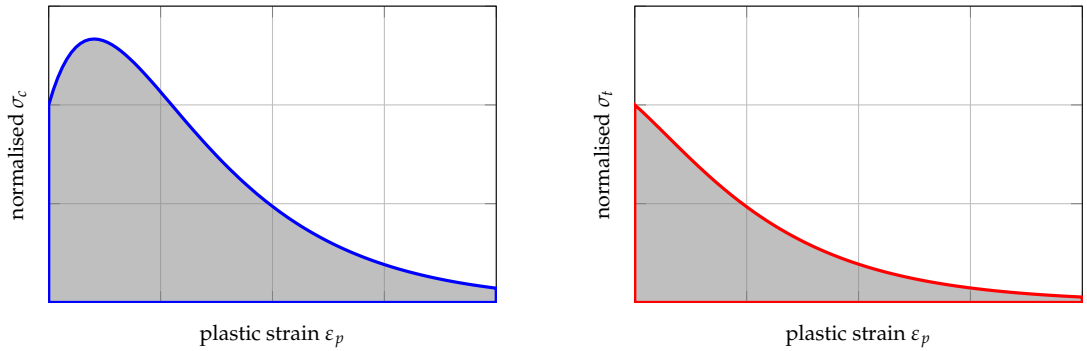


**(A)** compression **(B)** tension

**FIGURE 5.2.** example monotonic backbones used in the CDP model

to be the area under the corresponding backbone. The specific fracture energy $G_f$ can be used to control the tension softening by further defining $g_t = G_f / l_c$ where $l_c$ is the characteristic length of the target element. The compression counterpart $g_c$ can be defined in a similar fashion. $g_t$ and $g_c$ are two main model parameters that provide mesh objective response. Details can be found elsewhere (Lubliner et al., 1989).

An isotropic damage model is adopted so the stress response is defined as

$$\boldsymbol{\sigma} = (1 - D)\,\bar{\boldsymbol{\sigma}} = (1 - D)\,\boldsymbol{E}\left(\boldsymbol{\varepsilon} - \boldsymbol{\varepsilon}_p\right) \tag{5.7}$$

where $\bar{\boldsymbol{\sigma}}$ is the effective stress, $\boldsymbol{E}$ is the elastic stiffness, $D = 1 - (1 - d_c)\,(1 - s d_t)$ is a scalar degradation factor that relies on its uniaxial version $d_{\aleph}$, $s(\bar{\boldsymbol{\sigma}})$ is the stiffness recovery factor. The degradation factor $d_{\aleph}$, according to the original model (Lee and Fenves, 1998), is

$$d_{\aleph} = 1 - \exp\left(-c_{\aleph}\varepsilon_p\right) \tag{5.8}$$

where $c_{\aleph}$ is a material constant that controls the rate of degradation. By definition, $d_{\aleph}$ ranges from zero to unity.

To simplify the formulation, a normalised internal damage variable $\kappa_{\aleph}$ is adopted as a function of $\varepsilon_p$,

$$\kappa_{\aleph} = \frac{1}{g_{\aleph}} \int_0^{\varepsilon_p} \sigma_{\aleph}\, \mathrm{d}\varepsilon_p. \tag{5.9}$$

After some mathematical operations, $d_{\aleph}$ and $\sigma_{\aleph}$ can be expressed as functions of $\kappa_{\aleph}$. Hence, $\kappa_{\aleph}$ controls the developments of both damage and plasticity of the model. The evolution of

$\kappa_{\aleph}$ is related to the ratios among three principal stress components. Tensile and compressive damage can evolve separately so that tension and compression backbones can have different hardening behaviour.

For numerical implementation, parameters $b_{\aleph}$ and $c_{\aleph}$ are associated with the reference degradation factors $\bar{D}_c$ at crush strength and $\bar{D}_t$ at 50 % of the crack stress, respectively.

The yield function is defined as

$$F = \alpha I_1 + \sqrt{3J_2} + \beta \langle \hat{\sigma}_1 \rangle - (1 - \alpha)\, c, \tag{5.10}$$

in which $I_1$ is the first invariant of stress, $J_2$ is the second invariant of deviatoric stress, $\alpha$ is a dimensionless constant, $\beta(\kappa_{\aleph})$ and $c(\kappa_{\aleph})$ are the cohesion related parameters, $\hat{\sigma}_1$ is the algebraic maximum eigenvalue of stress and $\langle \cdot \rangle$ is the Macaulay bracket.

A Drucker-Prager type function is used as the plastic potential,

$$G = \sqrt{2J_2} + \alpha_p I_1, \tag{5.11}$$

where $\alpha_p$ is a material constant that controls dilatation.

Other recently proposed 3D concrete models, such as CDPM1 (Grassl and Jirásek, 2006) and CDPM2 (Grassl et al., 2013), can also be used. However, some of these models may have difficulties in deriving the corresponding consistent tangent stiffness matrices. In those cases, some low rank update algorithms (e.g., Shanno, 1970) can be adopted to obtain secant stiffness matrices. Noting that the state determination algorithm presented in Algorithm 1 is based on consistent tangent stiffness, a secant version can also be derived in the case of secant stiffness matrices.

## 5.4 A SIMPLE CONCRETE MODEL

A simple biaxial concrete model based on uniaxial concrete models is constructed to illustrate an alternative in this section. A series of work existing in current literature is adopted for different parts of this simple model. The purpose of this section is to show a usable model for modelling in-plane behaviour of concrete, rather than to justify if it is more accurate.

### 5.4.1 Biaxial Formulation

Here a simple concrete model based on the fixed crack theory that resembles the one by Crisfield and Wills (1989) is adopted. For any given strain $\boldsymbol{\varepsilon} = \begin{bmatrix} \varepsilon_x & \varepsilon_y & \gamma_{xy} \end{bmatrix}^{\mathrm{T}}$ in the global coordinate system, it can be transformed into a local coordinate system by applying a rotation so that

$$\hat{\boldsymbol{\varepsilon}} = \boldsymbol{P}\boldsymbol{\varepsilon}, \tag{5.12}$$

where $\hat{\boldsymbol{\varepsilon}} = \begin{bmatrix} \varepsilon_{x'} & \varepsilon_{y'} & \gamma_{x'y'} \end{bmatrix}^{\mathrm{T}}$. The transformation matrix $\boldsymbol{P}$ is can be expressed in terms of rotation angle $\theta$, that is

$$\boldsymbol{P} = \begin{bmatrix} \dfrac{1+\cos 2\theta}{2} & \dfrac{1-\cos 2\theta}{2} & \dfrac{\sin 2\theta}{2} \\ \dfrac{1-\cos 2\theta}{2} & \dfrac{1+\cos 2\theta}{2} & -\dfrac{\sin 2\theta}{2} \\ -\sin 2\theta & \sin 2\theta & \cos 2\theta \end{bmatrix}. \tag{5.13}$$

The angle $\theta$ equals the principal angle prior to the first yield, in which case $\gamma_{x'y'} = 0$. Once either tensile or compressive strength is reached, $\theta$ is fixed in subsequent computation. The local quantities can be transformed back to the global coordinate system, for example,

$$\boldsymbol{\sigma} = \boldsymbol{P}^{\mathrm{T}}\hat{\boldsymbol{\sigma}}. \tag{5.14}$$

Accordingly, the conversion between two stiffness matrices can be expressed as

$$\boldsymbol{K} = \boldsymbol{P}^{\mathrm{T}}\hat{\boldsymbol{K}}\boldsymbol{P}. \tag{5.15}$$

For simplicity, there is no coupling between response along two orthogonal directions. So the yield surface in 2D space is a square (Rankine type). There are other models that incorporate Poisson's ratio in the formulation. If only one Poisson's ratio is used, the corresponding stiffness is not symmetric. It is also possible to treat cracked concrete as anisotropic material so that more than one Poisson's ratio could be adopted to better describe the post-crack behaviour. The stress and stiffness along each local direction is computed via the corresponding uniaxial concrete material model.

### 5.4.2 Uniaxial Concrete Behaviour

There are many uniaxial concrete models in current literature (e.g., Kent and Park, 1971; Popovics, 1973; Tsai, 1988; Chang and Mander, 1994). In this work, Tsai's equation (Tsai, 1988) is used as the uniaxial backbone for compression. It can be written as

$$\frac{\sigma}{f_c} = \frac{m}{1+\left(m-\frac{n}{n-1}\right)\frac{\varepsilon}{\varepsilon_c}+\frac{1}{n-1}\left(\frac{\varepsilon}{\varepsilon_c}\right)^n}\frac{\varepsilon}{\varepsilon_c}, \tag{5.16}$$

where $m$ and $n$ are two empirical parameters that control the pre-peak and post-peak shape of the curve respectively, following values are recommended by Tsai (1988) for compression,

$$m = 1+\frac{17.9}{f_c}, \tag{5.17}$$

$$n = \frac{f_c}{6.68} - 1.85 > 1, \tag{5.18}$$

with $f_c > 0$ (MPa) and $\varepsilon_c > 0$ denote the peak compressive stress and the corresponding strain, respectively. The tension backbone is defined in a similar fashion but with modified $m$ and $n$. Fig. 5.3 shows a cluster of backbones with different parameters.

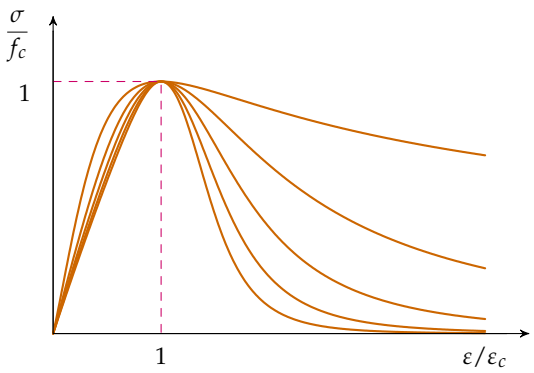


**FIGURE 5.3.** illustration of Tsai's equation

The residual strains along both directions are computed according to the empirical equations proposed by Chang and Mander (1994).

$$\varepsilon_r^+ = \varepsilon_{un}^+ - \frac{f_{un}^+\varepsilon_{un}^+ + 0.67f_{un}^+\varepsilon_t}{f_{un}^+ + 0.67E\varepsilon_t}, \tag{5.19}$$

$$\varepsilon_r^- = \varepsilon_{un}^- - \frac{f_{un}^-\varepsilon_{un}^- + 0.57f_{un}^-\varepsilon_c}{f_{un}^- + 0.57E\varepsilon_c}, \tag{5.20}$$

where superscripts $^+$ and $^-$ denote tension and compression respectively, $f_{un}$ and $\varepsilon_{un}$ is the maximum unload stress and strain, $\varepsilon_t$ and $\varepsilon_c$ are the crack and peak strains. The unloading/reloading behaviour is assumed to be linear. Whenever load reversal occurs, the response varies linearly between the corresponding residual strain point and the point that corresponds to a given level of unloading stress on the opposing unloading path.

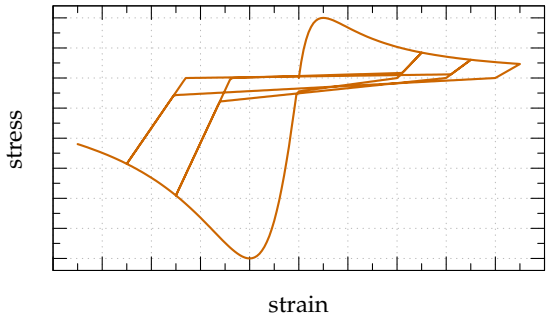


**FIGURE 5.4.** illustration of hysteresis rule

Fig. 5.4 shows an illustration of the adopted hysteresis rule. The peak stress is chosen to be close to the crack stress so that the hysteresis loop can be better seen. It thus does not correspond to any real concrete behaviour. Other more complex hysteresis rules can be applied, although in which small cycle behaviour can be carefully treated.

### 5.4.3 Shear Response

Due to the lack of a proper nonlinear shear response, a bilinear elastic relationship can be defined. For the hardening branch, a shear retention factor $\beta$ can be adopted so the hardening modulus can be defined as $\beta G$. The corresponding yielding shear stress can be limited to a user-defined value that may be associated with the tensile strength.

## 5.5 REINFORCED CONCRETE

For reinforced concrete, there are many in-plane models available, including well-known ones such as MCFT (Vecchio and Collins, 1986), CSMM (Hsu and Zhu, 2002) and their variants. The basic strategy adopted by those models is to decompose total strain either in the principal space (for a rotating crack theory) or along a fixed direction (for a fixed crack theory). Each strain component can be further split into different portions to account for various effects. Reinforcement is included in a smeared manner. Local phenomena such as aggregate locking,

stress transition/concentration and dowel action, can also be considered.

However, due to that many models (MCFT, DSFM (Vecchio, 2000), FA-STM, etc.) perform strain decompositions and use stress equilibrium as the governing equation, iterations are required to compute trial state and often only the secant stiffness is available. The overall state updating algorithm has a very slow convergence rate (sub-linear) and often faces difficulties in the unloading stage. For example, MCFT (at least the original version) does not define any unloading behaviour and thus can only be used in analyses under monotonic loading.

In this work, reinforcement is modelled independently in a smeared approach. Hence interactions between reinforcement and host concrete, such as dowel action, bar buckling and confinement, are not considered (not in an discrete way but still can be accounted for by modifying material models). The total material stiffness $\boldsymbol{D}$ and stress $\sigma$ can be expressed as the superposition of concrete and reinforcement response.

$$\boldsymbol{D} = \boldsymbol{D}_c + \boldsymbol{D}_s, \quad \sigma = \sigma_c + \sigma_s, \tag{5.21}$$

where $\boldsymbol{D}$ is the overall material stiffness, subscripts $_c$ and $_s$ denote concrete and reinforcement portion, respectively. $\boldsymbol{D}_s$ is often assumed to be orthogonal so that

$$\boldsymbol{D}_s = \begin{bmatrix} \rho_x E_x & 0 & 0 \\ 0 & \rho_y E_y & 0 \\ 0 & 0 & 0 \end{bmatrix}, \quad \sigma_s = \begin{bmatrix} \rho_x \sigma_x \\ \rho_y \sigma_y \\ 0 \end{bmatrix}, \tag{5.22}$$

where $\rho_x$ and $\rho_y$ are two reinforcement ratios along two axes, $E_x$ and $E_y$ are corresponding steel moduli. It shall be stressed that, although the smeared approach is used, GCMQ itself does not impose any constraint on the implementation of reinforcement. The discrete approach, or a combined method, could be employed as well.

# 6

# Applications of GCMQ and SGCMQ

This chapter is aimed to present a series of performance investigations of (S)GCMQ, including both static and dynamic applications. Noting that all examples shown are not meant for validating the adopted material models so justifications of the corresponding model parameters are not discussed.

Part of this chapter is published in the journal paper *Numerical Evaluations of A Novel Membrane Element in Simulations of Reinforced Concrete Shear Walls* (Chang et al., 2019b) with **Engineering Structures**.

## 6.1 Square Panel

A unit square panel with unit thickness is analysed by using (S)GCMQ with plane stress condition in this section. One edge of the panel is fully fixed while a uniform shear deformation is applied on the opposite edge. The other two are free edges. Both hardening and softening materials are involved.

### 6.1.1 With Hardening Material

The linear isotropic hardening von Mises material with the following material parameters is adopted: elastic modulus $E = 30\,\text{GPa}$, Poisson's ratio $\nu = 0.2$, yield stress $\sigma_y = 5\,\text{MPa}$ and hardening ratio $b = 0.05$.

Numerical results are shown in Fig. 6.1. It can be seen that with only one element defined, the result of SGCMQG differs from that of SGCMQI and SGCMQL. In this particular example, stresses on two free edges are always larger than that of element interior, SGCMQG tends to be less capable of capturing initial plasticity development due to its layout of integration points. Such a difference may not lead to less accurate results in other cases.

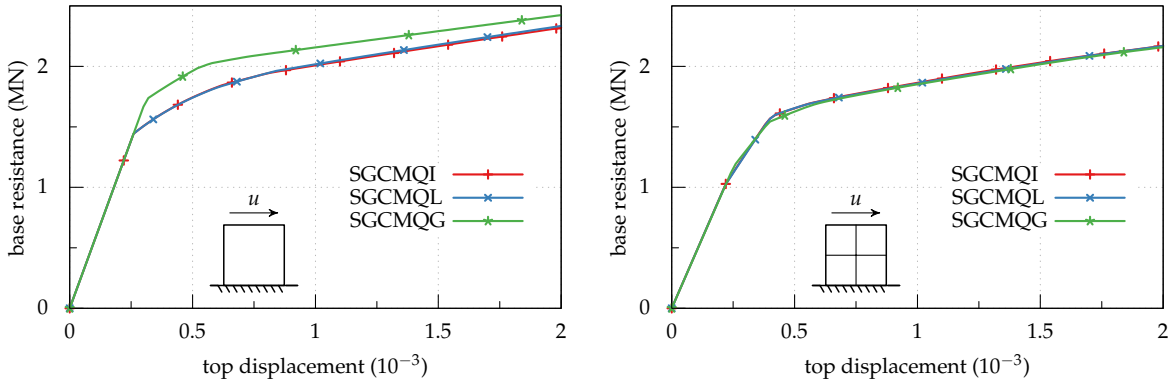


(A) $1 \times 1$ mesh (B) $2 \times 2$ mesh

FIGURE 6.1. performance baseline of SGCMQ

With $2 \times 2$ meshes, all three schemes give similar results, the error of base resistance is around 8 %, which is consistent with the results of linear validations. It could thus be concluded that SGCMQI is preferable due to its efficiency if a $2 \times 2$ or denser mesh is used.

### 6.1.2 With Softening Material

The CDP model is used to model the behaviour of plain concrete subjected to end shear. Noting that strength degradation tends to be mesh dependent, which is known due to the size effect (see, e.g., Bažant and Oh, 1983), normalised fracture energy $g_t$ and its counterpart $g_c$, are strictly scaled according to their original definitions (Lubliner et al., 1989) so that mesh dependence can be largely eliminated. Both GCMQ and SGCMQ are examined in this benchmark, the corresponding numerical results are shown in Fig. 6.2. Since regularisation is supported by the CDP model, a converged response can be obtained by performing mesh refinements.

The presence of enhanced strain field leads to different responses with very coarse ($1 \times 1$) meshes. Such a difference is insignificant with denser mesh grids, in which case SGCMQ is preferable for its higher efficiency. With one element defined, a reasonably accurate initial stiffness is predicted. However, the development of plasticity is not well captured. For refined modelling tasks, it is recommended to use $2 \times 2$ or denser meshes.

It is also observed that with the CDP material model, GCMQ may have some stability issues as the quadratic convergence rate deteriorates to at most superlinear. Similar issues are not found with other elasto-plastic materials nor with other element types. This may be relevant to the common stability problem discussed by Wriggers and Reese (1996).

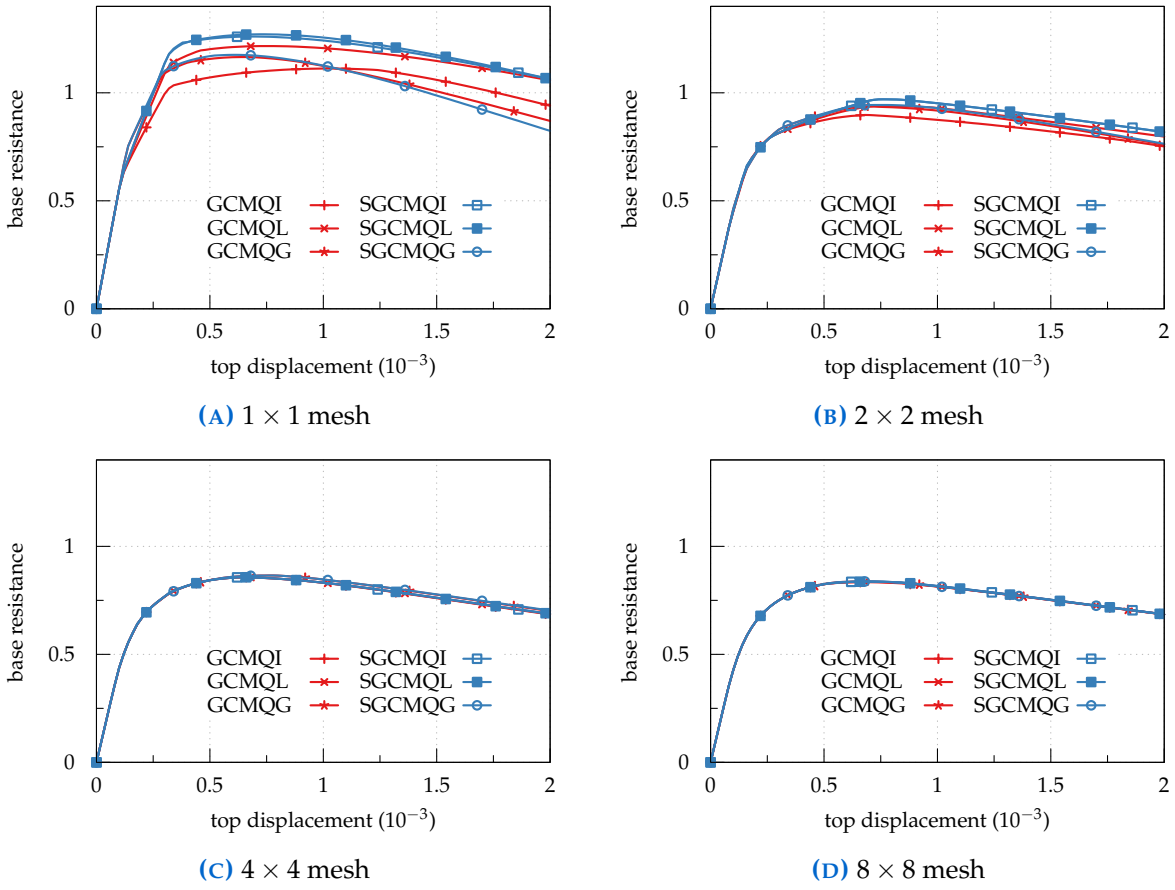


(A) $1 \times 1$ mesh (B) $2 \times 2$ mesh

(C) $4 \times 4$ mesh (D) $8 \times 8$ mesh

**FIGURE 6.2.** performance baseline of GCMQ and SGCMQ

Fig. 6.3 shows the evolution of tensile damage index $d_t$ (see § 5.3). With $1 \times 1$ meshes, the localised deformation at left bottom corner cannot be represented as strain is averaged within the element. As a result, the tensile damage is distributed over the left half of the element. With mesh refinements, such an unrealistic damage distribution quickly concentrates at left bottom corner. In conclusion, it is not practical to use only one element to perform any simulations.

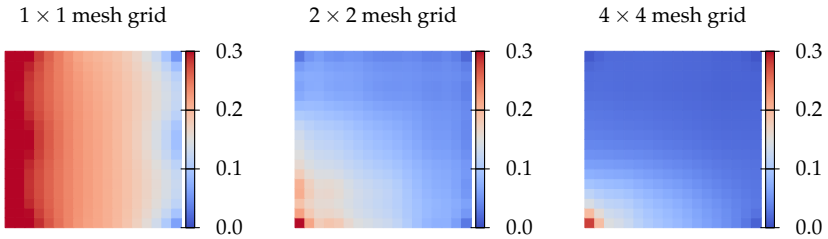


**FIGURE 6.3.** concentration of tensile degradation index $d_t$

## 6.2 PLATE WITH CIRCULAR HOLE

The plate shown in § 4.5.2 is analysed in this section with the perfectly plastic von Mises model. The following material properties are chosen: elastic modulus $E = 1000$, Poisson's ratio $\nu = 0.2$ and yielding stress $\sigma_y = 5$. A uniform displacement load is applied on the right boundary.

The distribution/concentration of the equivalent plastic strain $\bar{\varepsilon}_p$ is shown in Fig. 6.4 with three different mesh configurations (see Fig. 4.12). Due to the averaging effect, the maximum

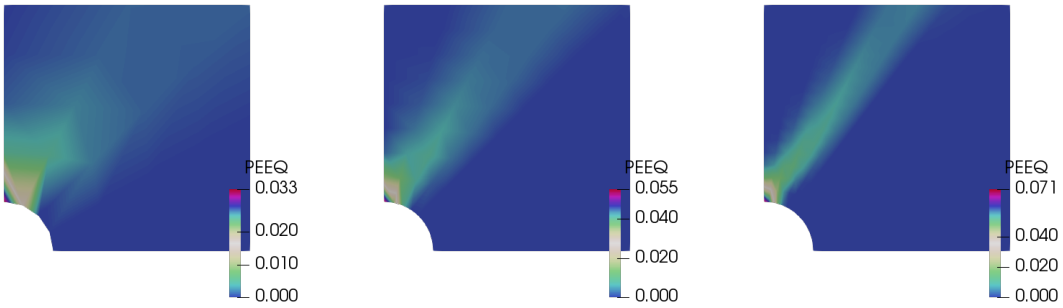


(A) coarse mesh (B) medium mesh (C) fine mesh

FIGURE 6.4. concentration of equivalent plastic strain $\bar{\varepsilon}_p$

$\bar{\varepsilon}_p$ tends to be small with coarse meshes. Concentration of plasticity development is recovered with denser meshes. An explicit plastic band can be spotted with the medium mesh.

The resistance of the left boundary is plotted in Fig. 6.5. In all cases, three integration schemes give very close results. With the coarse mesh, the maximum resistance is found to be 20.60. The error can be computed as 2.8 % compared to the converged value 20.03 given by the fine mesh.

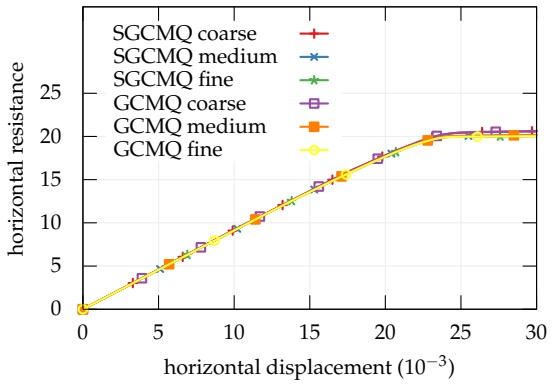


FIGURE 6.5. displacement v.s. resistance of plastic plate with circular hole

## 6.3 DOUBLE EDGE NOTCHED SPECIMEN

In this section, one of several double edge notched specimens (DENS) tested by Nooru-Mohamed (1992) is simulated by using the CDP model. This example is included to showcase the reliability of the material model, rather than the validation of the proposed element.

The specimen has a dimension of 200 mm × 200 mm × 50 mm with a notch depth of 25 mm and a width of 5 mm. The specimen is illustrated in Fig. 6.6. To simplify mesh generation, as

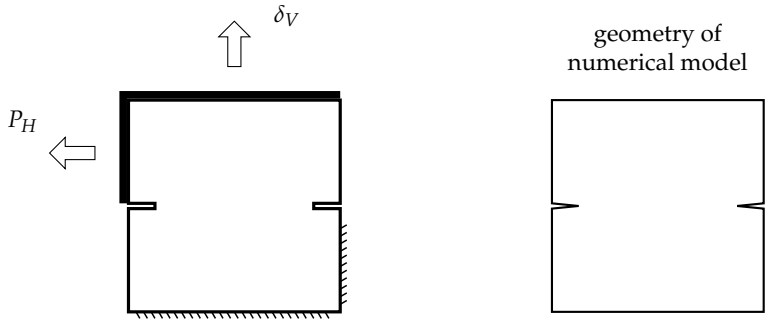


**FIGURE 6.6.** illustration of double edge notched specimen (Nooru-Mohamed, 1992)

well as to obtain more regular element meshes, the rectangular notches are idealised as triangles. The geometry of the corresponding numerical model is also shown in the same figure. A horizontal force $P_H$ of magnitude 10 kN is applied via the rigid steel frame to generate a constant shear state. Axial load is then applied in displacement control till failure.

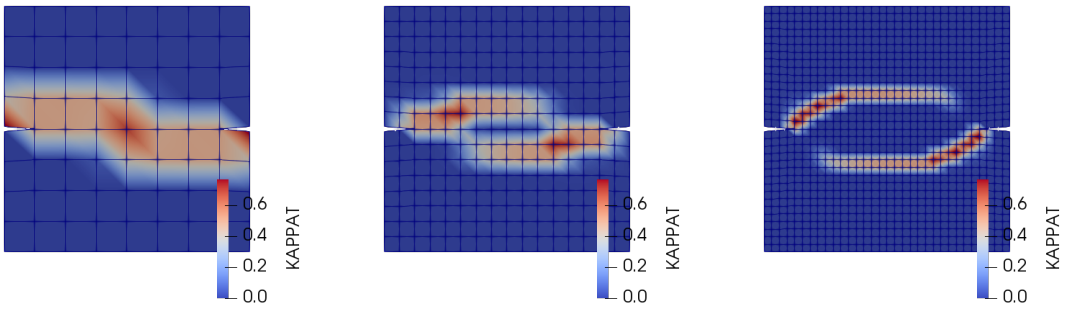


**(A)** coarse mesh **(B)** medium mesh **(C)** fine mesh

**FIGURE 6.7.** concentration of tensile damage index $\kappa_t$ at $\delta_V = 0.1$ mm

Three meshes with different densities are used with SGCMQI elements to perform the simulations. It shall be noted that although it is denoted as 'coarse mesh', the first mesh grid is considered dense enough for the given geometry that the difference between SGCMQ and other membrane elements is not significant. The distributions of tensile damage index $\kappa_t$ are

shown in Fig. 6.7. The following material properties (Pivonka et al., 2004) are used: elastic modulus $E = 32.8\,\text{GPa}$, Poisson's ratio $\nu = 0.2$, tensile strength $f_t = 3.0\,\text{MPa}$, compressive strength $f_c = 38.4\,\text{MPa}$ and specific fracture energy $G_F = 0.11\,\text{N}\,\text{m}^{-1}$.

It could be seen that the CDP model is a reliable material model for multi-scale modelling tasks. Local responses such as concentration of damage can be recovered with mesh refinement. Fig. 6.8 shows the distribution of major principal stress. The coarse mesh (64 elements) has a

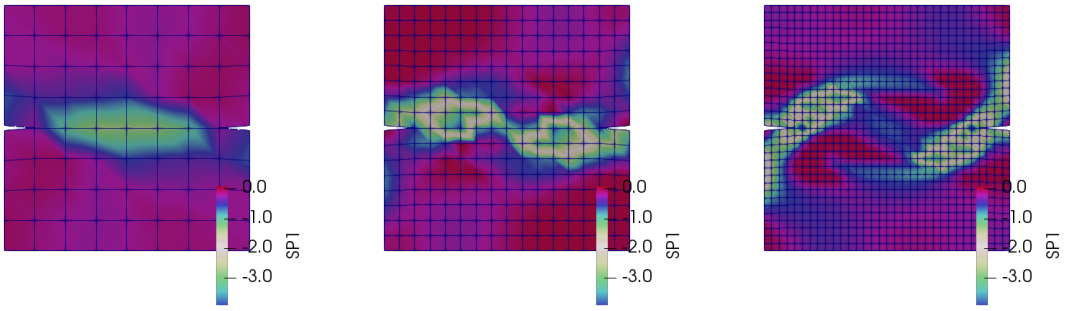


(A) coarse mesh (B) medium mesh (C) fine mesh

FIGURE 6.8. distribution of major principal stress at $\delta_V = 0.1\,\text{mm}$

poor ability of describing such a strongly non-linear stress field due to the averaging attribute of the finite element method. Some meaningful features can be spotted with the medium mesh (256 elements). The crack frontal zone can be clearly seen with the fine mesh (1024 elements). The major principal stress does not necessarily need to be positive for the crack to propagate. Fig. 6.9 also shows vertical resistance response. The peak resistance is greater than the ex-

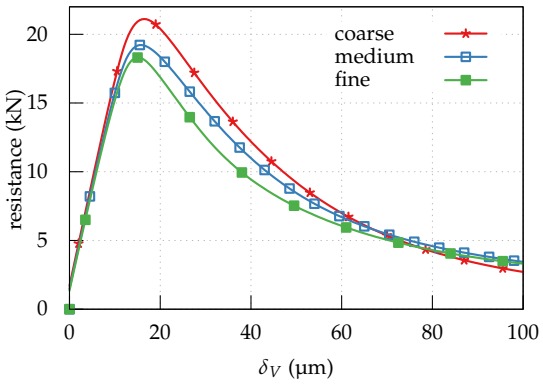


FIGURE 6.9. vertical displacement v.s. resistance of double edge notched specimen

perimental value, which is around 15 kN, but agrees with other numerical results (cf. Pivonka et al., 2004). With limited material properties, the results obtained by using the CDP model are satisfactory. It is possible to obtain better results by calibrating other material properties.

It shall be emphasised that localised responses of reinforced concrete shear walls that engineers are interested in, such as crack propagation, concrete crush and bar buckling, are impossible to be **precisely** predicted by any finite elements with coarse meshes with current numerical techniques. For studies focusing on relevant topics, dense meshes with 2D (or even 3D) elements are inevitable. By the nature of their formulations, planar elements are more versatile and advantageous than 1D elements like spring, beam, MVLEM, etc. In this sense, the effort shall be put to improve the efficiency of planar elements.

## 6.4 RC SHEAR WALL SPECIMENS UNDER MONOTONIC LOADING

The specimens LSW1, LSW2, MSW1 and MSW2 reported by Salonikios et al. (1999) are simulated in this section. Among all eleven specimens shown in the original work, the above four are suitable for investigations of SGCMQ given that they have neither axial loads nor diagonal rebars. The two boundaries are not heavily strengthened so a smeared representation will not lead to great error. A schematic illustration of the specimens, along with the $2 \times 2$ mesh grid used, is given in Fig. 6.10. Concrete is modelled by the CDP model while reinforcement

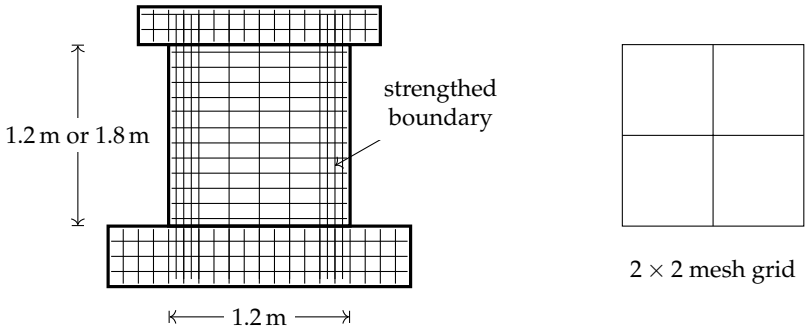


**FIGURE 6.10.** illustration of the specimens tested by Salonikios et al. (1999)

is modelled by the Menegotto-Pinto model in a smeared approach. Due to the absence of details of material properties, it is difficult to calibrate unloading/reloading behaviour, hence only monotonic envelops are shown here. The boundary columns may be strengthened, hence average values of reinforcement ratios are used. The following properties are not changed for all four specimens: elastic modulus $E = 30\,\text{GPa}$, Poisson's ratio $\nu = 0.2$, dilatation parameter $\alpha_p = 0.2$, ratio between biaxial and uniaxial compressive strengths $f_{bc}/f_c = 1.16$, reinforcement yield strength $f_y = 500\,\text{MPa}$ and the corresponding hardening ratio $b = 1\,\%$. Table 6.1 shows a summary of other material parameters used in numerical simulations.

**TABLE 6.1.** summary of material parameters used in LSW1, LSW2, MSW1 and MSW2

| | $w$ mm | $h$ mm | $t$ mm | $f_c$ MPa | $f_t$ MPa | $\rho$ % | concrete | $g_t$ kN/m$^2$ | $g_c$ MN/m$^2$ | $a_t$ | $a_c$ | $\bar{D}_t$ | $\bar{D}_c$ |
|---|---|---|---|---|---|---|---|---|---|---|---|---|---|
| LSW1 | 1200 | 1200 | 100 | 23.0 | 1.7 | 1.7 | CDP | 2.0 | 0.35 | 0.5 | 4.0 | 0.50 | 0.45 |
| LSW2 | 1200 | 1200 | 100 | 21.0 | 1.5 | 1.3 | CDP | 1.0 | 0.20 | 0.5 | 4.0 | 0.55 | 0.60 |
| MSW1 | 1200 | 1800 | 100 | 23.0 | 1.1 | 1.2 | CDP | 2.0 | 0.35 | 0.5 | 4.0 | 0.50 | 0.55 |
| MSW2 | 1200 | 1800 | 100 | 23.0 | 1.1 | 1.1 | CDP | 1.3 | 0.35 | 0.5 | 4.0 | 0.50 | 0.55 |

The numerical simulations of monotonic backbones for four specimens with three different integration schemes are shown in Fig. 6.11. In general, good agreements are observed between

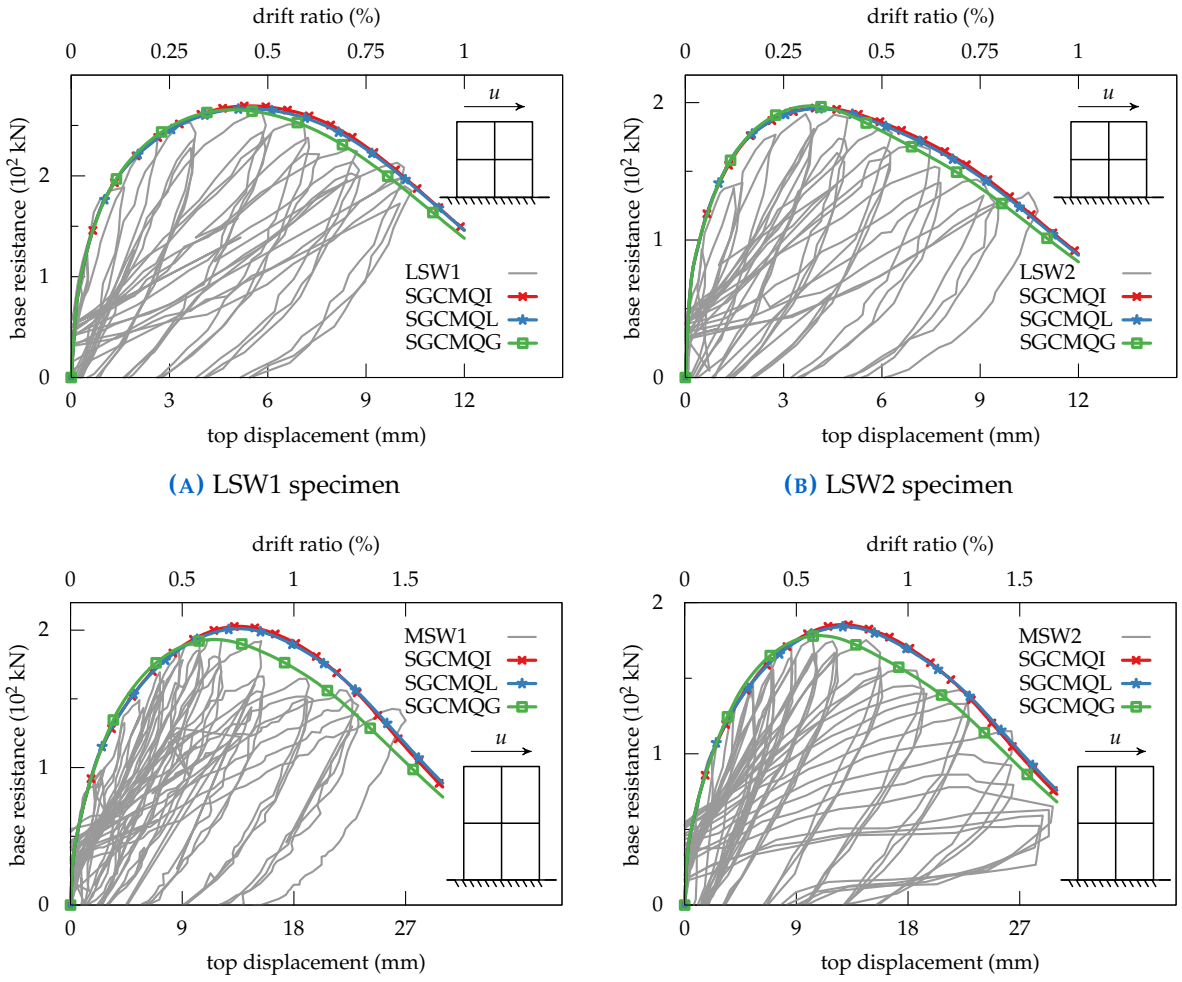


**(A)** LSW1 specimen

**(B)** LSW2 specimen

**(C)** MSW1 specimen

**(D)** MSW2 specimen

**FIGURE 6.11.** numerical results of LSW1, LSW2, MSW1 and MSW2

numerical results and experimental data. The initial stiffness, the maximum resistance and the degradation branch are well captured by numerical models. SGCMQI and SGCMQL show almost identical results, which indicates that the five-point quadrature is sufficiently accurate for elasto-plastic applications. The response of SGCMQG tends to differ from that of SGCMQI and SGCMQL due to the different arrangement of sampling/integration points, the difference may

vary from one model to another. Hence, SGCMQI and SGCMQG are the two main versions analysts could choose between while SGCMQL is less preferable in terms of both accuracy and efficiency.

Fig. 6.12 shows the evolution of tensile damage $\kappa_t$ (see § 5.3 for definition) of MSW2 specimen. Since the specimen is not axially loaded, the right half of the specimen, which is initially in compression, can eventually develop tensile damage. It can be concluded from the previous example that a $2 \times 2$ mesh may not be sufficient to recover local response in details. An expected concentration of local deformation can be observed with a denser mesh grid. However, it indeed can be observed from Fig. 6.12 that tensile damage initiates at the left bottom corner, where the maximum tensile stress occurs, and then propagates to the left half of the specimen. This is consistent with the typical shear failure pattern that engineers are familiar with.

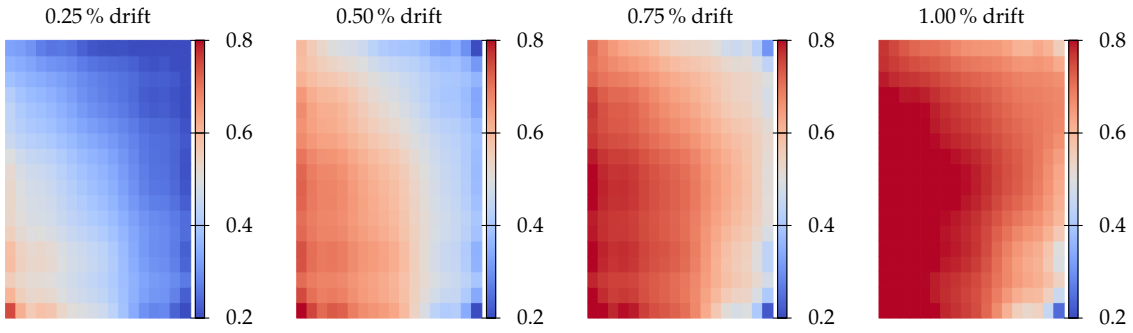


**FIGURE 6.12.** evolution of tensile damage variable $\kappa_t$ of MSW2

Mesh refinement is not carried out for this particular example. Given that reinforced concrete is modelled as a two-phase composite while regularisation of material response is only supported by the adopted concrete model, it is difficult to obtain objective results by solely adjusting the behaviour of one ingredient of the composite.

It is also observed that in the above four numerical models, the reinforcement stays elastic, the plasticity mainly occurs in the concrete. The shear failure can be naturally recovered due to the presence of a refined 3D yield surface. Most existing 2D in-plane concrete models, which treat normal and shear behaviour separately, would have difficulties in predicting the so called shear-flexure interaction.

Model configurations such as element type, mesh grid size, material properties including $g_t$ and $g_c$ (see § 5.3) may affect simulation results. The coarse mesh behaviour is investigated. It is worth mentioning that simply scaling concrete properties may not lead to objective results

as material response is now contributed to by both concrete and reinforcement. The examples shown here are not for the purpose of justifying the 'correct' material properties.

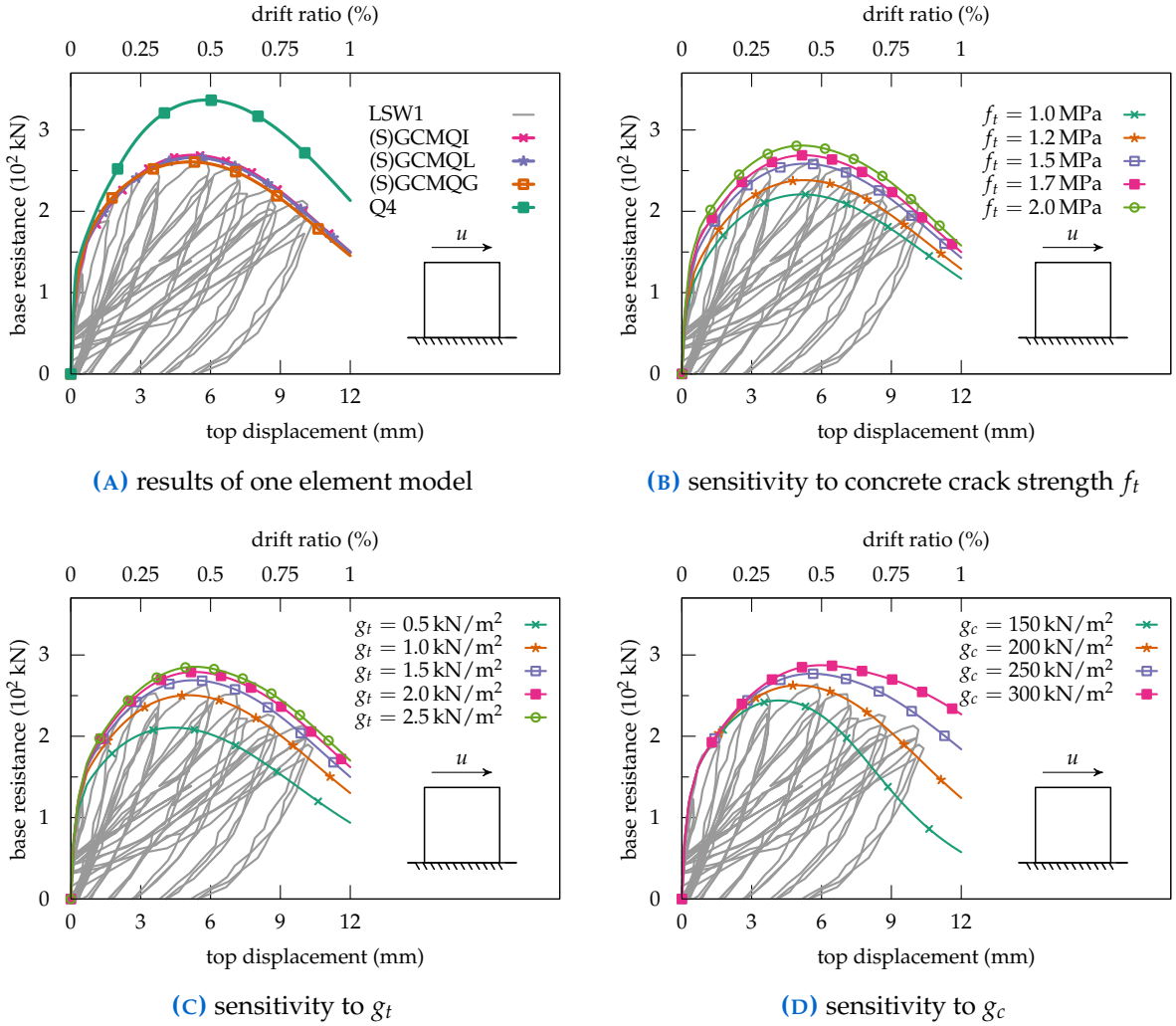


**(A)** results of one element model

**(B)** sensitivity to concrete crack strength $f_t$

**(C)** sensitivity to $g_t$

**(D)** sensitivity to $g_c$

**FIGURE 6.13.** sensitivity investigations with one elemnt model of LSW1 specimen

Fig. 6.13a shows the comparison between results of models using one GCMQ/Q4 element only. The damage parameters are set to $g_t = 15 \times 10^{-4}\,\mathrm{N/m^2}$ and $g_c = 22 \times 10^{-2}\,\mathrm{N/m^2}$, which are slightly above 50 % of the values used in the previous models with $2 \times 2$ meshes. As can be seen, with such a material configuration, GCMQ can capture loading backbones with good agreement. No significant difference is observed among three integration schemes. However, the model with Q4 element overestimates the maximum resistance by 25 % (337 kN and 269 kN). In this case, mesh refinement and adjustment of material properties are essential in order to capture a reliable response.

Fig. 6.13b, Fig. 6.13c and Fig. 6.13d show the sensitivity studies to concrete tensile strength $f_t$, along with damage parameters $g_c$ and $g_t$. Generally speaking, tension associated parameters

control the pre-peak response while compression related parameters mainly affect the post-peak response. Although tweaking material parameters would result in different behaviour, compared to the result of Q4 element, (S)GCMQ is able to produce backbone curves that are close to experiment data with a wide range of different values of material properties. Again, this is not achievable with classic finite elements such as Q4 incorporating a coarse mesh grid, let alone the macroscopic 1D elements.

## 6.5 RC SHEAR WALL SPECIMENS UNDER CYCLIC LOADING

For cyclic loading cases, two specimens RW1 and RW2 (Thomsen and Wallace, 2004) are modelled with the fixed crack concrete model (FCM) as examples. Both wall specimens have the same geometry with an identical aspect ratio of 3. The rebar layouts of the two specimens are similar with the gross reinforcement ratio around 0.5 %. The axial loads applied are 400 kN for RW1 and 380 kN for RW2. Accounting for the fact that most reinforcing bars are provided in the boundary zones in both specimens, the equivalent uniformly distributed reinforcement ratio is increased to 0.7 % in the numerical simulations to produce a similar location of neutral axis. A summary of the main model properties is presented in Table 6.2. It is worth noting

**TABLE 6.2.** summary of main material parameters used in RW1 and RW2

| | $w$ mm | $h$ mm | $t$ mm | $f_c$ MPa | $f_t$ MPa | $\rho$ % | $f_y$ MPa | $b$ | concrete | axial load kN | $m$ | $n$ |
|---|---|---|---|---|---|---|---|---|---|---|---|---|
| RW1 | 1200 | 3600 | 100 | 40.0 | 2.0 | 0.7 | 400 | 2 % | FCM | 400 | 2.0 | 2.0 |
| RW2 | 1200 | 3600 | 100 | 40.0 | 2.0 | 0.7 | 400 | 2 % | FCM | 380 | 2.0 | 2.0 |

that mesh objective response may not be available in this case, as the concrete material model used (FCM) does not support the corresponding regularisation procedure. Adjusting material properties with different meshes may give close results but no justification can be concluded from such comparisons of mesh refinements.

Numerical results are shown in Fig. 6.14. SGCMQG elements with $2 \times 2$ meshes are used in simulations. In general, the models are able to capture cyclic response with good agreement, although the initial stiffness is overestimated in both models. Many reasons, such as imperfections of specimens, flexible base-wall connections and customizable initial stiffness in the material model used, could lead to this difference.

It could be seen that with the same loading level, there is a difference between responses of

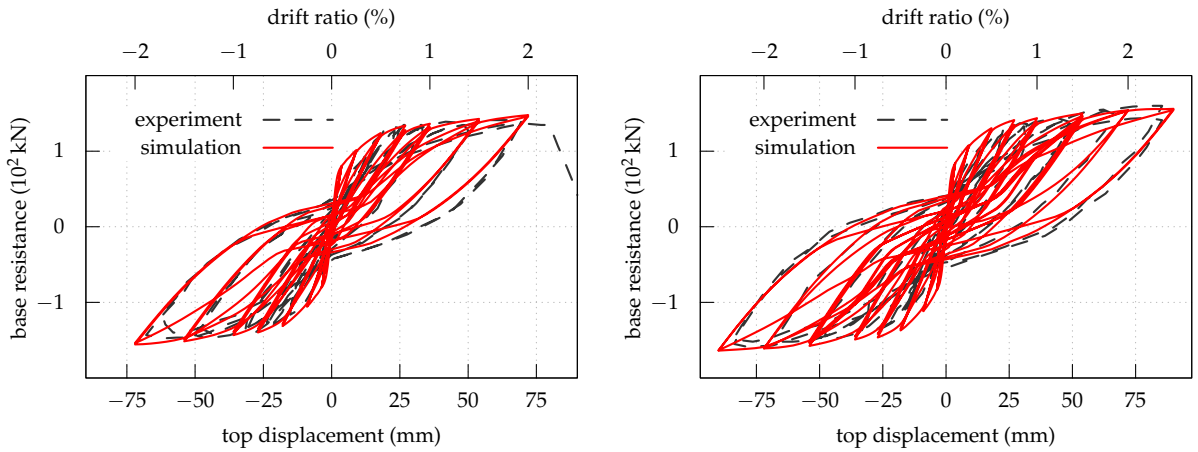


**(A)** RW1 specimen **(B)** RW2 specimen

**FIGURE 6.14.** numerical simulations of specimens RW1 and RW2

the first and second cycles. This is mainly due to the concrete unloading/reloading behaviour. The hysteresis rule is controlled by both unloading points. The update of either would lead to a different unloading/reloading path. Justifications of material models are not the main focus of this work. Further refinement of hysteresis behaviour is possible with a more complex material hysteresis rule applied (e.g., Chang and Mander, 1994).

With a coarse mesh grid ($2 \times 2$), it is difficult to recover a precise strain profile along wall width as the strain field is averaged over a finite element domain. This issue exists in all numerical models including the ones using macroscopic elements. For investigations of local response, (local) mesh refinement is inevitable. However, SGCMQ shows a good performance in terms of global response. Noting that the aspect ratio of the element used can be as large as 3, SGCMQ is tolerant to element geometry.

For elasto-plastic applications, most analysis time is spent on the state determination of material responses. From the previous two examples, it is observed that switching from the CDP model to the FCM model does save a significant amount of time. As long as the employed material model is cost efficient, it is reasonable to conclude that SGCMQ can be used for modelling large scale structures with a relatively higher accuracy and a lower computational demand.

## 6.6 DYNAMIC ANALYSIS OF A CANTILEVER WALL

The investigations of dynamic performance of the proposed (S)GCMQ element depart from a simple cantilever beam/wall example with an aspect ratio of 4. The model is depicted in

Fig. 6.15. Instead of point mass, distributed mass is used with the consistent mass formulation.

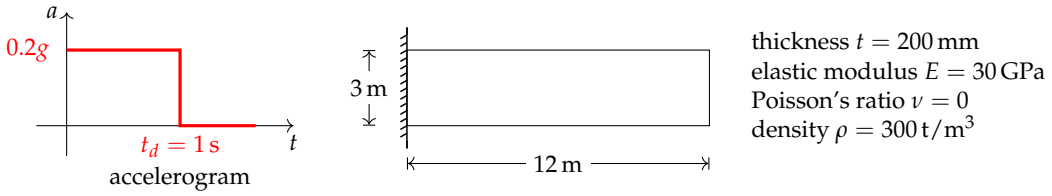


**FIGURE 6.15.** a simple cantilever beam example

The density is set to $300\,\mathrm{t/m^3}$ so that the analytical solution of the first natural frequency $f_1$ (Young, 2012) can be approximated by

$$f_1 \approx \frac{3.52}{2\pi}\sqrt{\frac{EI}{\rho bhL^4}} = \frac{3.52}{2\pi}\sqrt{\frac{Eh^2}{12\rho L^4}} = 1.065\,\mathrm{Hz}, \tag{6.1}$$

so that the first period is $t_1 = 0.939$ s. The duration of the rectangular pulse $t_d$ is set to 1 s. Since the chosen $t_d$ is close to $t_1$, the amplitude of displacement in the free vibration phase is significantly smaller than that of the forced vibration phase. Discussions on the theoretical solutions can be found elsewhere (Chopra, 2011). This feature can be used to amplify the difference among numerical models. The constant average acceleration Newmark method is used for the time integration. The time step size $\Delta t$ is set to 0.01 s. To avoid any potential bias due to different damping models, no damping is defined so an undamped beam is analysed.

### 6.6.1 Eigenanalysis

The eigenanalysis is performed to compute the first natural period. Numerical results, which are obtained by using SGCMQG elements and consistent mass formulation, are shown in Table 6.3. The reference solution is computed by using 3600 CPS4 elements with lumped mass

**TABLE 6.3.** the first natural period computed by using different meshes

| mesh | $1\times1$ | $1\times2$ | $1\times4$ | $2\times4$ | $2\times8$ | ref. |
|---|---|---|---|---|---|---|
| $\omega_1^2$ | 37.44 | 43.23 | 42.28 | 41.70 | 41.41 | 41.37 |
| $t_1$ | 1.03 | 0.96 | 0.97 | 0.97 | 0.98 | 0.98 |

formulation, which is the default configuration in ABAQUS. The results are not significantly affected by different integration schemes. Both consistent and lumped mass matrix formulations give similar results. It could be seen that relatively accurate natural periods, especially that of lower modes, can be obtained by using only a few elements.

From an algorithmic perspective, the excellent coarse mesh accuracy shown by (S)GCMQ is also advantageous to dynamics problems of structures. It is possible to use a very coarse mesh of (S)GCMQ to represent the stiffness of the target structure. By such, the highest frequency of the finite element model is lowered as the total number of DoFs is reduced. The potential fictitious response contributed by high frequency modes can be effectively eliminated from the source. This gives more flexibility when it comes to choose a proper time integration algorithm. The algorithmic damping and the second order accuracy cannot coexist in the well known Newmark method. To obtain the algorithmic damping, analysts shall either give up the second order accuracy or switch to another algorithm such as the generalised alpha method (Chung and Hulbert, 1993). With the high coarse mesh accuracy, it is possible to obtain satisfactory results by using the undamped time integration methods.

### 6.6.2 Linear Analysis

The linear analyses are performed with four mesh grids respectively: $1 \times 1$, $1 \times 2$, $1 \times 4$ and $2 \times 8$. The tip displacement histories are shown in Fig. 6.16. All versions of GCMQ, including

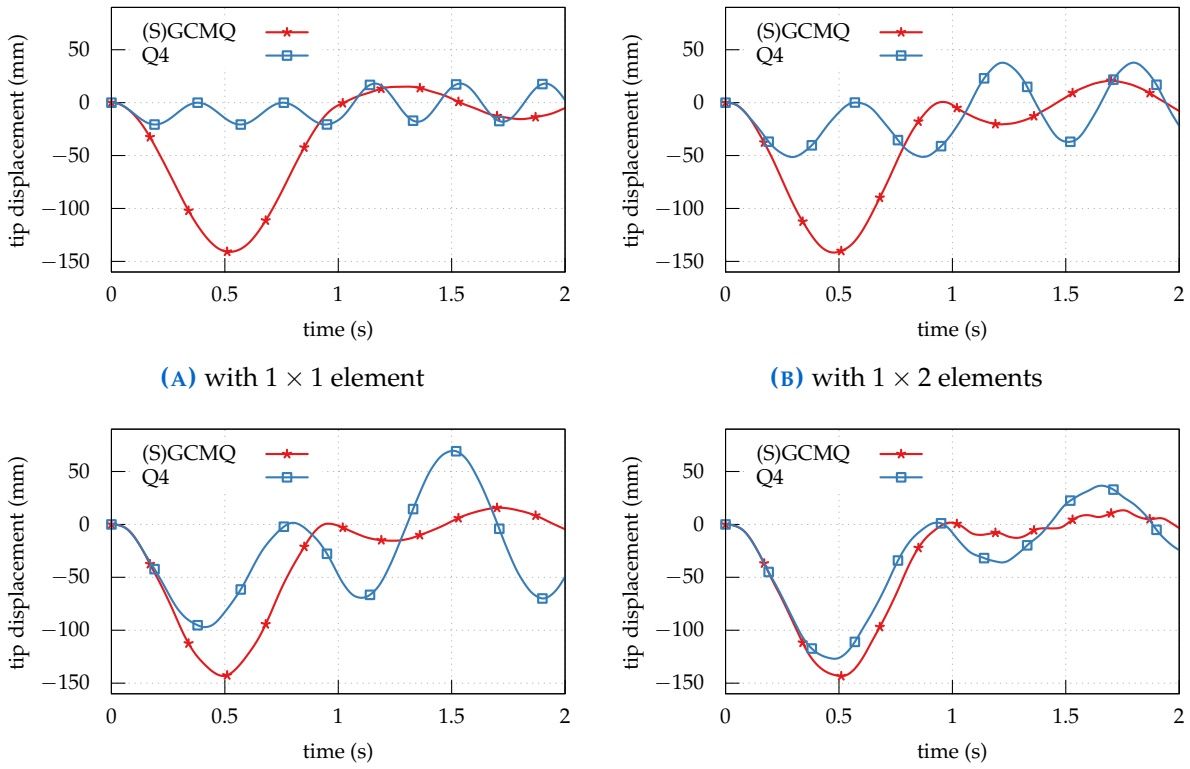


(A) with $1 \times 1$ element

(B) with $1 \times 2$ elements

(C) with $1 \times 4$ elements

(D) with $2 \times 8$ elements

FIGURE 6.16. linear dynamic analysis of the undamped cantilever beam subjected to a rectangular pulse

GCMQI, GCMQL, GCMQG, SGCMQI, SGCMQL and SGCMQG, show little difference in each case, so only one record, denoted as (S)GCMQ, is shown for the sake of clearness.

Due to the overstiff nature, models with Q4 elements show shorter periods and smaller maximum tip displacements compared to models with (S)GCMQ elements. With mesh refinements, less stiff response can be recovered by Q4 elements. However, even with a $2 \times 8$ mesh, the computed first mode period is still smaller than that of (S)GCMQ elements, which indicates that the numerical model is still too stiff. It can be predicted that a much denser mesh is required for Q4 elements to produce an equivalently accurate response. However, the difference among models with (S)GCMQ elements does not vary much. In particular, even with only one element defined, the error of response in forced vibration phase is not significant. (S)GCMQ is able to perform well in terms of linear dynamic analysis with the most coarse meshes.

Meanwhile, given the fact that different numerical integration schemes have no significant impact on the predicted linear displacement history, the simplified GCMQ with the five-point integration scheme (SGCMQI) element appears to be a better option as the computational cost of which is minimized.

### 6.6.3 Nonlinear Analysis

To avoid any mesh objectivity issues, here a linear isotropic hardening von Mises material is used for the non-linear analysis. The yielding stress is chosen to be 80 MPa as the maximum stress observed in the previous linear analysis is about 100 MPa.

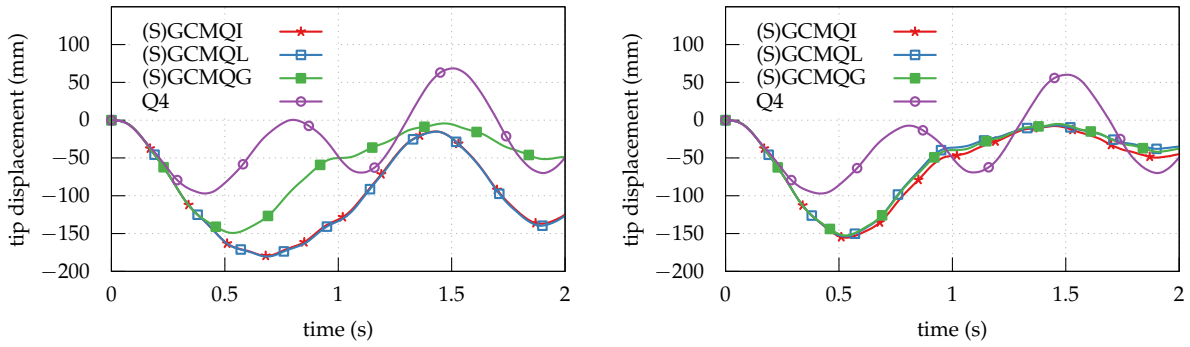


(A) with $1 \times 4$ elements (B) with $2 \times 4$ elements

FIGURE 6.17. non-linear dynamic analysis of the undamped cantilever beam subjected to a rectangular pulse

The displacement histories are shown in Fig. 6.17. With only one element assigned along wall width (beam depth), (S)GCMQI and (S)GCMQL tend to overestimate the development of

plasticity. This can be properly justified since except for the central one, all other integration points are located on element boundaries in the Irons and Lobatto quadratures. This problem can be largely alleviated by simply defining one more element transversely. As can be seen in Fig. 6.17b, all three different integration schemes show no significant difference with such meshes. In contrast, (S)GCMQG shows reasonably accurate response with coarse mesh grids. It is noted that with the Gauss scheme, the maximum stress, which often occurs on element boundaries, cannot be captured by any integration points. Based on the results of this particular example, it appears that (S)GCMQG, compared to the other versions, shall be used with extremely coarse meshes for more reliable results. Meanwhile, by the construction of (S)GCMQ, mesh refinements always result in more accurate response. However, such an improvement may not be necessary considering the coarse mesh performance of (S)GCMQ.

## 6.7 DYNAMIC ANALYSIS OF A RC SHEAR WALL

A reinforced concrete cantilever shear wall specimen shown in Fig. 6.18 with an aspect ratio of 5 is analysed. The specimen is lightly reinforced. As an illustrative example, the reinforcement is modelled in a uniform, smeared approach and may not represent real engineering practice. The total seismic mass is 100 t.

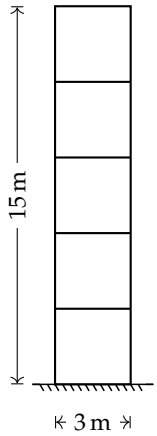


horizontal mass: $m = 20\,\text{t}$ per floor
thickness: $t = 200\,\text{mm}$
concrete elastic modulus: $E_c = 30\,\text{GPa}$
concrete compression strength: $f_c = 30\,\text{MPa}$
concrete tension strength: $f_t = 3\,\text{MPa}$
steel elastic modulus: $E_s = 200\,\text{GPa}$
steel yield strength: $f_y = 300\,\text{MPa}$
steel hardening ratio: $h = 0.02$
smeared reinforcement ratio: 0.5 %
finite element mesh: $2 \times 10$ (width×height)

**FIGURE 6.18.** a reinforced concrete shear wall specimen

A global Rayleigh damping (5 % on the first two modes) is applied. The damping matrix is **deliberately** chosen to be a constant matrix that is proportional to mass and initial stiffness matrices to avoid any potential bias brought by the damping matrix. Such a definition is known to be problematic (Carr, 1997; Chopra and McKenna, 2015), better alternatives are available.

The ground motion used is the NS component of the El Centro record, the PGA of which is $0.349g$. The Newmark method with a constant average acceleration formulation is selected for time integration. The concrete material model used is the CDP model while the Menegotto-Pinto steel model (Menegotto and Pinto, 1973) is used for reinforcement.

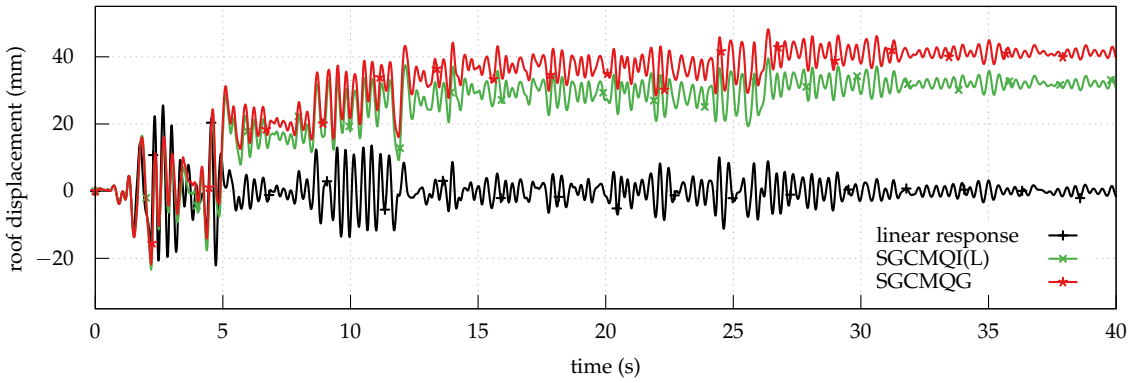


**FIGURE 6.19.** displacement history of a reinforced concrete shear wall

The computed first eigenvalue of the corresponding generalised eigenvalue problem is 351.67, which yields the first natural period to be $T_1 \approx 0.34\,\text{s}$. Fig. 6.19 shows the displacement histories. The difference between linear and non-linear responses starts at $t \approx 2.2\,\text{s}$. The major plastic deformation occurs at $t \approx 4.9\,\text{s}$.

Fig. 6.20 shows the evolution of tensile damage index $\kappa_t$ at both the left and right corners of wall foot. As in this example, the non-linear response is mainly contributed by concrete tensile failure localised on the first floor, the characteristics of the plasticity development observed from the displacement history can also be seen in Fig. 6.20.

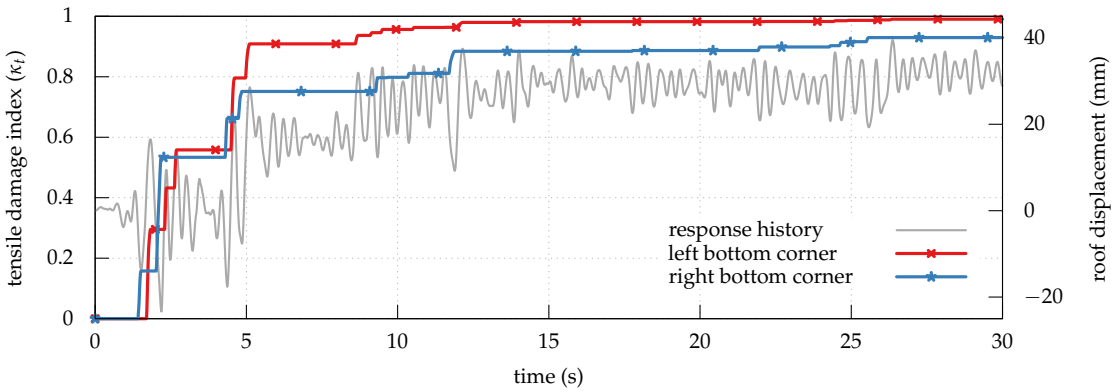


**FIGURE 6.20.** evolution of tensile damage index $\kappa_t$ at left and right corners

It could be again seen in Fig. 6.19 that due to the development of plasticity, different arrangements of interpolation/sampling points lead to different global responses. This discrep-

ancy varies according to the degree of material nonlinearity. In this particular example, such a difference vanishes if an elastic material model is used for reinforcement, in which case the non-linear response purely stems from the concrete material model.

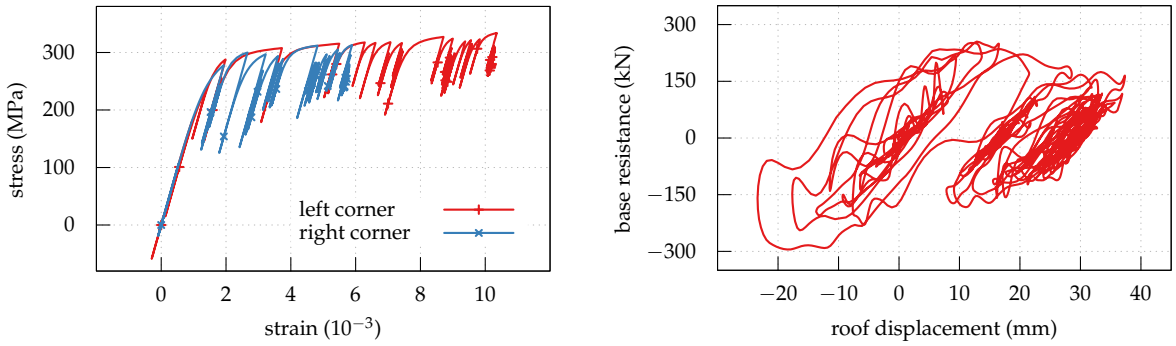


**(A)** reinforcement response **(B)** shear hysteresis

**FIGURE 6.21.** responses of reinforced concrete shear wall

Fig. 6.21a shows the material responses of reinforcement in two extreme integration points. Since the left corner has a higher value of tensile damage index $\kappa_t$, the maximum strain is accordingly larger than that of the right corner. The final strain in the right corner is observed to be positive, meaning that the wall specimen is uplifted. The concrete model can be modified to refine the corresponding response. It shall be noted that the ratcheting effect could exist in the adopted model for reinforcement, with other models, different responses may be obtained.

The base shear resistance is plotted in Fig. 6.21b. Strong non-linear response is observed. The simple multilinear hysteresis models cannot simulate wall structures in which higher modes may have considerable contributions. The maximum shear resistance is about 295 kN.

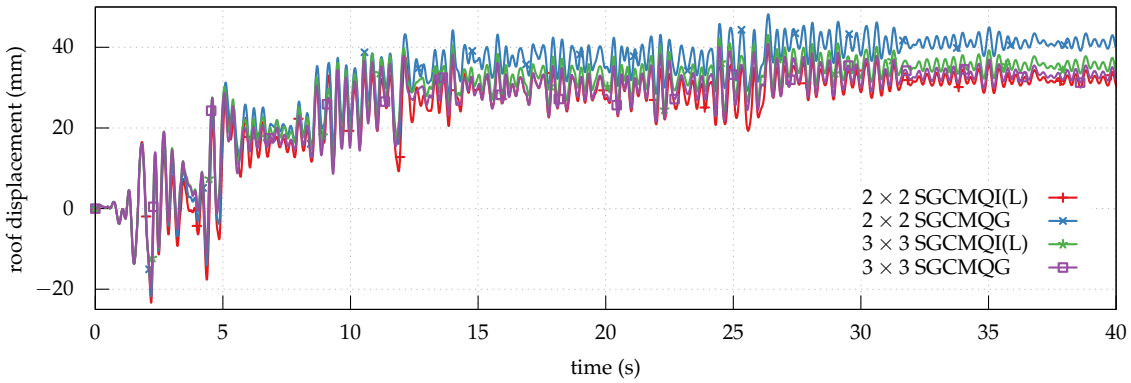


**FIGURE 6.22.** displacement histories with different meshes

Complete mesh objective results are difficult to obtain in dynamic analyses since the response tends to be sensitive to the initial development of plasticity, which is amplified due to the presence of damping and inertial terms. Nevertheless, close results can still be obtained.

Fig. 6.22 shows the displacement histories with $2 \times 2$ and $3 \times 3$ meshes. The corresponding material properties are strictly scaled according to the characteristic lengths of elements. It could be seen that the difference between two types of meshes is insignificant, considering the tensile damage index is approaching unity as shown in Fig. 6.20. For cases with moderate nonlinearity, such a difference would be smaller, resulting in a higher coarse mesh accuracy.

## 6.8 DYNAMIC ANALYSIS OF A RC COUPLED SHEAR WALL

The presence of drilling degrees of freedom offers great convenience to model the connections between wall panels and adjacent beam-type members. This is advantageous when it comes to simulate wall-frame structures and coupled walls. The conventional concept of rotation is derived based on the 'plane sections remain plane' assumption, thus the beam theory. It is in general difficult to define the so called rotation field in a 2D continuum when deformation gradient has similar magnitudes along two axes. Before performing simulations of reinforced concrete structural walls, the performance of drilling DoFs are firstly examined.

### 6.8.1 Numerical Experiment

The model shown in Fig. 6.23 is analysed. A slender beam of size $2 \times 10$ is attached to a square panel of size $10 \times 10$. A uniform thickness of unity is used for both panel and beam.

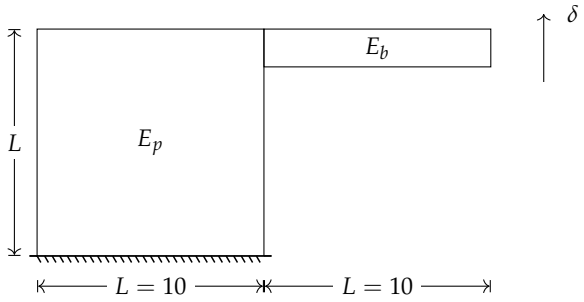


FIGURE 6.23. wall example with attached beam

Although it may not be closely related, the ratio between moments of inertia is $I_p / I_b = 125$, which is kept unchanged throughout different cases. The beam and panel may have different elastic moduli to represent different stiffness ratios between panel and beam. The panel is fully fixed at the base and a unit vertical displacement is applied to the free end of the beam, the corresponding reaction forces is recorded. This structure can be modelled by using membrane

(for panel) and beam (for beam) elements. Alternatively, membrane elements can be used to represent both panel and beam.

In the beam-panel model, the panel is modelled by (S)GCMQ elements while the attached beam is idealised as elastic beam element. The Poisson's ratio is set to zero so the deflection of beam is accurate. Two different meshes are tested: $2 \times 2$ and $4 \times 4$. The corresponding results are shown in Fig. 6.24. The reference values are given by 2D models with refined meshes of plane stress elements in ABAQUS. It could be seen from Fig. 6.24 that the drilling DoFs in (S)GCMQ perform well with weak coupling members. For $E_b/E_p \leqslant 1$, the error can be bounded within 20 % and becomes insignificant when $E_b/E_p \leqslant 0.1$ with the $2 \times 2$ mesh. It is worth mentioning that $E_b/E_p = 125$ leads to the same $EI$ for both panel and beam. However, different mesh densities show different behaviour. A refined mesh does not necessarily lead to more accurate results. With the $4 \times 4$ mesh, the results deteriorates quickly with an increasing moduli ratio $E_b/E_p$. It shall be noted that with the $2 \times 2$ mesh the beam depth is 40 % of the length of the adjacent panel element while this value increases to 80 % with the $4 \times 4$ mesh. Such a high ratio means the physical boundary condition **cannot** be precisely represented by the numerical model. Deformation compatibility may become a severe problem as different elements adopt different displacement interpolations.

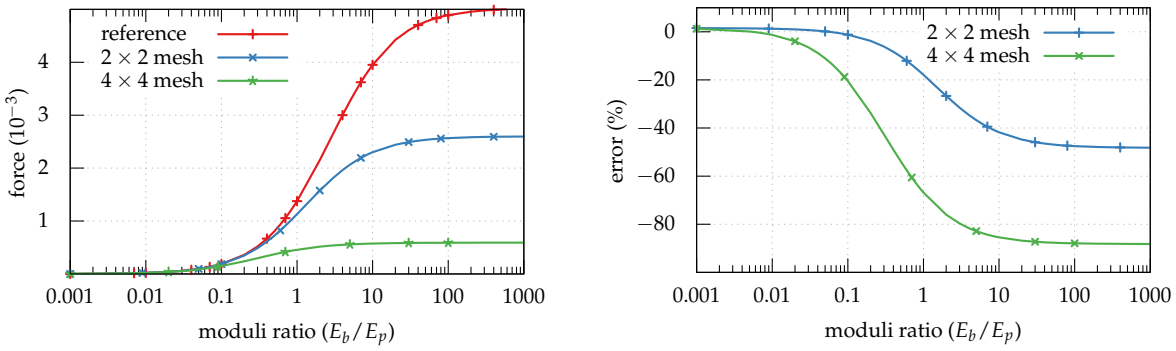


**(A)** end force required **(B)** corresponding error

**FIGURE 6.24.** results of panel with attached beam with different moduli ratios

It is thus **inappropriate** to model this type of connections by using membrane and beam elements. It can be inferred that the error of rotational constraint would be lowered with shallower beams. The response of strong coupling members is hence not well captured by the current definition of drilling DoFs. Indeed, for rigid beams, deformation mainly occurs in the wall panel, where the rotational constraint may be contributed to by a number of adjacent wall elements.

In the author's opinion, it is **not recommended** to simulate walls with opening and/or strong coupling members such as deep beams by using hybrid models that consist of membrane elements — not only (S)GCMQ but also other elements — and beam elements. The focus of the remaining of this section is limited to coupled walls with weak coupling beams/slabs.

### 6.8.2 Reinforced Concrete Coupled Wall

Two reinforced concrete shear walls shown in § 6.7 connected with each other by beams are used to form a coupled wall with a spacing of 3 m. The illustration of the coupled wall, along with the beam section, is depicted in Fig. 6.25. The thickness of concrete cover is assumed to

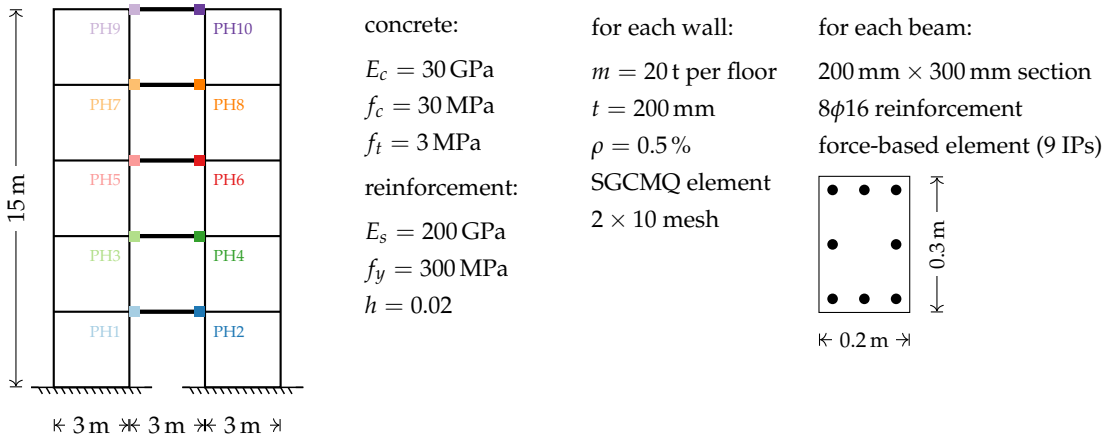


**FIGURE 6.25.** a reinforced concrete shear wall specimen

be 30 mm. The force-based beam element (Spacone et al., 1996) is adopted to model beams since its accuracy mainly relies on the number of integration points (Neuenhofer and Filippou, 1997) so coarse meshes can also be utilised. For beam sections, the backbones used in § 5.4 are adopted as the uniaxial concrete model while the Menegotto-Pinto steel model is used for reinforcement. The configuration of numerical algorithm is identical to that in § 6.7. The first natural period computed is around 0.32 s. The same NS component of El Centro record is used as ground motion.

For the configuration listed, the elastic analysis reveals that the response of the hybrid model (with SGCMQ and beam elements) is close to that of the model with plane stress elements. The difference varies depending on the mesh size but is within 10 %. It is thus reasonable to use the hybrid model to perform the corresponding non-linear analyses.

Fig. 6.26 shows the corresponding displacement histories with three integration schemes.

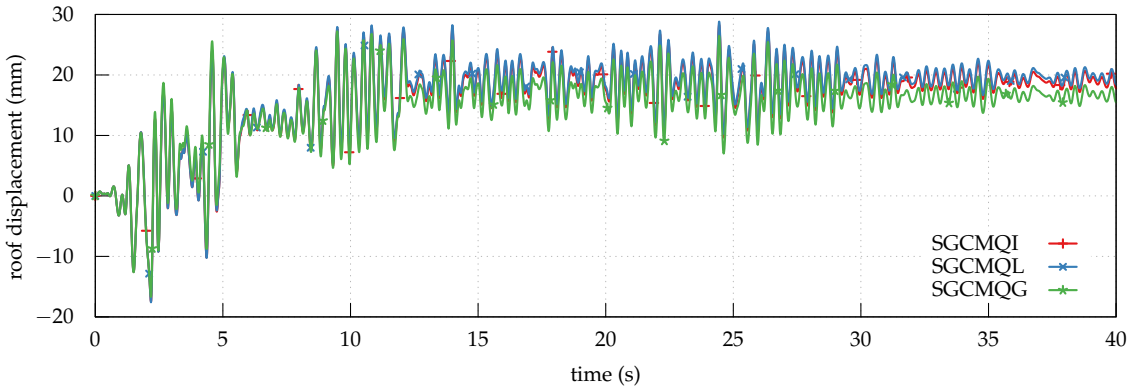


**FIGURE 6.26.** displacement history of coupled wall

The difference between SGCMQG and the other two versions is not as significant as in Fig. 6.19. However, in this example SGCMQG gives slightly more stiff results. It could be inferred that the performance difference between SGCMQG and SGCMQI/SGCMQL would vary from one specific model to another. It is in general difficult to conclude which version is better in terms of accuracy. The overall shapes of roof displacement histories shown in Fig. 6.19 and Fig. 6.26 resemble each other. Due to the presence of coupling beams, the magnitude of displacement is lowered in the first five seconds. The major difference occurs between 5 s and 10 s, which further leads to different residual displacements.

Fig. 6.27 shows the axial force histories of both walls. Nonzero residual axial forces are observed to balance the overturning moment caused by horizontal inertial forces while the summation of which eventually stays at zero.

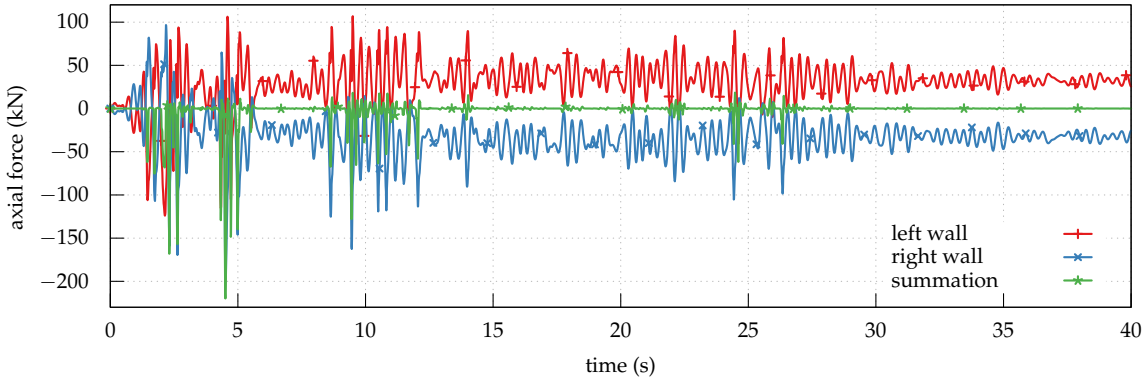


**FIGURE 6.27.** axial force history of coupled wall

Fig. 6.28 shows the evolution of $\kappa_t$ in both walls. Both walls have close $\kappa_t$ values at the same locations. With all material properties unmodified, the coupling effect lowers the maximum tensile damage index $\kappa_t$ from 0.99 in Fig. 6.19 to 0.88 in Fig. 6.28.

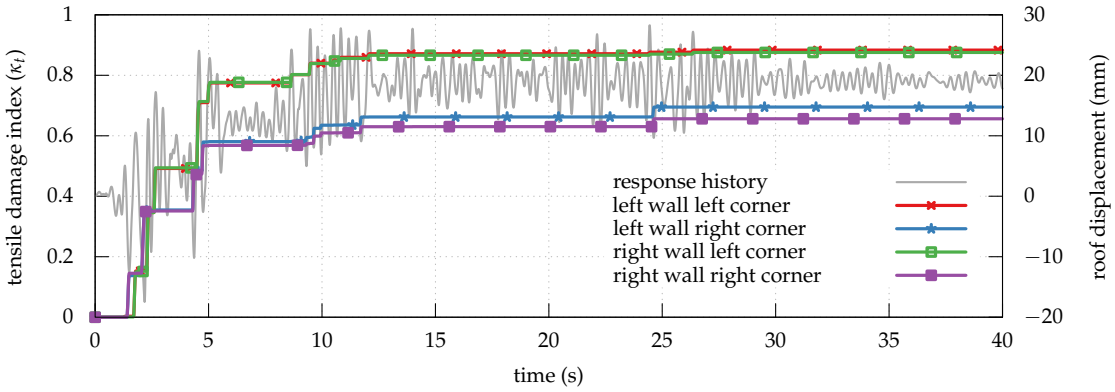


**FIGURE 6.28.** tensile damage index $\kappa_t$ history of coupled wall

Plastic hinges are also developed in coupling beams. Fig. 6.29 shows the hysteresis behaviour of selected beam ends. The upper three floors show similar responses while the first two give different hysteresis loops. The bilinear unloading/reloading rule, which may not be valid for some engineering applications, can be observed.

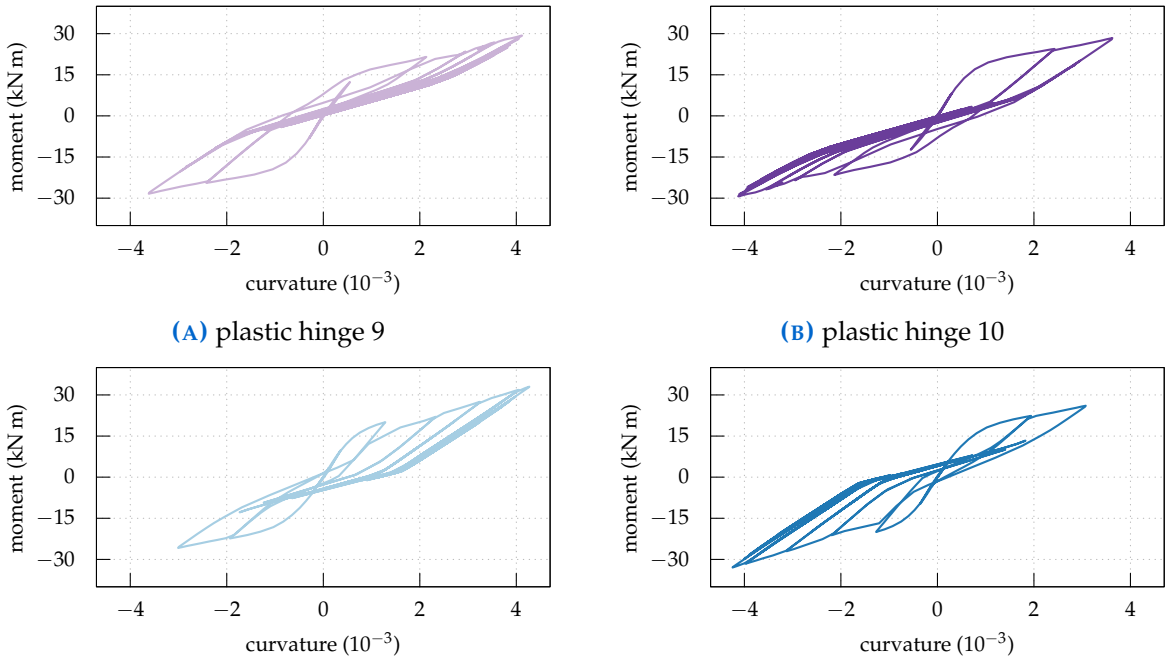


**(A)** plastic hinge 9

**(B)** plastic hinge 10

**(C)** plastic hinge 1

**(D)** plastic hinge 2

**FIGURE 6.29.** responses of plastic hinges located at both ends of coupling beams

Since the adopted beam element does not account for shear response on beam cross sections, the corresponding shear failure mechanisms cannot be captured. In fact, modelling shear failure patterns of coupling beams is similar to simulating walls in which shear effects cannot be ignored. Beam elements may not be suitable for this type of problems.

The presence of drilling DoFs provides the ability to model wall-beam connections in a

natural approach. Other workarounds also exist to address this problem, such as using rigid offset bars and extending beam elements into wall panels. However, those methods either underestimate or overestimate the constraint ability provied by wall panels. Before a clear and precise definition of rotation field for 2D panels, it is difficult to argue which method is more advantageous. Nevertheless, (S)GCMQ offers an alternative to approach the problem. As can be seen in the numerical experiment, the accuracy can be guaranteed if the coupling effect is weak. Drilling DoFs are also appealing to geotechnical engineers when it comes to model pile problems in which piles are often modelled by beam elements. Retaining walls could be also modelled by (S)GCMQ.

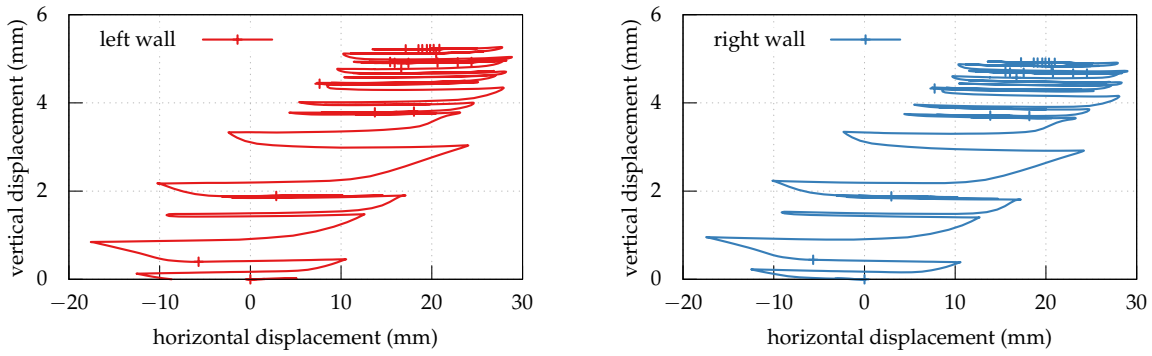


(A) left wall (B) right wall

**FIGURE 6.30.** elongation of the coupled wall under seismic excitation

Finally the elongation of two walls are shown in Fig. 6.30. Since there is no axial load applied, two walls behave in a similar manner. The left wall reaches a larger vertical elongation than that of the right wall. This is consistent with the axial load distribution as shown earlier in Fig. 6.27. The difference would be greater if the coupled wall is axially loaded.

# 7

# Conclusions

Summaries and conclusions are presented in this chapter. Beyond the (S)GCMQ element itself, a few other things regarding modelling of shear walls are discussed. For future work, the author believes that a more enriched element can be developed atop (S)GCMQ, including but not limited to a more complex reinforcement representation, coupling between in-plane and out-of-plane actions, etc.

## 7.1 Summaries

In this work,

1. A four-node quadrilateral membrane element with drilling degrees of freedom named as GCMQ is proposed based on a modified Hu-Washizu variational principle with an additional enhanced strain field.
2. A simplified version of GCMQ with the enhanced strain field omitted, named as SGCMQ, is proposed for better numerical efficiency.
3. A five-point integration scheme is proposed based on Irons' six-point scheme to minimise the computational cost.

The proposed (S)GCMQ element combines the advantages of both the mixed formulation and the generalised conforming method and further optimize the interpolations of stress and strain fields. Up to three enhanced strain modes are supported by the formulation. In the

proposed elements, GCMQ adopts one enhanced mode while SGCMQ excludes the enhanced mode. Alternatives of enhanced strain modes are possible. Elastic validations of the proposed (S)GCMQ element have been performed with emphases on convergence, mesh distortion sensitivity, shear locking, volumetric locking and coarse mesh accuracy. Since strain rate is not involved in the formulation, it could be expected that the proposed element is locking free under transient loading as well. The objectives are mostly fulfilled, (S)GCMQ has the following features.

1. free from volumetric locking,
2. good bending performance,
3. no locking in thin elements,
4. low sensitivity to mesh distortions,
5. good coarse mesh accuracy,
6. simple implementation for non-linear constitutive equations and,
7. minimised computational cost.

In the meantime, (S)GCMQ exhibits high coarse mesh accuracy that can be utilised in both elastic and elasto-plastic applications. Since (S)GCMQ is a general purpose planar element, it can be used to model not only reinforced concrete shear walls but also other 2D problems. The finite element analysis is more efficient with (S)GCMQ since the number of DoFs required to achieve the same level of accuracy can be significantly reduced.

Due to the presence of drilling DoFs, (S)GCMQ can be used with other types of elements without additional treatments. This feature can be utilised to simplify the pre-precessing procedure of some special applications such as the simulation of wall-frame structures in civil engineering. The drilling DoFs are also advantageous when it comes to forming a planar shell element by combing (S)GCMQ with other plate elements. The corresponding stiffness matrix would be properly ranked, no other numerical considerations are required.

## 7.2 DISCOVERIES

A series of applications of the proposed (S)GCMQ with non-linear material models subjected to static, including both monotonic and cyclic, and dynamic loading is also performed to model squat/short and slender shear walls, as well as weakly coupled shear walls. Various

mesh configurations are examined. Several discoveries can be concluded as follows.

1. Convergence is guaranteed for (S)GCMQ with different integration schemes. If dense meshes are used, the five-point adapted Irons quadrature is preferable due to its minimised numerical cost.
2. For most examples shown in this dissertation, there is no significant difference observed from the results of (S)GCMQI and (S)GCMQL. Since displacement, strain and stress are interpolated internally, the additional four integration points used in (S)GCMQL do not lead to any improvement of performance. In this sense, (S)GCMQL is not recommended unless some other material properties are of interest.
3. The proposed (S)GCMQ element has a lower initial error bound, which is advantageous in terms of elastic applications.
4. The performance of drilling degrees of freedom is reliable **only** when the wall-panel connection is properly sized. It is thus recommended to model weak coupling effects by using membranes and beams while for strong coupling members complete 2D models with plane stress elements shall be employed.
5. The performance of (S)GCMQI/(S)GCMQL differs from that of (S)GCMQG due to the different arrangements of integration points. It is a common phenomenon and hard to determine which one is consistently better than the others. It is thus the analysts' choice to decide which version to use.
6. (S)GCMQ element is able to produce more accurate eigenvalues, viz., natural periods of structures, with fewer elements. This is advantageous when it comes to eigenanalyses of structures. In terms of mass formulation, no significant difference is observed among different formulations for lower modes. However, it is recommended to use full ranked mass matrices to accommodate some conditionally stable time integration algorithms.
7. The overall performance of numerical simulations relies on not only elements but also material models. It could be seen that objective results can only be obtained by using material models that support regularisation. In other words,

$$\text{High-performing Element} + \text{Objective Material} = \text{Good Overall Accuracy}.$$

Apart from the sensitivity to severe mesh distortion, it is worth noting that there may exist a stability issue when the enhanced strain is present. The problem can only be observed

with **certain** non-linear material models. It may be relevant to the bifurcation problem of coupled damage plasticity material models or the common issue with enhanced strain elements as discussed by Wriggers and Reese (1996). Numerical experiments reveal that the global convergence rate would be greatly affected even with the presence of consistent tangent stiffness. However, convergence can still be achieved and the solution can be computed. In specific, the problem appears with GCMQ (no matter how many enhanced strain modes are used) and the CDP model presented in § 5.3. All other material models used in this work do not exhibit unstable performance. Based on these facts, GCMQ is recommended for linear analysis while SGCMQ is recommended for non-linear analysis.

## 7.3 BEYOND THE ELEMENT ITSELF

Beyond the technical details of the proposed (S)GCMQ element, there are a few other problems with regard to the finite element analysis of reinforced concrete shear walls. This section is aimed to present a brief discussion of some key ones. Hopefully the numerical simulations of shear walls would be less complex and less painful in future.

### 7.3.1 1D, 2D or 3D?

Different elements with different formulations could work well in different scenarios. However, accounting for error of numerical methods and computational efficiency, for general purpose practice, the author believes that it is preferable to use 2D elements with 2D/3D materials to model walls for the following reasons.

1. From first principles, modelling in-plane behaviour of shear walls is a 2D problem and naturally it shall be addressed by using 2D tools.
2. All procedures of simplification from 2D to 1D domain adopt additional assumptions at the cost of sacrificing certain information of panel behaviour. Hence 1D models may work well in modelling slender walls that are dominated by uniaxial behaviour. For anything beyond that, 2D elements should be used.
3. Analysts are not recommended to use any 3D solid/brick elements, including both lower-order and higher-order elements, to model panels due to their extremely low efficiency and performance, let alone the disproportionate demand on memory usage.

4. Similar to how bar buckling is treated by Dhakal and Maekawa (2002), out-of-plane behaviour of walls can also be accounted for as material response so that the computational cost can be minimised. Geometry nonlinearity analysis could be more precise but it is not practical for simulations of large scale structures due to its cost. In this sense, a planar element is preferred with a proper material model that has built-in degradation for out-of-plane buckling.

### 7.3.2 How Reliable Is (S)GCMQ?

Reliability is a great concern for all finite elements. There are debates over the reliability, as well as other attributes such as the robustness, of different modelling approaches (see Palermo and Vecchio, 2007). In the author's opinion, all 1D idealizations, which are adopted by most macroscopic elements, are not suitable for simulations of shear walls due to the presences of various assumptions which do not always hold for all types of walls. As can be seen earlier, the error of those elements is not bounded within a certain range and convergence to analytical solution is not achievable. In this sense, existing macroscopic elements are **unreliable**. A 2D problem should be solved by using 2D tools.

The proposed (S)GCMQ is developed based on the theory of continuum mechanics. By construction, convergence is guaranteed. Hence, mesh refinement can always reduce the magnitude of error. Since (S)GCMQ has a good coarse mesh accuracy, the initial numerical error can be bounded within a narrow range. If the adopted material model is reliable, the overall reliability is not an issue for (S)GCMQ.

### 7.3.3 What Material Model Shall Be Used?

To model in-plane concrete behaviour, for numerical models with coarse mesh grids, the so called fixed/discrete crack formulation (for concrete) loses its meaning as the fixed crack angle itself is an averaged representation of cracking effect around a relatively large region. Meanwhile, it is in general difficult to define a proper behaviour for shear response as most models treat normal and shear responses separately. The smeared approach and the damage based formulations appear to be better options.

To the best of the author's knowledge, to date, there is still a lack of good in-plane concrete

material models that can simulate both the development of failure envelop and the hysteresis behaviour. Multiaxial models that are formulated based on plasticity and/or damage theories could provide flexible definitions of yield surface and its development. The CDP model used in the previous chapter is a 3D model and thus requires iterations to produce plane stress response (with a conventional static condensation algorithm). Alternatively, a non-iterative algorithm can be applied (see, e.g., Klinkel and Govindjee, 2002). Meanwhile, since an isotropic damage model is adopted, the unloading/reloading (hysteresis) response is not ideal. As a more efficient alternative, the fixed angle theory is essentially based on uniaxial response. Due to this, the post-yielding behaviour, as well as the development of yielding surface, is a tough issue. Hence, an efficient in-plane concrete model developed based on the corresponding plasticity/damage theory is on demand. With such a material model, simulations of concrete walls would be easier in the future.

### 7.3.4 Is Efficiency a Problem?

People may argue that finite elements, particularly mixed ones, are less computationally efficient. Indeed, for element-wise state updating, finite elements do require more computation effort. However, it is clear that the finite element analysis time is not proportional to the number of DoFs and most time is spent on solving global system instead of updating element states. Thus, element-wise performance is less concerning, especially in a parallel framework that is capable of updating several element states at the same time. For the same level of accuracy with the same amount of DoFs, (S)GCMQ is not necessarily slower than other elements. In fact, it can be shown that GCMQ is faster than the serendipity Q8 element. Furthermore, the simplified version SGCMQ does not require element level matrix operation and has an efficiency similar to that of Q8 element with reduced integration (CPS8R element in ABAQUS notation). The state determination of which fully resembles that of conventional displacement based elements.

### 7.3.5 Which Stress Field Should Be Used?

Unlike displacement and strain fields, in (S)GCMQ, there are two stress fields, one is the interpolated stress field within each element domain, the other one is the stress provided by the material model at each integration point. There is no difference between those two fields in elastic cases. However, for elasto-plastic applications, they may differ and the difference could

be significant. This rises a problem: which one should analysts use?

Clearly, as can be seen in Fig. 4.13, the difference between adjacent stress fields diminishes with refined mesh grids. The problem then becomes whether the interpolated stress field is reliable with a coarse mesh grid. In fact, the interpolated stress field can be deemed as an energetic equivalence of the material stress field. In this sense, the interpolated stress field is simply one implementation of many stress averaging methods. If the inter-element continuity is a must, the interpolated stress field can be further averaged.

If post-processing is performed separately, it is likely to average the stress field over the whole model. Depending on the specific method used, the interpolated stress field may or may not be useful. It is possible to obtained nodal stress values directly from the interpolated stress field. Nodal stresses can be averaged in a weighed approach based on how many elements are connected to the target node.

In the author's opinion, unless an interpolated stress field that possesses inter-element continuity is available, there is no difference to use any of the two stress fields, given that the raw data generated will not be directly used in the interpretation of simulation results. However, if section resultants are required, the interpolated stress field shall be used as it is closer to the true stress field from the perspective of energy.

## 7.4 WHAT'S NEXT?

The formulation of the (S)GCMQ element presented in § 3.2 is based on an additive decomposition of infinitesimal deformation. The distortion $\boldsymbol{u}_d$ can be directly constructed on the translated configuration $\boldsymbol{x}_m$. Hence, a finite deformation formulation can be further developed by keeping the second order term $\nabla \boldsymbol{u}_d \cdot \boldsymbol{u}_t$. Although finite deformation may not be critical for structural walls in civil engineering, it could be useful in other applications.

For simplicity, only one enhanced mode is adopted in GCMQ while the formulation supports at most three modes. A more extensive study of different enhanced modes can be performed in order to seek potentially better modes that can further improve the coarse mesh accuracy of GCMQ.

It could been seen that the proposed (S)GCMQ element shows a very good performance among existing four-node quadrilateral membrane elements. Though, for 3D applications with

arbitrary planar geometries, a shell element is in demand. SGCMQ can be readily combined with other plate elements to form high performing shell elements. Since the plate theory has been extensively investigated by researchers to date, there are a lot of very good four-node plate elements in current literature. Successful ones, such as DKT element family (Batoz et al., 1980), can be directly borrowed.

It can also be concluded from numerical examples that the adopted definition of drilling degrees of freedom is not perfect. It works well when the distortion is not great compared to the translational deformation. However, in the current context, there is still a lack of theoretical basis for discussions of the 'precision' of the drilling DoFs. As aforementioned in Chapter 3, ideally there shall be two drilling DoFs per node to control the distortion of two connected edges respectively. It is thus possible to develop a series of different types of elements with four DoFs per node to form a new finite element system, which may help to improve the numerical representation of realistic deformation field.

As discussed previously, apart from the element aspect, the development of a good in-plane (or 3D) concrete material model that supports flexible definitions of hysteresis rules and damage evolutions is still challenging. The two-surface plasticity theory (Dafalias, 1986) combined with the damage mechanics would be an appealing potential. However, it is noted the coupled damage plasticity models may have bifurcation problems due to localization, while mixed elements with enhanced strain modes may have stability issues, it is expected to further study the performance of the combination of the proposed element and damage plasticity material models. In terms of modelling reinforced concrete problems, to accommodate more flexible definitions of reinforcement layouts, it is possible to define some built-in patterns of reinforcement that may adopt both discrete and smeared approaches. A laminated membrane/shell element could be constructed atop (S)GCMQ.

# A

# Explicit Form of Drilling Displacement

By assuming the element is anti-clockwise encoded by four nodes labelled from 1 to 4, the global coordinates of which are

$$\begin{bmatrix} x_1 & x_2 & x_3 & x_4 \\ y_1 & y_2 & y_3 & y_4 \end{bmatrix}^{\mathrm{T}}. \tag{A.1}$$

For convenience, the following symbols are used as well.

$$\begin{aligned} &x_{21} = x_2 - x_1, \quad x_{32} = x_3 - x_2, \quad x_{43} = x_4 - x_3, \quad x_{14} = x_1 - x_4, \\ &y_{21} = y_2 - y_1, \quad y_{32} = y_3 - y_2, \quad y_{43} = y_4 - y_3, \quad y_{14} = y_1 - y_4. \end{aligned} \tag{A.2}$$

For a given integration point with parent coordinates $\xi$ and $\eta$, denote

$$\xi_p = \xi + 1, \quad \xi_m = \xi - 1, \quad \eta_p = \eta + 1, \quad \eta_m = \eta - 1, \tag{A.3}$$

so that in Eq. (3.35),

$$\boldsymbol{\phi}_d \boldsymbol{G}^{-1} \boldsymbol{Q} = \frac{1}{16} \begin{bmatrix} x_{21}(1-\xi^2)\eta_m + x_{14}\xi_m(\eta^2-1) & y_{21}(1-\xi^2)\eta_m + y_{14}\xi_m(\eta^2-1) \\ x_{21}(\xi^2-1)\eta_m + x_{32}\xi_p(\eta^2-1) & y_{21}(\xi^2-1)\eta_m + y_{32}\xi_p(\eta^2-1) \\ x_{43}(\xi^2-1)\eta_p + x_{32}\xi_p(1-\eta^2) & y_{43}(\xi^2-1)\eta_p + y_{32}\xi_p(1-\eta^2) \\ x_{43}(1-\xi^2)\eta_p + x_{14}\xi_m(1-\eta^2) & y_{43}(1-\xi^2)\eta_p + y_{14}\xi_m(1-\eta^2) \end{bmatrix}^{\mathrm{T}}. \tag{A.4}$$

The derivatives can be computed accordingly.

# B

# Explicit Eigenvalue Decomposition of a Square GCMQ Element

A unit square element with unit thickness is analysed with a density of 100 and an elastic modulus of 100. The Poisson's ratio is set to 0.2. GCMQG element is used as the reference element. The stiffness $\boldsymbol{K}$ can be explicitly expressed with discrete numbers.

$$K = \begin{bmatrix}
46.38 & 15.63 & -4.46 & -25.55 & -5.21 & 4.46 & -26.54 & -15.63 & -2.48 & 5.70 & 5.21 & 2.48 \\
15.63 & 46.38 & 4.46 & 5.21 & 5.70 & -2.48 & -15.63 & -26.54 & 2.48 & -5.21 & -25.55 & -4.46 \\
-4.46 & 4.46 & 2.68 & 4.46 & 2.48 & -1.44 & 2.48 & -2.48 & 0.20 & -2.48 & -4.46 & -1.44 \\
-25.55 & 5.21 & 4.46 & 46.38 & -15.63 & -4.46 & 5.70 & -5.21 & 2.48 & -26.54 & 15.63 & -2.48 \\
-5.21 & 5.70 & 2.48 & -15.63 & 46.38 & -4.46 & 5.21 & -25.55 & 4.46 & 15.63 & -26.54 & -2.48 \\
4.46 & -2.48 & -1.44 & -4.46 & -4.46 & 2.68 & -2.48 & 4.46 & -1.44 & 2.48 & 2.48 & 0.20 \\
-26.54 & -15.63 & 2.48 & 5.70 & 5.21 & -2.48 & 46.38 & 15.63 & 4.46 & -25.55 & -5.21 & -4.46 \\
-15.63 & -26.54 & -2.48 & -5.21 & -25.55 & 4.46 & 15.63 & 46.38 & -4.46 & 5.21 & 5.70 & 2.48 \\
-2.48 & 2.48 & 0.20 & 2.48 & 4.46 & -1.44 & 4.46 & -4.46 & 2.68 & -4.46 & -2.48 & -1.44 \\
5.70 & -5.21 & -2.48 & -26.54 & 15.63 & 2.48 & -25.55 & 5.21 & -4.46 & 46.38 & -15.63 & 4.46 \\
5.21 & -25.55 & -4.46 & 15.63 & -26.54 & 2.48 & -5.21 & 5.70 & -2.48 & -15.63 & 46.38 & 4.46 \\
2.48 & -4.46 & -1.44 & -2.48 & -2.48 & 0.20 & -4.46 & 2.48 & -1.44 & 4.46 & 4.46 & 2.68
\end{bmatrix}.$$

Eigendecomposition of $\boldsymbol{K}$ gives the following eigenvalues.

$$\lambda = \begin{bmatrix} 0.00 & 0.00 & 0.00 & 0.00 & 1.05 & 2.06 & 2.06 & 40.10 & 40.10 & 83.33 & 88.02 & 125.00 \end{bmatrix}.$$

Clearly, the rank of $\boldsymbol{K}$ equals 8. There are four rigid body modes. Mode 7 and mode 8 have the

same eigenvalue, as well as mode 9 and mode 10. In total, there are 6 different eigen modes. The corresponding eigenvectors are

$$\begin{bmatrix}
1 & 1 & 1 & 1 & 1 & 1 & 1 & 1 \\
-1 & 0 & -13.34 & -2.74 & 0 & 1 & -1 & 1 \\
5.92 & 9.48 & 135.99 & -0.39 & -0.11 & 0 & -0.34 & 0 \\
-1 & -1 & -1 & -1 & -1 & 1 & -1 & -1 \\
-1 & 0 & 13.34 & 2.74 & 0 & -1 & -1 & 1 \\
-5.92 & -9.48 & 117.03 & -0.18 & 0.11 & 0 & 0.34 & 0 \\
-1 & 1 & 1 & 1 & 1 & -1 & -1 & -1 \\
1 & 0 & -13.34 & -2.74 & 0 & -1 & 1 & -1 \\
5.92 & -9.48 & -135.99 & 0.39 & 0.11 & 0 & -0.34 & 0 \\
1 & -1 & -1 & -1 & -1 & -1 & 1 & 1 \\
1 & 0 & 13.34 & 2.74 & 0 & 1 & 1 & -1 \\
-5.92 & 9.48 & -117.03 & 0.18 & -0.11 & 0 & 0.34 & 0
\end{bmatrix}.$$

The corresponding mass matrix $\boldsymbol{M}$ can be seen as

$$M = \begin{bmatrix}
11.11 & & & 5.56 & & & 2.78 & & & 5.56 & & \\
& 11.11 & & & 5.56 & & & 2.78 & & & 5.56 & \\
& & 0.56 & & & -0.14 & & & -0.28 & & & -0.14 \\
5.56 & & & 11.11 & & & 5.56 & & & 2.78 & & \\
& 5.56 & & & 11.11 & & & 5.56 & & & 2.78 & \\
& & -0.14 & & & 0.56 & & & -0.14 & & & -0.28 \\
2.78 & & & 5.56 & & & 11.11 & & & 5.56 & & \\
& 2.78 & & & 5.56 & & & 11.11 & & & 5.56 & \\
& & -0.28 & & & -0.14 & & & 0.56 & & & -0.14 \\
5.56 & & & 2.78 & & & 5.56 & & & 11.11 & & \\
& 5.56 & & & 2.78 & & & 5.56 & & & 11.11 & \\
& & -0.14 & & & -0.28 & & & -0.14 & & & 0.56
\end{bmatrix}.$$

The generalised eigenvalue problem can also be solved. This could be useful when it comes to the formulation of elemental damping.

# References


Allman, D. J. (1984). A compatible triangular element including vertex rotations for plane elasticity analysis, *Computers & Structures* **19**(1-2): 1–8.

Allman, D. J. (1988). A quadrilateral finite element including vertex rotations for plane elasticity analysis, *International Journal for Numerical Methods in Engineering* **26**(3): 717–730.

Ayoub, A. and Filippou, F. C. (1998). Nonlinear finite-element analysis of RC shear panels and walls, *Journal of Structural Engineering* **124**(3): 298–308.

Azzato, F. and Vulcano, A. (1996). Modeling of RC frame-wall structures for nonlinear seismic analysis, *Proceedings of the 11$^{th}$ World Conference on Earthquake Engineering*.

Bailey, C. G. (1995). *Simulation of the Structural Behaviour of Steel-Framed Buildings in Fire*, phdthesis, University of Sheffield.

Bao, Y. and Kunnath, S. K. (2010). Simplified progressive collapse simulation of RC frame-wall structures, *Engineering Structures* **32**(10): 3153–3162.

Barrales, F. R. (2012). *Development of a Nonlinear Quadrilateral Layered Membrane Element with Drilling Degrees of Freedom and a Nonlinear Quadrilateral Thin Flat Layered Shell Element for the Modeling of Reinforced Concrete Walls*, phdthesis, University of Southern California.

Batoz, J.-L., Bathe, K.-J. and Ho, L.-W. (1980). A study of three-node triangular plate bending elements, *International Journal for Numerical Methods in Engineering* **15**(12): 1771–1812.

Bažant, Z. P. and Oh, B. H. (1983). Crack band theory for fracture of concrete, *Matériaux et Constructions* **16**(3): 155–177.

Belmouden, Y. and Lestuzzi, P. (2007). Analytical model for predicting nonlinear reversed cyclic behaviour of reinforced concrete structural walls, *Engineering Structures* **29**(7): 1263–1276.

Belytschko, T., Liu, W. K., Moran, B. and Elkhodary, K. (2014). *Nonlinear Finite Elements for Continua and Structures*, 2nd edn, John Wiley & Sons.

Bergan, P. G. and Felippa, C. A. (1985). A triangular membrane element with rotational degrees of freedom, *Computer Methods in Applied Mechanics and Engineering* **50**(1): 25–69.

Boutagouga, D. (2016). A new enhanced assumed strain quadrilateral membrane element with drilling degree of freedom and modified shape functions, *International Journal for Numerical Methods in Engineering* **110**(6): 573–600.

Carpenter, L. D., Naeim, F., Lew, M., Youssef, N. F., Rojas, F., Saragoni, G. R. and Adaros, M. S. (2010). Performance of tall buildings in viña del mar in the 27 February 2010 offshore maule, Chile earthquake, *The Structural Design of Tall and Special Buildings* **20**(1): 17–36.

Carr, A. J. (1967). *A refined finite element analysis of thin shell structures including dynamic loadings*, phdthesis, University of California at Berkeley.

Carr, A. J. (1997). Damping models for inelasitc analyses, *Asia-Pacific Vibration Conference*, pp. 42–48.

Carr, A. J. (1998). *Ruaumoko: The Maori God of Volcanoes and Earthquakes*, University of Canterbury.

Cen, S., Zhou, M.-J. and Fu, X.-R. (2011). A 4-node hybrid stress-function (HS-F) plane element with drilling degrees of freedom less sensitive to severe mesh distortions, *Computers & Structures* **89**(5-6): 517–528.

Cen, S., Zhou, P.-L., Li, C.-F. and Wu, C.-J. (2015). An unsymmetric 4-node, 8-DOF plane membrane element perfectly breaking through MacNeal's theorem, *International Journal for Numerical Methods in Engineering* **103**(7): 469–500.

Chaboche, J. L. (2008). A review of some plasticity and viscoplasticity constitutive theories, *International Journal of Plasticity* **24**(10): 1642–1693.

Chang, G. A. and Mander, J. B. (1994). Seismic energy based fatigue damage analysis of bridge columns: Part I — evaluation of seismic capacity, *techreport NCEER-94-0006*, State University of New York ar Buffalo.

Chang, T. L., Lee, C.-L., Carr, A. J. and Dhakal, R. P. (2019b). Numerical evaluations of a novel membrane element in simulations of reinforced concrete shear walls, *Engineering Structures* **199**: 109592.

Chang, T. L., Lee, C.-L., Carr, A. J., Dhakal, R. P. and Pampanin, S. (2019a). A new drilling quadrilateral membrane element with high coarse-mesh accuracy using a modified Hu-Washizu principle, *International Journal for Numerical Methods in Engineering* **119**(7): 639–660.

Chen, B., Tan, J. and Oyang, Y. (2011). An improved simulation model of shear wall structures of tall building, *Procedia Engineering* **12**: 127–132.

Chen, S. and Kabeyasawa, T. (2000). Modeling of reinforced concrete shear wall for nonlinear analysis, *Proceedings of the 12$^{th}$ World Conference on Earthquake Engineering*.

Chinosi, C., Comodi, M. I. and Sacchi, G. (1997). A new finite element with 'drilling' D.O.F., *Computer Methods in Applied Mechanics and Engineering* **143**(1-2): 1–11.

Choi, C.-K., Lee, T.-Y. and Chung, K.-Y. (2002). Direct modification for nonconforming elements with drilling DOF, *International Journal for Numerical Methods in Engineering* **55**(12): 1463–1476.

Choi, N., Choo, Y. S. and Lee, B. C. (2006). A hybrid Trefftz plane elasticity element with drilling degrees of freedom, *Computer Methods in Applied Mechanics and Engineering* **195**(33-36): 4095–4105.

Choo, Y. S., Choi, N. and Lee, B. C. (2006). Quadrilateral and triangular plane elements with rotational degrees of freedom based on the hybrid trefftz method, *Finite Elements in Analysis and Design* **42**(11): 1002–1008.

Chopra, A. K. (2011). *Dynamics of Structures*, 4th edn, Pearson.

Chopra, A. K. and McKenna, F. (2015). Modeling viscous damping in nonlinear response history analysis of buildings for earthquake excitation, *Earthquake Engineering & Structural Dynamics* **45**(2): 193–211.

Chung, J. and Hulbert, G. M. (1993). A time integration algorithm for structural dynamics with improved numerical dissipation: The generalized-$\alpha$ method, *Journal of Applied Mechanics* **60**(2): 371.

Colotti, V. (1993). Shear behavior of RC structural walls, *Journal of Structural Engineering* **119**(3): 728–746.

Cook, R. D. (1986). On the allman triangle and a related quadrilateral element, *Computers & Structures* **22**(6): 1065–1067.

Cook, R. D. (1987). A plane hybrid element with rotational D.O.F. and adjustable stiffness, *International Journal for Numerical Methods in Engineering* **24**(8): 1499–1508.

Crisfield, M. A. and Wills, J. (1989). Analysis of R/C panels using different concrete models, *Journal of Engineering Mechanics* **115**(3): 578–597.

Dafalias, Y. F. (1986). Bounding surface plasticity. I: Mathematical foundation and hypoplasticity, *Journal of Engineering Mechanics* **112**(9): 966–987.

Dashti, F., Jalali, A. and Malekpour, S. (2011). Parametric investigations on an RC wall macro model, *Procedia Engineering* **14**: 329–335.

Dhakal, R. P. and Maekawa, K. (2002). Modeling for postyield buckling of reinforcement, *Journal of Structural Engineering* **128**(9): 1139–1147.

Dodd, L. L. and Restrepo-Posada, J. I. (1995). Model for predicting cyclic behavior of reinforcing steel, *Journal of Structural Engineering* **121**(3): 433–445.

Fajman, P. (2002). New triangular plane element with drilling degrees of freedom, *Journal of Engineering Mechanics* **128**(4): 413–418.

Felippa, C. A. (1966). *Refined Finite Element Analysis of Linear and Nonlinear Two–Dimensional Structures*, phdthesis, University of California, Berkeley.

Filippou, F. C., Popov, E. P. and Bertero, V. V. (1983). Effects of bond deterioration on hysteretic behavior of reinforced concrete joints, *techreport UCB/EERC-83/19*, University of California at Berkeley.

Fischinger, M. and Isaković, T. (2000). Benchmark analysis of structural wall, *Proceedings of the 12$^{th}$ World Conference on Earthquake Engineering*.

Fischinger, M., Isakovic, T. and Kante, P. (2004). Implementation of a macro model to predict seismic response of RC structural walls, *Computers and Concrete* **1**(2): 211–226.

Fischinger, M., Vidic, T. and Fajfar, P. (1992). Nonlinear seismic analysis of structural walls using the multiple-vertical-line-element model, *in* P. Fajfar and H. Krawinkler (eds), *Nonlinear Seismic Analysis and Design of Reinforced Concrete Buildings*, Elsevier Science Publishers Ltd., London and New York.

Frederick, C. O. and Armstrong, P. J. (2007). A mathematical representation of the multiaxial Bauschinger effect, *Materials at High Temperatures* **24**(1): 1–26.

Fu, X.-R., Cen, S., Li, C. F. and Chen, X.-M. (2010). Analytical trial function method for development of new 8-node plane element based on the variational principle containing airy stress function, *Engineering Computations* **27**(4): 442–463.

Ghobarah, A. and Youssef, M. (1999). Modelling of reinforced concrete structural walls, *Engineering Structures* **21**(10): 912–923.

Grassl, P. and Jirásek, M. (2006). Damage-plastic model for concrete failure, *International Journal of Solids and Structures* **43**(22-23): 7166–7196.

Grassl, P., Xenos, D., Nyström, U., Rempling, R. and Gylltoft, K. (2013). CDPM2: A damage-plasticity approach to modelling the failure of concrete, *International Journal of Solids and Structures* **50**(24): 3805–3816.

Gulec, C. K. and Whittaker, A. S. (2009). Performance-based assessment and design of squat reinforced concrete shear walls, *techreport MCEER-09-0010*, MCEER.

Han, X. L., Chen, X. W., Cheang, J., Mao, G. N. and Wu, P. F. (2008). Numerical analysis of cyclic loading test of shear walls based on OpenSees, *Proceedings of the 14$^{th}$ World Conference on Earthquake Engineering*.

Hinton, E. and Owen, D. R. J. (1984). *Finite Elements Software for Plates and Shells*, Pineridge Press, Swansea, UK.

Hrennikoff, A. (1941). Solution of problems in elasticity by the frame work method, *Journal of Applied Mechanics* **8**(4): 169–175.

Hsu, T. T. C. and Zhu, R. R. H. (2002). Softened membrane model for reinforced concrete elements in shear, *ACI Structural Journal* **99**(4): 460–469.

Hu, H. C. (1954). On some variational principles in the theory of elasticity and the theory of plasticity, *Acta Phys. Sin.* **10**(3): 259–290.

Huang, Z. H., Burgess, I. W. and Plank, R. J. (1999). Nonlinear analysis of reinforced concrete slabs subjected to fire, *ACI Structural Journal* **96**(1): 127–135.

Hughes, T. J. R. and Brezzi, F. (1989). On drilling degrees of freedom, *Computer Methods in Applied Mechanics and Engineering* **72**(1): 105–121.

Hughes, T. J. R., Masud, A. and Harari, I. (1995). Numerical assessment of some membrane elements with drilling degrees of freedom, *Computers & Structures* **55**(2): 297–314.

Ibrahimbegović, A. (1993). Mixed finite element with drilling rotations for plane problems in finite elasticity, *Computer Methods in Applied Mechanics and Engineering* **107**(1-2): 225–238.

Ibrahimbegović, A. (1994). Stress resultant geometrically nonlinear shell theory with drilling rotations — part I. A consistent formulation, *Computer Methods in Applied Mechanics and Engineering* **118**(3-4): 265–284.

Ibrahimbegović, A. and Frey, F. (1992). Membrane quadrilateral finite elements with rotational degrees of freedom, *Engineering Fracture Mechanics* **43**(1): 13–24.

Ibrahimbegović, A., Taylor, R. L. and Wilson, E. L. (1990). A robust quadrilateral membrane finite element with drilling degrees of freedom, *International Journal for Numerical Methods in Engineering* **30**(3): 445–457.

Irons, B. M. (1966). Numerical integration applied to finite element methods, *Proceedings of the Conference on Use of Digital Computers in Structural Engineering*, University of Newcastle.

Irons, B. M. (1971). Quadrature rules for brick based finite elements, *International Journal for Numerical Methods in Engineering* **3**(2): 293–294.

Jiang, H. and Lu, X. (2002). Nonlinear earthquake response analysis and energy calculation for seismic slit shear wall structures, *Earthquake Engineering and Engineering Vibration* **1**(2): 227–237.

Jiang, J. J., Lu, X. Z. and Ye, L. P. (2005). *Finite Element Analysis of Concrete Structures (in Chinese)*, Tsinghua University Press.

Jury, R. (2011). Investigation into the collapse of the Pyne Gould Corporation building on 22nd February 2011, *techreport*, Beca Carter Hollings & Ferner Ltd.

Kabeyasawa, T., Shiohara, H., Otani, S. and Aoyama, H. (1983). Analysis of the full-scale seven-story reinforced concrete test structure, *Journal (B), The Faculty of Engineering, University of Tokyo* **XXXVII**(2): 432–478.

Kagermanov, A. and Ceresa, P. (2016). Physically based cyclic tensile model for RC membrane elements, *Journal of Structural Engineering* **142**(12): 04016118.

Kam, W. Y. and Pampanin, S. (2011). The seismic performance of RC buildings in the 22 February 2011 Christchurch earthquake, *Structural Concrete* **12**(4): 223–233.

Kante, P. (2005). *Seismic Vulnerability of Reinforced Concrete Walls (in Slovenian)*, phdthesis, University of Ljubljana.

Kazaz, İ., Yakut, A. and Gülkan, P. (2006). Numerical simulation of dynamic shear wall tests: A benchmark study, *Computers & Structures* **84**(8-9): 549–562.

Kent, D. C. and Park, R. (1971). Flexural members with confined concrete, *Journal of the Structural Division* **97**(7): 1969–1990.

Klinkel, S. and Govindjee, S. (2002). Using finite strain 3D-material models in beam and shell elements, *Engineering Computations* **19**(3): 254–271.

Kolozvari, K. (2013). *Analytical Modeling of Cyclic Shear-flexure Interaction in Reinforced Concrete Structural Walls*, phdthesis, University of California, Los Angeles.

Kolozvari, K., Biscombe, L., Dashti, F., Dhakal, R. P., Gogus, A., Gullu, M. F., Henry, R. S., Massone, L. M., Orakcal, K., Rojas, F., Shegay, A. and Wallace, J. (2019). State-of-the-art in nonlinear finite element modeling of isolated planar reinforced concrete walls, *Engineering Structures* **194**: 46–65.

Kolozvari, K., Orakcal, K. and Wallace, J. W. (2015). Modeling of cyclic shear-flexure interaction in reinforced concrete structural walls. I: Theory, *Journal of Structural Engineering* **141**(5): 04014135.

Kolozvari, K., Tran, T. A., Orakcal, K. and Wallace, J. W. (2015). Modeling of cyclic shear-flexure interaction in reinforced concrete structural walls. II: Experimental validation, *Journal of Structural Engineering* **141**(5): 04014136.

Lee, J. and Fenves, G. L. (1998). Plastic-damage model for cyclic loading of concrete structures, *Journal of Engineering Mechanics* **124**(8): 892–900.

Lee, N.-S. and Bathe, K.-J. (1993). Effects of element distortions on the performance of isoparametric elements, *International Journal for Numerical Methods in Engineering* **36**(20): 3553–3576.

Li, H.-n. and Li, B. (2004). Experimental study on seismic restoring performance of reinforced concrete shear walls, *Proceedings of the 13th World Conference on Earthquake Engineering*, Vancouver, B. C., Canada.

Linde, P. and Bachmann, H. (1994). Dynamic modelling and design of earthquake-resistant walls, *Earthquake Engineering & Structural Dynamics* **23**(12): 1331–1350.

Long, Y.-Q., Cen, S. and Long, Z.-F. (2009). *Advanced Finite Element Method in Structural Engineering*, Springer Berlin Heidelberg.

Long, Y. Q. and Xu, Y. (1994). Generalized conforming quadrilateral membrane element with vertex rigid rotational freedom, *Computers & Structures* **52**(4): 749–755.

Long, Z.-F., Cen, S., Wang, L., Fu, X.-R. and Long, Y.-Q. (2010). The third form of the quadrilateral area coordinate method (QACM-III): Theory, application, and scheme of composite coordinate interpolation, *Finite Elements in Analysis and Design* **46**(10): 805–818.

Lu, X. and Chen, Y. (2005). Modeling of coupled shear walls and its experimental verification, *Journal of Structural Engineering* **131**(1): 75–84.

Lu, X., Xie, L., Guan, H., Huang, Y. and Lu, X. (2015). A shear wall element for nonlinear seismic analysis of super-tall buildings using OpenSees, *Finite Elements in Analysis and Design* **98**: 14–25.

Lu, Y. and Panagiotou, M. (2014). Three-dimensional cyclic beam-truss model for nonplanar reinforced concrete walls, *Journal of Structural Engineering* **140**(3): 04013071.

Lubliner, J., Oliver, J., Oller, S. and Oñate, E. (1989). A plastic-damage model for concrete, *International Journal of Solids and Structures* **25**(3): 299–326.

MacLeod, I. A. (1969). New rectangular finite element for shear wall analysis, *Journal of the Structural Division* **95**(3): 399–409.

MacNeal, R. H. and Harder, R. L. (1985). A proposed standard set of problems to test finite element accuracy, *Finite Elements in Analysis and Design* **1**(1): 3–20.

MacNeal, R. H. and Harder, R. L. (1988). A refined four-noded membrane element with rotational degrees of freedom, *Computers & Structures* **28**(1): 75–84.

Madeo, A., Casciaro, R., Zagari, G., Zinno, R. and Zucco, G. (2014). A mixed isostatic 16 DOF quadrilateral membrane element with drilling rotations, based on airy stresses, *Finite Elements in Analysis and Design* **89**: 52–66.

Madeo, A., Zagari, G. and Casciaro, R. (2012). An isostatic quadrilateral membrane finite element with drilling rotations and no spurious modes, *Finite Elements in Analysis and Design* **50**: 21–32.

Martinelli, P. and Filippou, F. C. (2009). Simulation of the shaking table test of a seven-story shear wall building, *Earthquake Engineering & Structural Dynamics* **38**(5): 587–607.

Massone, L. M. (2006). *RC Wall Shear-flexure Interaction: Analytical and Experimental Responses*, phdthesis, University of California, Los Angeles.

Massone, L. M. (2010). Strength prediction of squat structural walls via calibration of a shear-flexure interaction model, *Engineering Structures* **32**(4): 922–932.

Menegotto, M. and Pinto, P. E. (1973). Method of analysis for cyclically loaded R.C. plane frames including changes in geometry and non-elastic behaviour of elements under combined normal force and bending.

Miao, Z. W., Lu, X. Z., Jiang, J. J. and Ye, L. P. (2006). Nonlinear FE model for RC shear walls based on multi-layer shell element and micro-plane constitutive model, *Computational Methods in Engineering & Science*, Springer Berlin Heidelberg, pp. 204–204.

Milev, J. I. (1996). Two dimensional analytical model of reinforced concrete shear walls, *Proceedings of the 11$^{th}$ World Conference on Earthquake Engineering*.

Mo, Y. L., Zhong, J. and Hsu, T. T. C. (2008). Seismic simulation of RC wall-type structures, *Engineering Structures* **30**(11): 3167–3175.

Nakamura, N., Tsunashima, N., Nakano, T. and Tachibana, E. (2009). Analytical study on energy consumption and damage to cylindrical and i-shaped reinforced concrete shear walls subjected to cyclic loading, *Engineering Structures* **31**(4): 999–1009.

Neuenhofer, A. and Filippou, F. C. (1997). Evaluation of nonlinear frame finite-element models, *Journal of Structural Engineering* **123**(7): 958–966.

Nodargi, N. A. and Bisegna, P. (2017). A novel high-performance mixed membrane finite element for the analysis of inelastic structures, *Computers & Structures* **182**: 337–353.

Nooru-Mohamed, M. B. (1992). *Mixed-mode Fracture of Concrete: An Experimental Approach*, phdthesis, Delft University of Technology.

Oesterle, R. G., Fiorato, A. E., Aristizabal-Ochoa, J. D. and Corley, W. G. (1980). Hysteretic response of reinforced concrete structural walls, *ACI Special Publication* **63**: 243–274.

Orakcal, K. and Wallace, J. W. (2006). Flexural modeling of reinforced concrete walls — experimental verification, *ACI Structural Journal* **103**(2): 196–206.

Orakcal, K., Wallace, J. W. and Conte, J. P. (2004). Flexural modeling of reinforced concrete walls — model attributes, *ACI Structural Journal* **101**(5): 688–698.

Otani, S. and Sozen, M. A. (1972). Behavior of multistory reinforced concrete frames during earthquakes, *techreport UILU-ENG-72-2018*, University of Illinois.

Palermo, D. and Vecchio, F. J. (2002). Behavior of three-dimensional reinforced concrete shear walls, *ACI Structural Journal* **99**(1).

Palermo, D. and Vecchio, F. J. (2004). Compression field modeling of reinforced concrete subjected to revered loading: Verification, *ACI Structural Journal* **101**(2).

Palermo, D. and Vecchio, F. J. (2007). Simulation of cyclically loaded concrete structures based on the finite-element method, *Journal of Structural Engineering* **133**(5): 728–738.

Parulekar, Y. M., Reddy, G. R., Vaze, K. K., Pegon, P. and Wenzel, H. (2014). Simulation of reinforced concrete short shear wall subjected to cyclic loading, *Nuclear Engineering and Design* **270**: 344–350.

Pian, T. H. H. and Sumihara, K. (1984). Rational approach for assumed stress finite elements, *International Journal for Numerical Methods in Engineering* **20**(9): 1685–1695.

Piltner, R. and Taylor, R. L. (1995). A quadrilateral mixed finite element with two enhanced strain modes, *International Journal for Numerical Methods in Engineering* **38**(11): 1783–1808.

Piltner, R. and Taylor, R. L. (1999). A systematic construction of B-bar functions for linear and non-linear mixed-enhanced finite elements for plane elasticity problems, *International Journal for Numerical Methods in Engineering* **44**(5): 615–639.

Pimpinelli, G. (2004). An assumed strain quadrilateral element with drilling degrees of freedom, *Finite Elements in Analysis and Design* **41**(3): 267–283.

Pivonka, P., Ožbolt, J., Lackner, R. and Mang, H. A. (2004). Comparative studies of 3D-constitutive models for concrete: Application to mixed-mode fracture, *International Journal for Numerical Methods in Engineering* **60**(2): 549–570.

Polak, M. A. and Vecchio, F. J. (1993). Nonlinear analysis of reinforced-concrete shells, *Journal of Structural Engineering* **119**(12): 3439–3462.

Popovics, S. (1973). A numerical approach to the complete stress-strain curve of concrete, *Cement and Concrete Research* **3**(5): 583–599.

Ramberg, W. and Osgood, W. R. (1943). Description of stress-strain curves by three parameters.

Rejec, K., Isaković, T. and Fischinger, M. (2011). Seismic shear force magnification in RC cantilever structural walls, designed according to eurocode 8, *Bulletin of Earthquake Engineering* **10**(2): 567–586.

Royal Commission (2011a). Volume 2: The performance of Christchurch CBD buildings, *techreport*, Royal Commission.
**URL:** *https://canterbury.royalcommission.govt.nz/Final-Report-Volume-Two-Contents*

Royal Commission (2011b). Volume 6: Canterbury television building (CTV), *techreport*, Royal Commission.
**URL:** *https://canterbury.royalcommission.govt.nz/Final-Report-Volume-Six-Contents*

Salonikios, T. N., Kappos, A. J., Tegos, I. A. and Penelis, G. G. (1999). Cyclic load behavior of low-slenderness reinforced concrete walls: Design basis and test results, *ACI Structural Journal* **96**(4): 649–660.

Scordelis, A. C. (1967). Analysis of continuous box girder bridges, *resreport*, University of California, Berkeley.

Shang, Y. and Ouyang, W. (2017). 4-node unsymmetric quadrilateral membrane element with drilling DOFs insensitive to severe mesh-distortion, *International Journal for Numerical Methods in Engineering* **113**(10): 1589–1606.

Shanno, D. F. (1970). Conditioning of quasi-Newton methods for function minimization, *Mathematics of Computation* **24**(111): 647–647.

Simo, J. C. and Hughes, T. J. R. (1998). *Computational Inelasticity*, Springer New York.

Simo, J. C. and Rifai, M. S. (1990). A class of mixed assumed strain methods and the method of incompatible modes, *International Journal for Numerical Methods in Engineering* **29**(8): 1595–1638.

Spacone, E., Ciampi, V. and Filippou, F. C. (1996). Mixed formulation of nonlinear beam finite element, *Computers & Structures* **58**(1): 71–83.

Sze, K. Y., Chan, W. K. and Pian, T. H. H. (2002). An eight-node hybrid-stress solid-shell element for geometric non-linear analysis of elastic shells, *International Journal for Numerical Methods in Engineering* **55**(7): 853–878.

Sze, K. Y., Chen, W. J. and Cheung, Y. K. (1992). An efficient quadrilateral plane element with drilling degrees of freedom using orthogonal stress modes, *Computers & Structures* **42**(5): 695–705.

Taig, I. G. and Kerr, R. I. (1964). Some problems in the discrete element representation of aircraft strcutures, *in* F. de Veubeke (ed.), *Matrix Methods of Structural Analysis*, The Pitman Press, Bath, pp. 267–316.

Takeda, T., Sozen, M. A. and Nielsen, N. N. (1970). Reinforced concrete response to simulated earthquakes, *Journal of the Structural Division* **96**(12): 2557–2573.

Tang, L. M., Chen, W. J. and Liu, Y. X. (1984). Formulation of quasi-conforming element and hu-washizu principle, *Computers & Structures* **19**(1-2): 247–250.

Taylor, R. G. (1977). *The Nonlinear Seismic Response of Tall Shear Wall Structures*, phdthesis, University of Canterbury.

Taylor, R. L., Beresford, P. J. and Wilson, E. L. (1976). A non-conforming element for stress analysis, *International Journal for Numerical Methods in Engineering* **10**(6): 1211–1219.

Thomsen, J. H. and Wallace, J. W. (2004). Displacement-based design of slender reinforced concrete structural walls — experimental verification, *Journal of Structural Engineering* **130**(4): 618–630.

Thomson, E. D., Perdomo, M. E., Picón, R., Marante, M. E. and Flórez-López, J. (2009). Simplified model for damage in squat RC shear walls, *Engineering Structures* **31**(10): 2215–2223.

Timoshenko, S. (1970). *Theory of Elasticity*, McGraw-Hill College.

Tran, T. A. and Wallace, J. W. (2015). Cyclic testing of moderate-aspect-ratio reinforced concrete structural walls, *ACI Structural Journal* **112**(6): 653–665.

Tsai, W. T. (1988). Uniaxial compressional stress-strain relation of concrete, *Journal of Structural Engineering* **114**(9): 2133–2136.

Turner, M. J., Clough, R. W., Martin, H. C. and Topp, L. J. (1956). Stiffness and deflection analysis of complex structures, *Journal of the Aeronautical Sciences* **23**(9): 805–823.

Valoroso, N., Marmo, F. and Sessa, S. (2014). Limit state analysis of reinforced shear walls, *Engineering Structures* **61**: 127–139.

Vecchio, F. J. (2000). Disturbed stress field model for reinforced concrete: Formulation, *Journal of Structural Engineering* **126**(9): 1070–1077.

Vecchio, F. J. and Chan, C. C. L. (1990). Reinforced concrete membrane elements with perforations, *Journal of Structural Engineering* **116**(9): 2344–2360.

Vecchio, F. J. and Collins, M. P. (1986). The modified compression-field theory for reinforced concrete elements subjected to shear, *ACI Journal Proceedings* **83**(2): 219–231.

Vulcano, A. (1992). Use of wall macroscopic models in the nonlinear analysis of RC frame-wall structures, *Earthquake Engineering, Tenth World Conference*.

Vulcano, A., Bertero, V. V. and Colotti, V. (1988). Analytical modeling of R/C structural walls, *Proceedings of Ninth World Conference on Earthquake Engineering*.

Wallace, J. W. (2012). Behavior, design, and modeling of structural walls and coupling beams — lessons from recent laboratory tests and earthquakes, *International Journal of Concrete Structures and Materials* **6**(1): 3–18.

Wang, C., Zhang, X. and Hu, P. (2016). New formulation of quasi-conforming method: A simple membrane element for analysis of planar problems, *European Journal of Mechanics - A/Solids* **60**: 122–133.

Wang, H.-B. and Shen, P.-S. (2005). Nonlinear seismic response analysis of reinforced concrete tube in tube structure, *Journal of Central South University of Technology* **12**(1): 183–188.

Willam, K. J. (1969). *Finite Element Analysis of Cellular Structures*, phdthesis, University of California, Berkeley.

Williams, S. A. (2014). *Numerical analysis of reinforced masonry shear walls using the nonlinear truss approach*, mathesis, Virginia Polytechnic Institute and State University.

Wriggers, P. (2008). *Nonlinear Finite Element Methods*, Springer Berlin Heidelberg.

Wriggers, P. and Reese, S. (1996). A note on enhanced strain methods for large deformations, *Computer Methods in Applied Mechanics and Engineering* **135**(3-4): 201–209.

Wu, C.-C., Huang, M.-G. and Pian, T. H. (1987). Consistency condition and convergence criteria of incompatible elements: General formulation of incompatible functions and its application, *Computers & Structures* **27**(5): 639–644.

Wu, Y.-T., Lan, T.-Q., Xiao, Y. and Yang, Y.-B. (2016). Macro-modeling of reinforced concrete structural walls: State-of-the-art, *Journal of Earthquake Engineering* **21**(4): 652–678.

Yang, J., Wallace, J. W. and Lu, X. (2013). Nonlinear analysis of reinforced concrete walls using new concrete model in OpenSees, *2013 Fifth International Conference on Measuring Technology and Mechatronics Automation*, IEEE.

Young, W. C. (2012). *Roark's Formulas for Stress and Strain*, 8th edn, McGraw-Hill Education.

Zhang, Y. X. and Bradford, M. A. (2007). Nonlinear analysis of moderately thick reinforced concrete slabs at elevated temperatures using a rectangular layered plate element with timoshenko beam functions, *Engineering Structures* **29**(10): 2751–2761.

Zienkiewicz, O. C., Taylor, R. L. and Zhu, J. Z. (2013). *The Finite Element Method: Its Basis and Fundamentals*, 7 edn, Butterworth-Heinemann.

Zienkiewicz, O. and Taylor, R. (1997). The finite element patch test revisited a computer test for convergence, validation and error estimates, *Computer Methods in Applied Mechanics and Engineering* **149**(1-4): 223–254.

Zouari, W., Hammadi, F. and Ayad, R. (2016). Quadrilateral membrane finite elements with rotational DOFs for the analysis of geometrically linear and nonlinear plane problems, *Computers & Structures* **173**: 139–149.

ZHANG lei